Space Densities and Unified Models of AGN

by

Melanie A. Gendre

B.Sc., The University of Victoria, 2004

A THESIS SUBMITTED IN PARTIAL FULFILMENT OF
THE REQUIREMENTS FOR THE DEGREE OF

Master of Science

in

The Faculty of Graduate Studies

(Astronomy)

The University Of British Columbia

September, 2006

Abstract

Using combined information from both FIRST and NVSS radio surveys at 1.4GHz, a sample of 282 sources with $S_{lim} = 1.3Jy$ was constructed. Radio morphological type were determined for each sources, and redshift information was found for 94% of the sample members, from databases such as SIMBAD and SDSS. A source count at 1.4 GHz was constructed from results in the literature. Space-density models using the Wall, Pearson & Longair (1980) technique were then applied using the sample and the source count; parameters for these models were optimized for the entire sample, as well as for the sample of extended sources only. In both cases, it was found that an exponential evolution with $P_t = alog(z) + b$ gave the best fit. In the case of the entire sample, the V/V_{max} statistics was computed, where $< V/V_{max} >= 0.6113$ with $\sigma = 0.0174$.

This project was mainly a pilot study to determine if the modeling of the luminosity function and epoch dependence of radio AGN was possible, primarily using the FIRST and NVSS samples in a complementary manner. This is a further way in which these huge radio surveys may be exploited for cosmological purposes and physical understanding of AGN. Since this study was successful, future work will involve using samples from FIRST and NVSS at different flux limits and applying this and much more sophisticated modeling techniques to determine the evolutions of the FRI and FRII populations separately. Ultimately, the goal of such a project would be to compare these evolutions and to use them as bases to derive new versions of the dual-population unified model described by Wall & Jackson (1997). This unified model has been successful until now but these new data should provide a comprehensive test – which may reject the formulation; or may suggest modifications that further our physical insight into the hosting/beaming paradigm of powerful radio AGN.

Table of Contents

List of Tables

List of Figures

Acknowledgements

I would like to thank my supervisor, Jasper Wall, for his help and patience throughout these two years, as well as Chris Blake for always having been here to answer my questions.
I would also like to thank Lara and Mya for their support and for accompanying me to my numerous and very much needed coffee breaks.
Finally, I would like to thank Matt for fixing my computer and helping me through my "I-broke-fortran-again" problems so many times.

Chapter 1

Introduction

[1]All galaxies are sources of radio emission. Among them, the sources of higher radio luminosity are Seyfert galaxies, starburst galaxies and Active Galactic Nuclei (AGN) galaxies. Because radio observations are not affected by intergalactic medium, radio surveys offer a large number of galaxies over a wide range of redshifts (the median redshift of galaxies detected in radio surveys is typically z=1 (Condon, 1989)), giving statistically complete samples with high accuracy position measurements. However, radio surveys ultimately rely on optical surveys to get the redshift and morphology of the host objects. It also frequently happens that no obvious optical counterpart is found, especially for sources with extended structure not showing an obvious core.

More than 95% of sources at flux densities above 50mJy at 1.4GHz (the frequency of the sample used in this thesis) are classified as AGN and radio galaxies. Below 50mJy, the number of AGN declines and the proportion of starburst galaxies increases (Condon, 1989; Sadler et al., 2002).

AGN are interesting to investigate extreme physics (collimation, black hole physics, plasma ejection, confinement, etc...). They are also one of the most important probe in the study of the formation and evolution of our Universe. The later is precisely the subject of this thesis: determining the evolution of radio sources.

In this introduction, the classification of radio galaxies will be described (§1.1), as well as the evolutionary scenario for radio galaxies and the unified schemes associated with them (§1.2). Some key terms will then be defined (§1.3) before discussing the radio surveys used (§1.4) and giving an overview of the content of this thesis (§1.5).

1.1 Classification of Radio Objects

The first analysis of radio sources classified AGNs into two populations based on their spectral type: "steep-spectrum" and "flat-spectrum". "Steep-spectrum" type follows a power law, presumably corresponding to the electron distribution in the optically thin environment. "Flat-spectrum" type corresponds to all sources not falling into the "steep-spectrum" category. Their spectra show curvature and bumps, due to synchrotron self-absorption in the optically thick environment.

[1]Throughout this thesis, the following appellations will be used: P for luminosity and S for flux.

A number of papers, including Wall, Pearson & Longair (1980) and Dunlop & Peacock (1990), dealt with the evolution of "flat" and "steep"-spectra separately. In particular, Dunlop & Peacock (1990) found that both types could be fitted independently by pure luminosity evolution (PLE) and free-form evolution models (where no preconceived assumptions is made as to the form of the evolution - see Peacock (1985)) and, most importantly, that both populations were undergoing very similar differential evolutions. Since then, the classification of AGN has changed.

In general, AGN can be considered as being either radio loud or radio quiet objects.

1.1.1 Radio Loud Objects

Radio loud objects are powerful sources with $P_{178MHz} \geq 10^{22}\ WHz^{-1}\ sr^{-1}$, whose radio structure extends from pc to Mpc scales. The sources consist of a central black hole emitting collimated opposing jets of plasma, whose nature is unknown. The jets feed energy and highly relativistic particles into radio lobes (Rees, 1971) and are terminated by shock with the intergalactic medium, creating radio hot spots (Scheuer, 1974; Blandford & Rees, 1974). In many cases, the ejected plasma blobs close to the nucleus show superluminal motion (their apparent motion exceeds the speed of light), probably as a result of relativistic bulk motion close to the line of sight of the observer (Rees, 1967).
There are no sharp features in the radio spectrum of radio loud galaxies and QSOs. Their spectra is described by the spectral index $\alpha = d(lnS)/d(ln\nu)$, where $-1.4 < \alpha < -0.5$ for extended radio sources and $-0.5 < \alpha < 0.5$ for compact sources.

The classification of radio loud object is based on radio morphology and optical/UV characteristics.
The Fanaroff-Riley (FR) scheme (Fanaroff & Riley, 1974) is based on the ratio R of the distance between the central maxima of the source and the overall size of the object (see Figure 1.1 for examples of FRI and FRII sources).

FRI These sources have a ratio $R < 0.5$ and are of moderate radio luminosity with $P_{178MHz} \leq 3 \times 10^{25} WHz^{-1}sr^{-1}$. They are lobe-dominated sources, with the lobes connected by smooth and continuous double-sided jets. The FRI class includes many disturbed and atypical radio structures (Parma et al., 1992). In the optical/UV, their spectrum is dominated by stellar emission, with only weak (or zero) narrow-line emission from the AGN.

FRII These sources have a ratio $R > 0.5$ and are of higher radio luminosity with $P_{178MHz} \geq 3 \times 10^{25} WHz^{-1}sr^{-1}$. They are also lobe-dominated, with more collimated (smaller opening angle) and less smooth jets than FRIs. Contrary to FRIs, the steepest-spectrum part of the source is found in its innermost region. In the optical/UV, the spectrum of FRII sources generally shows only narrow or no emission lines of high excitation level.

QSO These sources are generally core-dominated. However, the differences are drastic: the outer lobes and hot spots are still visible although the central core and jets are very much more prominent. Their structure almost always appear one-sided in the milliarcsecond scale. In the optical/UV, QSOs show broad and narrow emission lines together with a bright blue continuum.

BL Lac These sources are compact and have very strong and varying continuum emission at all wavelength. In the optical/UV, they show weak or no emission lines and no evidence of stellar spectrum.

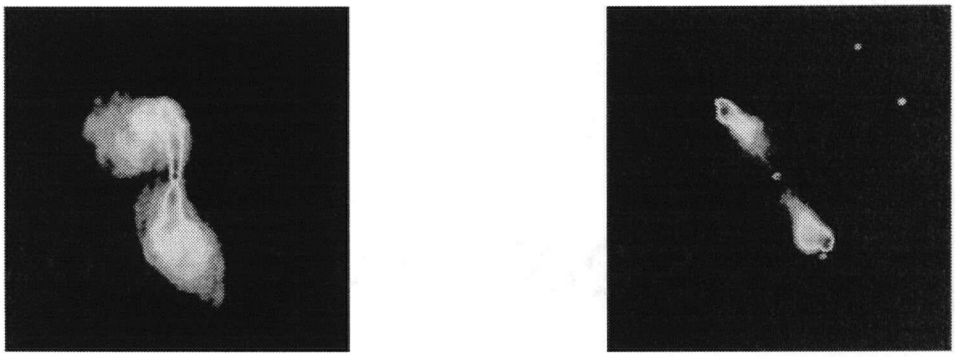

Figure 1.1: Radio images from the 3CRR catalog (Laing, Riley & Longair, 1983). 3C272.1 (left) is a FRI type source, with diffuse, approximately symmetric jets whose surface brightness falls off away from the center. 3C457 (right) is a FRII type source, with sharp-edged lobes and bright hot spots.(www.jb.man.ac.ukatlas)

1.1.2 Radio Quiet Objects

Objects found in radio surveys are classified as radio quiet if $P_{178MHz} \leq 10^{22}$ WHz^{-1} sr^{-1}. Those are almost exclusively late type host galaxies which dominate radio surveys at low flux densities. Saunders et al. (1990) studied their evolution. Because there is no evidence for any Doppler beaming, they are outside of the unified scheme (see §1.1.2).

Starburst galaxies These sources show diffuse radio emission from synchrotron radiation from supernovae remnants, bremsstrahlung and free-free emission from HII regions.

Seyfert galaxies These sources have broad and narrow emission lines associated with radio quiet AGN (Seyfert, 1943). They are probably a miniature version of QSOs.

[2]BL≡Broad Line, NL≡Narrow Line

Table 1.1: Extragalactic radio source populations (Jackson & Wall, 1999)

Population	Optical emission type	Radio spectrum $\nu \sim 5$ GHz	Doppler beamed version
FRII high excitation radio galaxies	BL^2	flat	QSO
	BL	steep	-
	NL^2	steep	-
FRII low excitation radio galaxies	none	flat	BL-Lac
	weak NL/ none	steep	-
FRI radio galaxies	none	flat	BL-Lac
	weak NL/ none	steep	-
Starbursts and Seyferts	BL	steep	-
	NL	steep	-

Elliptical galaxies When the cores of elliptical galaxies are imaged at high resolution, their nuclei often either show structures associated with FRI or simply a weak compact core. About 40% of NGC galaxies show non-thermal activity.

1.2 Evolutionary scenarios and unified schemes

It is believed that radio sources undergo some kind of cosmic evolution[3]. All scenarios are a combination of two possible evolutions: luminosity evolution (where the luminosity changes with epoch) and density evolution (where the density changes with epoch).
The two most popular forms of evolution model are the power law evolution and the exponential evolution.

Power law evolution The main assumption of the power law evolution model is that whatever has caused the evolution goes as some power of (1+z), and is therefore cosmic time dependent. This also suggests some direct relation between the scale size of the Universe (dependent on the epoch) and the space density of sources, scaling as $(1+z)^{\kappa}$. This form of evolution is fairly simple; however, it has to be terminated at some redshift cutoff to prevent the resultant source count from diverging.

Exponential law evolution This form was first investigated by Doroshkevich et al. (1970). Here, the evolution scales as $exp(M\tau)$, where M is a measure of the

e-folding rate and τ is the look-back time as a fraction of the Hubble time.

As stated in the previous section, investigation of the luminosity function of "flat-" and "steep-"spectrum sources by Dunlop & Peacock (1990) showed that both types were undergoing the same evolution. Evidence accumulated that observed populations of radio loud AGN were strongly orientation dependent, giving rise to the concept of "unified schemes". These schemes assumed a parent radio source population, where the random orientation of the population to our line of sight was the cause of the different source types observed (Orr & Browne, 1982). A dual population model based on the sources radio power (FRI and FRII types) was then introduced (Jackson & Wall, 1999) . In this model, both population exhibit anisotropic radiations arising from Doppler beaming (superluminal motion of the radio jets), and obscuration by a dusty torus contributes to the orientation dependent appearance of the high power FRII (see figure 1.2).

[3]The term *evolution* used here implies either a change in the total number of sources (they are created or disappear) or a change in the luminosity of the sources (they become brighter or fainter).

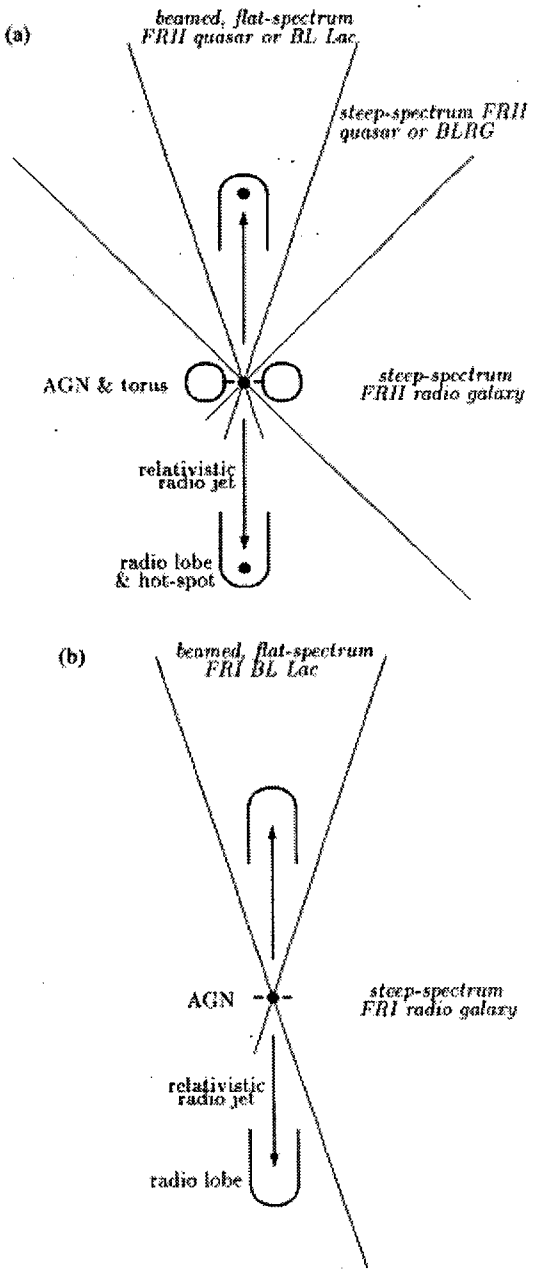

Figure 1.2: Jackson & Wall (1999): Unified Scheme models (a) FRII radio sources; (b) FRI radio sources.

1.3 Definitions

1.3.1 Source Count

The source count is the surface density as a function of flux density at a given frequency. Because the cumulative source count N($> S$) implies that points are not independent of each other, the differential form of the source count, $\Delta N/\Delta N_0$ (where $N_0 = \kappa_\nu S^{-1.5}$) is usually used.

In the case of an Euclidean universe[4]and constant space density, the integral count is observed to accord with $N \propto S^{-1.5}$ (Wall, 1983). However, the source count does not follow this simple Euclidean geometry (Ryle & Clark, 1961). Since there is no steady state, the radio population must therefore be evolving as a function of redshift. Longair (1966) showed that this evolution was differential: the lower-luminosity sources show little or no evolution whereas the most luminous sources undergo the most dramatic evolution. Radio source counts can therefore potentially yield important information on the cosmological evolution of both active and star-burst galaxies (Longair, 1966; Wall, Pearson & Longair, 1980).

The first direct test of evolution, the V/V_{max} test, was created by Schmidt in 1968 (Schmidt, 1968). For this test, the volume V between redshift 0 and redshift z of each source is compared to the volume V_{max} between redshift 0 and the redshift where the source is pushed to the flux limit of the survey (note that in the case where both optical and radio surveys are involved, this flux limit corresponds to the first limit encountered). If the survey deals with non-evolving sources, V/V_{max} values would be uniformly distributed between 0 and 1, implying $\langle V/V_{max}\rangle = 0.5$[5](with $\sigma = 1/\sqrt{12N}$). If $\langle V/V_{max}\rangle \geq 0.5$, there are therefore more radio sources at greater distance. Using a sample of 33 QSOs from the 3C catalog, Schmidt found a value of $\langle V/V_{max}\rangle = 0.7$ ($\sigma = 0.05$), implying an increasing number of sources with epoch, which is consistent with a strong cosmological evolution.

Figure 1.3 (Jackson & Wall, 1999) shows differential source counts at different frequencies. The source counts can be split into four main regions[6]:

1. At high flux densities ($logS > 0.5$), the differential source count is near Euclidean, due to the mixture of nearby sources and distant bright objects (the evolving sources at high redshift are diluted by the more abundant local sources).

[4]An Euclidean universe is a flat, infinite universe.

[5]Proof:
The observed number of objects in the (P,z) plane is:

$$N = \int_0^\infty \rho(P)dP \int_0^{z_{max}} \frac{dV}{dz} dz$$

therefore:

$$\langle V/V_{max}\rangle = \frac{\int_0^\infty \rho(P)dP \int_0^{V_{max}} \frac{V}{V_{max}} dV}{\int_0^\infty \rho(P)dP \int_0^{V_{max}} dV} = \frac{1}{2}$$

This result is independent of the luminosity function $\rho(P)$.

2. Between $logS = -1$ and $logS = 0.5$, the differential count is dominated by powerful sources at high redshift, showing how extreme their evolution is. The bulge there hints at a sharp peak in density at some epoch, and the width of the plateau varies with frequency due to the increasing contribution of flat-spectrum sources (Kellerman & Wall, 1987), which are predominantly QSOs.

3. In the next three orders of magnitude ($-4 < logS < -1$), the count is made up of lower power sources at intermediate redshift and drops away from the Euclidean prediction.

4. At low flux densities ($logS < -4$), the source count flatten back to near Euclidean and is made up mostly of "blue" starburst and "red" FRI type galaxies, which are seen at relatively small redshift ($z < 0.4$).

[6] An interpretation of the different slopes of the relative differential source count can be found in Wall (1983).

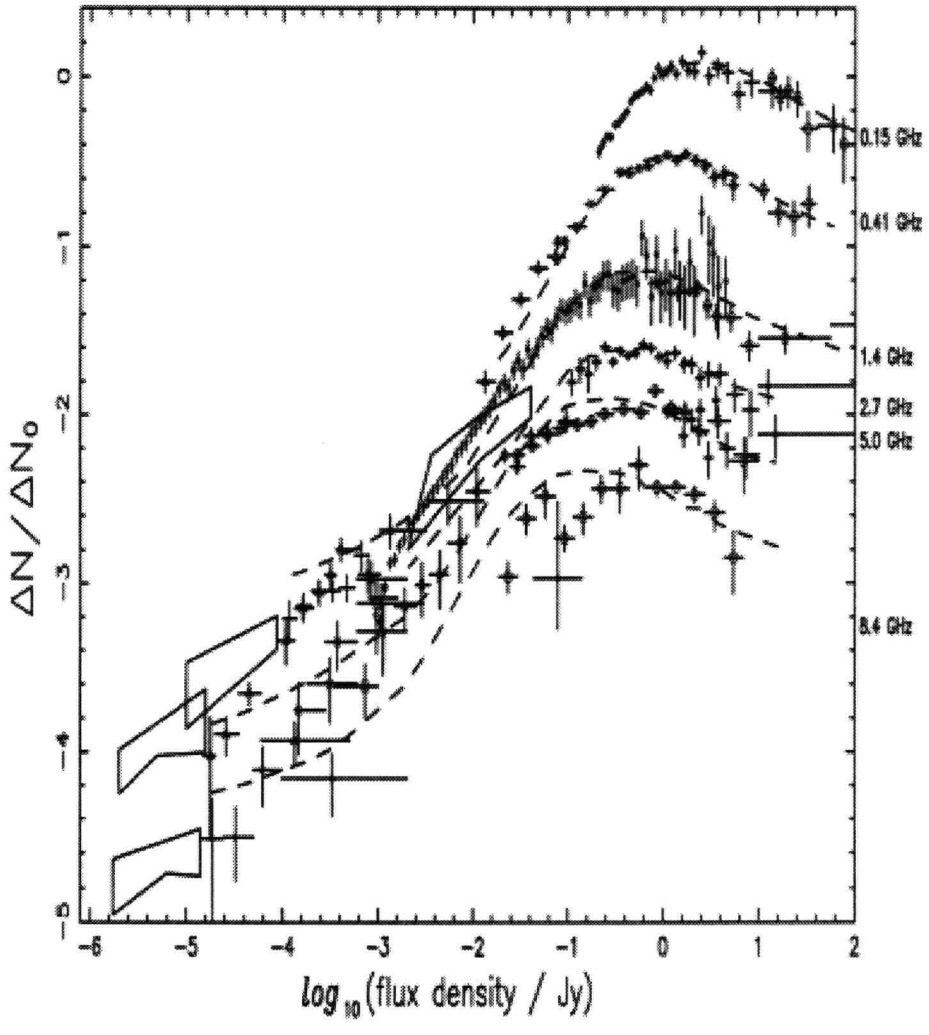

Figure 1.3: Jackson & Wall (1999): Source counts at various frequencies in relative differential form where ΔN_0 is the number of sources expected in a uniformly-filled Euclidean universe ($N_0 = K_\nu S_\nu^{-3/2}$). The dash curves are polynomial least square fits to the counts.

1.3.2 Miscellaneous

Radio Luminosity Function $\rho(P, z)$. Space density of radio sources at a given luminosity, per unit luminosity and at a particular epoch. At the current epoch (z=0), the luminosity function is called the local luminosity function. It is usually expressed as the number of sources per unit volume (Mpc^3) per unit Δz per unit $\Delta log P_\nu$.

Evolution function F(P,z). Determines the evolution of the radio sources as a function of luminosity and redshift. In the models of radio luminosity function used in this thesis, the evolution function is used to modify the local luminosity function (LLF) to give the radio luminosity function (RLF) at a given epoch z $[\rho(P, z) = F(P, z) \times \rho_0(P)]$.

Redshift cutoff z_c. Maximum redshift at which a population exists (at larger redshift, its space density is zero).

Luminosity distribution N(P). Distribution of intrinsic radio luminosities in a complete flux limited sample. Note that in the case of no evolution (i.e. F(P,z)=1), each source in this distribution would contribute exactly $1/V_{max}$ to the RLF (direct relation). For evolving sources, the contribution would be $1/(F(P, z) \times V_{max})$.

1.4 Surveys

Two main radio surveys used in this work: FIRST and NVSS; two optical surveys were also used: SDSS and 2dF.[7]

FIRST The Faint Images of the Radio Sky at Twenty centimeters survey (White et al., 1997) is a VLA survey at 1.4GHz containing over 800,000 sources with S_{lim}=1 mJy and covering 9030 deg^2 of the northern sky with a beam size of 5".
The small angular beam size makes the FIRST survey highly reliable since it makes it easier to cross-correlate radio sources with their optical host galaxies (since more details are visible than with a larger beam size). It also means that the observations are not sensitive to extended radio structures and therefore the total radio luminosity of sources larger than a few arcsec is underestimated (Becker et al., 1995). In addition, many extended sources are split into multiple components in FIRST.

NVSS The NRAO-VLA Sky Survey (Condon et al., 1998) at 1.4GHz covers the entire sky north of -40 degrees declination, contains about 1.8 million sources with S_{lim}=2.3 mJy and has a beam size of 45".
Contrary to the FIRST survey, most radio sources (93%) are contained within a single NVSS component due to the relatively large beam size. This made NVSS the first radio survey to permit automated cross-correlation with optical surveys. However, high angular beam size also implies low resolution, leading to significant uncertainties in cross-identifying the radio sources with their optical host galaxies.

There is therefore a trade-off between the reliability of the optical identification and the completeness of the sample.

SDSS The Sloan Digital Sky Survey (York et al., 2000) is an optical imaging (u, g, r, i, z bands) and spectroscopic survey of about a quarter of the extragalactic sky (covering the same region as the FIRST survey) carried out at the Apache Point Observatory.

2dF The 2-degrees Field survey (Colless, 1999; Colless et al., 2001) is an Anglo-Australian Telescope spectroscopic survey covering 2000deg^2 in southern hemisphere. The subsection of the 2dF survey used in this thesis is the 2dFGRS (2dF Galaxy Redshift Survey (Sadler et al., 2002)), which contains about 256,000 sources with limit of $b_j = 19.45$.

Both FIRST and NVSS surveys are used in this thesis to select objects in the studied samples, as they are highly complementary surveys (Best et al. (2005) describes in detail the advantages of combining both surveys). Indeed, if FIRST is the only primary catalog used, the fact that different components of the same source may be resolved as different objects for extended objects creates a bias in the sample. NVSS is therefore used to maximize the completeness and reliability of the resulting sample, making sure that no extended sources are left out.

The 2dF and SDSS catalogs are mostly used as support data for redshift determination, essential in modeling the luminosity function and its epoch dependence.

1.5 Overview of this thesis

The project has two main goals:

- Determine the physical evolution parameters for the different populations (FRI and FRII) of extended radio AGN.
- Due to the always increasing amount of available data permitting us to study both population separately, we can aim to answer the following questions: Is the dual-population unified scheme based on FRI and FRII objects as two separate host populations still acceptable? Or, where does it fail, and how do we modify it in a physically meaningful way to describe the data? Can a simpler single-population model (Snellen & Best, 2001) describe the evolution?

This master's project is mainly a pilot study to determine if the goals described above can be met by samples defined by two existing radio surveys (namely, FIRST and NVSS). It lays the groundwork for a detailed study of the dual-population unified model (Jackson & Wall, 1999).

[7]The surveys can be found at: FIRST: http:sundog.stsci.edu NVSS: http:www.cv.nrao.edunvss SDSS: http:cas.sdss.org 2dF: http:www.aao.gov.au2df

This project was done in three main steps

1. Creating the primary sample of radio sources, complete to a given integrated flux density at 1.4GHz. This step included selecting the sources by combining information from FIRST and NVSS, finding redshift information and determining the morphological type (FRI, FRII, unresolved, etc.) for each sources (§2.1). The luminosity distributions (for the entire sample as well as for extended sources only) were then computed (§2.2.1).

2. Compiling a source count at 1.4GHz over a wide range of flux densities for both the entire sample and the sub-sample of extended sources only (§2.2.2).

3. Modeling the radio luminosity function using the Wall, Pearson & Longair (1980) technique (§3.1) for both the entire sample and the sample of extended sources only (§3.2 and §3.3).

In this modeling, maximum likelihood and a downhill-simplex method were used to determine optimum model parameters.

Chapter 2

Data: The 1.4GHz Primary Sample and Source Count

In order to study the luminosity function of AGNs and its evolution, two types of data are needed: at least one luminosity distribution of a sample of sources chosen at a given limiting flux density and at least one source count compiled at the same frequency as the luminosity distribution.

In this chapter, both data types used in this thesis will be described. First will be described the source selection criteria for the primary sample (§2.1.1) as well as the processes used to estimate redshifts and sort the sources into the different radio types (§2.1.2). The computation of the luminosity distribution used for the models will then be discussed (§2.2.1). Finally, the different source counts compiled will be presented (§2.2.2).

2.1 Construction of the primary sample

The sample was constructed in several steps:

1. All sources from the FIRST catalog with S_{int}[8] $\geq$ 1.3Jy were selected. The value of the flux limit was chosen to produce a sample from the FIRST catalogue with a number of object not exceeding 200. Each source was then compared with its NVSS counterpart to ensure that it was an actual source and not one of the components of an extended source resolved in FIRST due to the small beam size. A total of 184 objects were selected during this first process.

2. As previously stated, some sources in the FIRST catalog are actually resolved components of more extended sources. These components might have an individual flux density lower than the 1.3Jy flux limit, but the actual source might have a flux density above 1.3Jy, when all its components are added. In order to account for these sources, sources from the FIRST survey with 0.5Jy<S<1.3Jy were compared with their NVSS counterpart. If the flux density of the counterpart was above the flux limit, a visual cross-check was done using contour plots of FIRST and NVSS radio flux density (to ensure the FIRST source is actually a component of the NVSS source and not a close-by but independent source). After cross-check, 92 sources[9]were added to the sample, raising the total number of sources to 276.

[8]Flux integrated over the entire area of the source.

3. Finally, it was also necessary to account for the giant sources which might even be resolved in NVSS. Fortunately, these sources are well known: 9 of the 3CR sources located in the FIRST region not included in the sample were added, giving a final number of 285 sources for the primary sample.

Those three steps ensured that no source above the flux limit in the FIRST region was left out, creating an unbiased sample of sources at $S_{1.4GHz} \geq 1.3$Jy.

2.1.1 Redshift estimate

For most of these bright sources, redshift information were obtained from the SIMBAD website[10]. When it was not present, magnitude information (B and V magnitudes) were looked for and a Hubble diagram (redshift versus B magnitude) was used to estimate the photometric redshift of the source.

In all cases, an attempt was made to find a counterpart in the SDSS catalog, to get magnitude (*ugriz*) information if none was available in the literature. However, only 143 sources appeared to have SDSS counterparts, with 25 of them possible but not confirmed[11]. For 44 sources in the sample, no magnitude information was available in the literature, but the sources had a confirmed SDSS counterpart; the B magnitude was then estimated from the *ugriz* magnitude information following Fukugita, Shimasaku & Ichikawa (1995):

$$B = g + 0.217 + 0.419(g - r) \tag{2.1}$$

The distribution of B magnitude is shown in figure 2.1, where the ratio of the different optical types (QSOs, Seyferts, BL Lacs or galaxies) is represented.

To complete the Hubble diagram, sources from 2dFGRS (Sadler et al., 1999) were used in addition to the data from our sample. This survey is suitable for our purpose because the optical hosts of radio galaxies are a very uniform population of massive elliptical galaxies such as the galaxies in 2dFGRS. Figure 2.2 shows the complete Hubble diagram, for all sources as well as for the sub-sample of galaxies only (excluding QSOs). Both diagrams include sources from our sample as well as sources from 2dFGRS.

A polynomial was then fitted to the points to get the relation between redshift and B magnitude, as shown in figure 2.3:

$$log(z) = 0.0011B^2 + 0.138B - 3.7 \tag{2.2}$$

[9]One of the source found with NVSS was discarded as it was impossible to find the nature of the object in the literature. This object was possibly a globular cluster, therefore ignoring it has no impact on the sample.

[10]http:simbad.harvard.edu

[11]"possible but not confirmed" means that a SDSS source was found in a 2" radius from the radio source, but there was no indication in the SDSS description of the source that it also belongs to the FIRST survey.

Out of the 285 sources in the sample, 49 had no redshift in SIMBAD or in the SDSS catalog. Estimates from the B magnitude were used for 39 of these sources; 10 sources remained unidentified. Note that redshifts estimated using the Hubble diagram correspond to photometric redshifts, which are close but different from the actual redshifts of the sources.

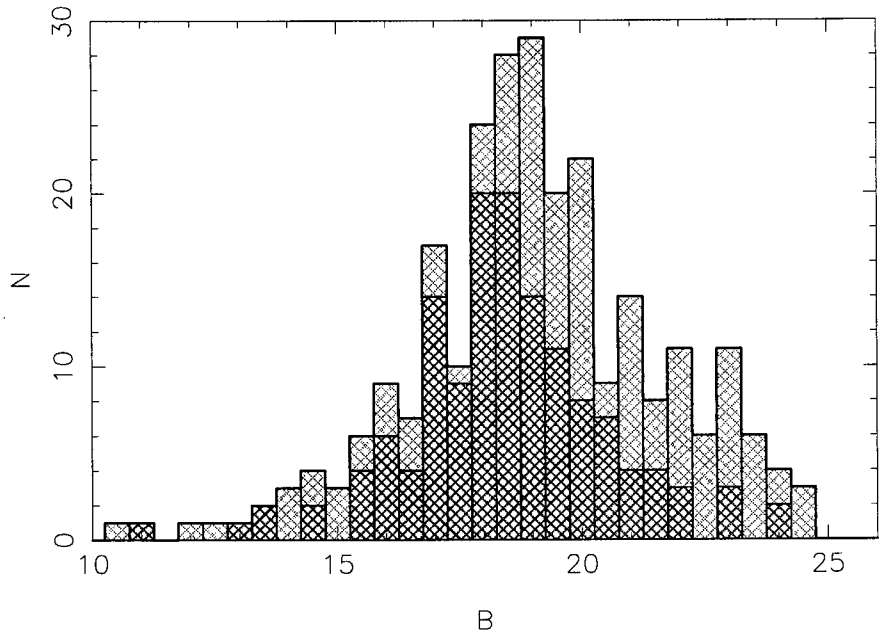

Figure 2.1: Distribution of the 275 B magnitudes for our sample. Each column shows the number of QSOs, Seyferts and BL Lacs (in red) and the number of galaxies (in light blue). The magnitudes were either found in SIMBAD or computed using the g and r magnitudes information from SDSS.

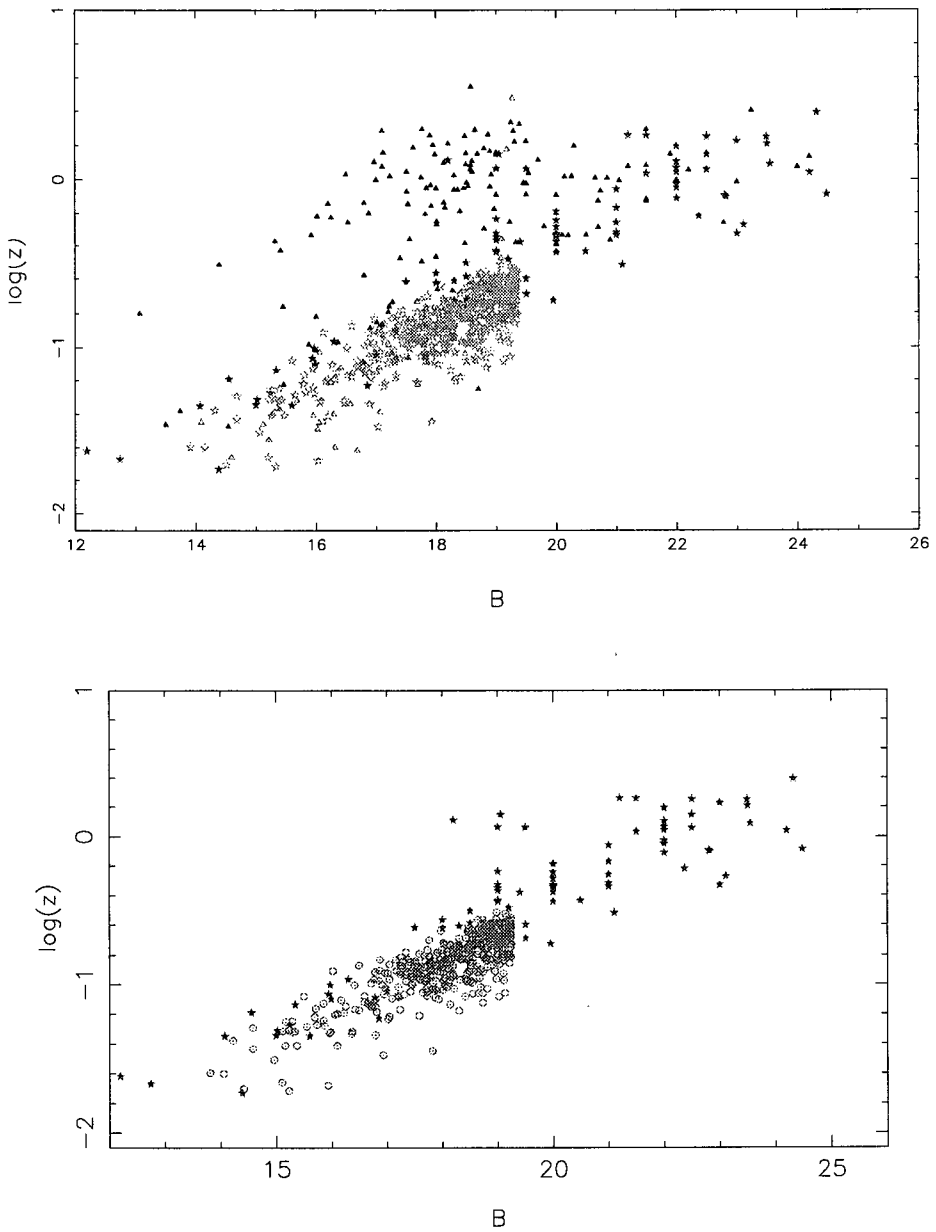

Figure 2.2: Top Panel: Hubble diagram relating B magnitude and redshift for all sources from the FIRST and Sadler et al. (1999) 2dFGRS samples. Bottom Panel: Hubble diagram relating B magnitude and redshift for galaxies only.
(red filled stars: FIRST galaxies; orange open stars/pink dotted circles: 2dFGRS galaxies; blue filled triangles: FIRST QSOs; open light blue triangles: 2dFGRS QSOs.)

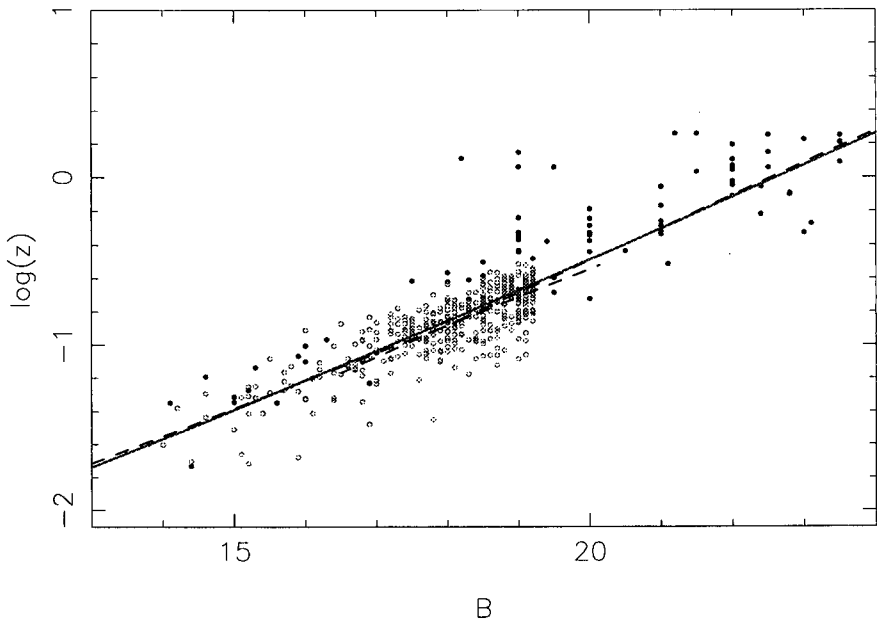

Figure 2.3: Linear (dash black line) and polynomial (red line) fit to the Hubble diagram relating B magnitude and redshift. Redshifts were estimated for 39 sources of the primary sample using this polynomial.
(blue filled circles: FIRST data; pink open circles: 2dFGRS data).

Testing of the redshift estimate

To make sure the redshift estimate used was valid, luminosity distributions were derived using redshift estimated from B and V magnitudes separately. For this purpose, only sources with both B and V magnitudes were used, to ensure that both distribution were done with the same number of objects.

The polynomial fit for the log(z) vs. B magnitude diagram is (see figure 2.4, top panel):

$$log(z) = -3.72 + 0.134B + 0.0013B^2 \tag{2.3}$$

and for the log(z) vs. V magnitude diagram (see figure 2.4, bottom panel):

$$log(z) = -4.22 + 0.222V - 0.0014V^2 \tag{2.4}$$

In both panels, only the sub-sample of galaxies is shown (excluding QSOs).

The resulting luminosity distributions are shown in figure 2.5. Since they look very similar, it was concluded that the redshift estimate done using B magnitudes was valid.

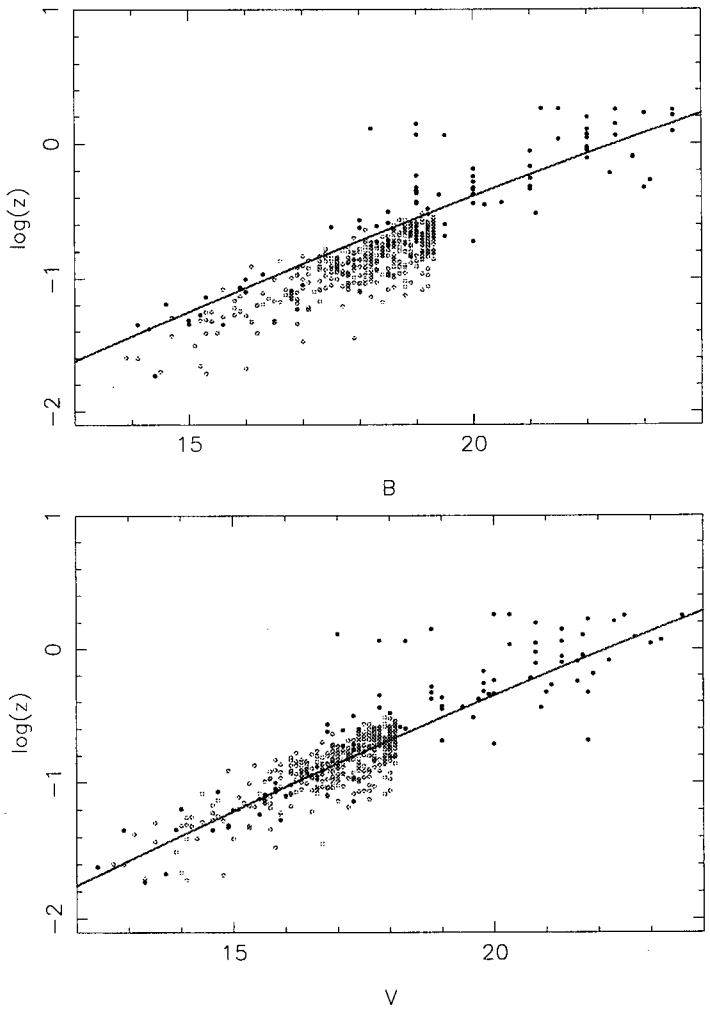

Figure 2.4: Polynomial fits to the Hubble diagram relating B magnitude and redshift (top panel) and relating V magnitude and redshift (bottom panel) used in comparing redshift estimates using one or the other magnitude.
(blue filled circles: FIRST data; pink open circles: 2dFGRS data).

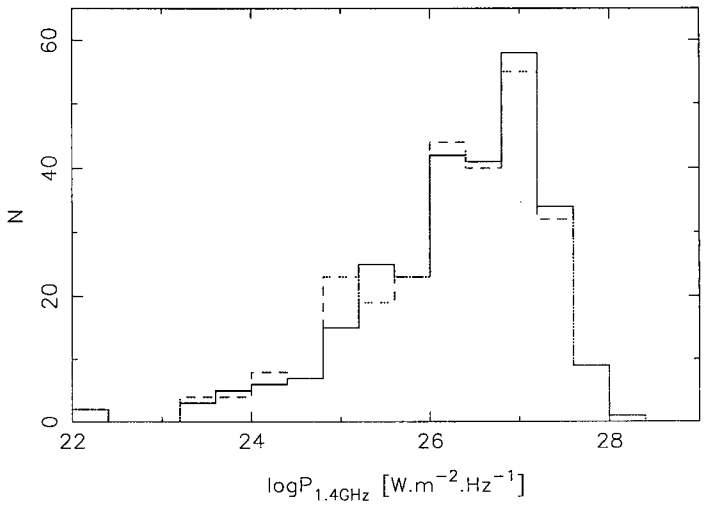

Figure 2.5: Luminosity distributions ($q_0 = 0.5$) derived using redshifts estimated from the B (solid black) and V (dash red) magnitudes. Since they both look very similar, it was concluded that the redshift estimate done using B magnitudes was valid.

2.1.2 Classification

Several processes were used to determine the type of each source in the sample.

For some sources, type was specified in SIMBAD, especially sources from the 3CR catalog (Laing, Riley & Longair, 1983). For the other sources, type was determined by looking at the contour plots (see Appendix C) of the FIRST and NVSS radio maps, downloaded in $10' \times 10'$ format from the respective websites.

In the case of compact sources (based on the major axis size given in the FIRST survey), they were labeled as compact (as opposed to resolved component of an extended source) if the FIRST and NVSS flux densities were similar[12]. Figure 2.7 illustrate this similarity between FIRST and NVSS fluxes for sources in our sample. If the contour plots were showing distinct hot spots at the edge of the lobes, and the lobes were aligned, the source was classified as an FRII. Most irregular looking sources were classified as FRI.

In some cases, the morphological typing was more difficult; in 3 cases, the source was dropped from the primary sample after looking at the contour plots, reducing the total number of sources to 282. Those special sources are described in more details in Appendix D.

Table 2.1: Number of source for each type

radio type	FRI	FRII	Compact	Other
number	39	94	145	4
%	13.8	33.3	51.4	1.4

This complete the construction of our sample. The complete table of information can be found in Appendix A.1 (an sample of the table is shown in table 2.2). Figure 2.6 shows a map of the sources in the primary sample as well as the area of the FIRST survey.

2.2 Study of the sample

Throughout this thesis, the following cosmology is used: $q_0 = 0.5$ and $H_0 = 50\ km/s/Mpc$[13].

This provides the following relations between co-moving distance and redshift:

$$D = \frac{2c}{H_0}\left(1 - \frac{1}{\sqrt{1+z}}\right) \tag{2.5}$$

as well as relation between flux density and luminosity (assuming a spectral index $\alpha = 0.75$[14], in the sense $S \propto \nu^{-\alpha}$):

$$S = \frac{P}{D^2(1+z)^{1.75}} \tag{2.6}$$

[12] $0.9 \leq S_{FIRST}/S_{NVSS} \leq 1.1$

[13] This cosmology was chosen for comparison with previous works, such as Wall, Pearson & Longair (1980).

2.2.1 Luminosity distributions

The relative differential source count for the sample is compared to the source count for the FIRST catalogue in figure 2.8. Note that the values of the source count for our sample are (in general) higher that the value of the source count derived from FIRST. This is due to the fact that the multiples components of extended sources resolved in FIRST have been combined to form one source, increasing the number of sources with $S \geq 1.3Jy$.

The luminosity (figure 2.9) and redshift (figure 2.10) distributions were also compiled for the entire sample as well as for extended sources only (ie: FRI and FRII sources). Note that the range of luminosity for our sample goes from $logP \sim 24$ to $logP \sim 28$.

A primary requirement for this type of analysis is a well-defined luminosity distribution. However, the range of luminosities covered by the FIRST sample is quite small ($24 \leq logP \leq 28$). To improve it at low powers, data from the 2dFGRS survey derived by Sadler et al. (2002) were used. Indeed, as seen on figure 2.11, the 2dFGRS distribution goes from $logP \sim 22$ to $logP \sim 26$, providing a better range in luminosity. This combination of the luminosity distribution of our sample with the 2dFGRS data is possible since no evolution is observed for source with $logP \leq 24$.

In order to normalized the 2dFGRS data to the same flux limit of 1.3Jy as the primary sample, an integral source count (which represents the cumulative number of sources observed above a given flux limit) at 1.4GHz was derived by fitting a polynomial to the relative differential source count computed from the FIRST survey (see §2.2.2) and integrating the result, as shown in figures 2.12 and 2.13. The ratio of the integrated count at 1.3Jy to its value at 3mJy (flux limit of the Sadler sample) gives the normalization factor. The combined luminosity distributions are shown on figure 2.14. The luminosity range now goes from $logP \sim 22$ to $logP \sim 28$. The contribution of the 2dFGRS sample to the luminosity distribution is small after normalization, but it is still enough to better define the distribution.
The luminosity distribution data are tabulated in Appendix A.2.

[14]This assumed value of the spectral index is wrong for QSOs. Their luminosity was therefore overestimated in our sample. However, since compact objects will be taken out of the sample, this has no impact on our study.

Table 2.2: Primary Sample (the complete table can be found in Appendix A.1.)
Columns 1 and 2 correspond to the right ascension and declination of the radio identification; column 3 gives the name of the source; columns 4 and 5 correspond to the flux density from FIRST and NVSS respectively, in mJy; column 6 and 7 correspond to the B and V magnitudes; column 8 describes the source morphology (Co for compact, I for FRI, II for FRII, U for other types); column 9 corresponds to redshift; column 10 gives information on the SDSS identification (c for confirmed identification, u for possible but not confirmed, n for none) as well as information on the magnitudes and redshift estimation (B and V when the magnitudes were estimated from SDSS, H when the redshift was estimated from the Hubble diagram).

RA	DEC	Name	S_{FIRST} (mJy)	S_{NVSS} (mJy)	B	V	morph.	z	
00 06 22.611	-00 04 24.48	3C 002	3879.24	3897.6	20.14	19.35	Co	1.0370	c
00 13 10.910	+00 51 42.40	3C 005	1600.68	1620.1	22.37	20.73	II	0.6060	u A
00 22 25.437	+00 14 56.08	PKS 0019-00	2938.88	3009.2	21.10	19.57	Co	0.3050	c V
00 37 04.060	-01 09 09.40	3C 015	3703.23	4067.1	15.34	17.33	I	0.0730	c V
00 38 20.410	-02 07 40.40	3C 017	6015.11	6187.8	18.02	0.00	I	0.2196	n
00 57 34.150	-01 22 58.40	3C 029	2087.33	5365.4	14.07	0.00	II	0.0448	n
00 59 05.511	+00 06 51.70	PKS 0056-00	2415.95	2508.8	17.53	17.33	Co	0.7170	c
01 25 28.853	-00 05 56.20	PKS 0122-00	1524.09	1540.2	16.50	16.70	Co	1.0700	c
01 26 4.670	-01 24 1.90	NGC 547 (3C 40)	106.29	2010.1	14.38	13.34	I	0.0185	n
02 20 54.052	-01 56 55.16	3C 063	3123.21	3419.2	18.50	0.00	I	0.1750	n
02 42 40.720	-00 00 47.70	M77	4261.56	4848.1	8.91	9.77	I	0.0038	c V
06 55 14.780	+54 09 00.00	3C 171	3636.91	3680.0	18.89	18.90	II	0.2384	n
07 02 53.639	+44 31 11.92	4C 44.15	2433.08	2397.4	0.00	0.00	Co	0.0000	n
07 06 48.083	+46 47 56.39	B3 0703+468	1589.99	1584.9	23.10	0.00	Co	1.4941	nH
07 13 38.169	+43 49 17.06	B0710+439	2032.11	2011.4	20.70	0.00	Co	0.5180	n
07 14 24.813	+35 34 39.70	B0711+35	1533.45	1467.1	18.20	17.00	Co	1.6260	n
07 16 41.090	+53 23 10.30	4C 53.16	1298.23	1501.4	14.55	14.00	II	0.0643	n
07 35 55.549	+33 07 9.44	4C 33.21	2423.09	2473.1	21.00	20.90	Co	0.5187	cHV
07 38 7.379	+17 42 19.60	J0738+1742	1101.95	2257.7	15.32	14.85	Co	0.4240	c
07 41 10.698	+31 12 0.31	J0741+3111	2071.27	2284.3	16.88	17.00	Co	0.6313	c B
07 45 42.131	+31 42 52.60	4C 31.30	1163.63	1357.8	15.92	16.00	II	0.4620	c B

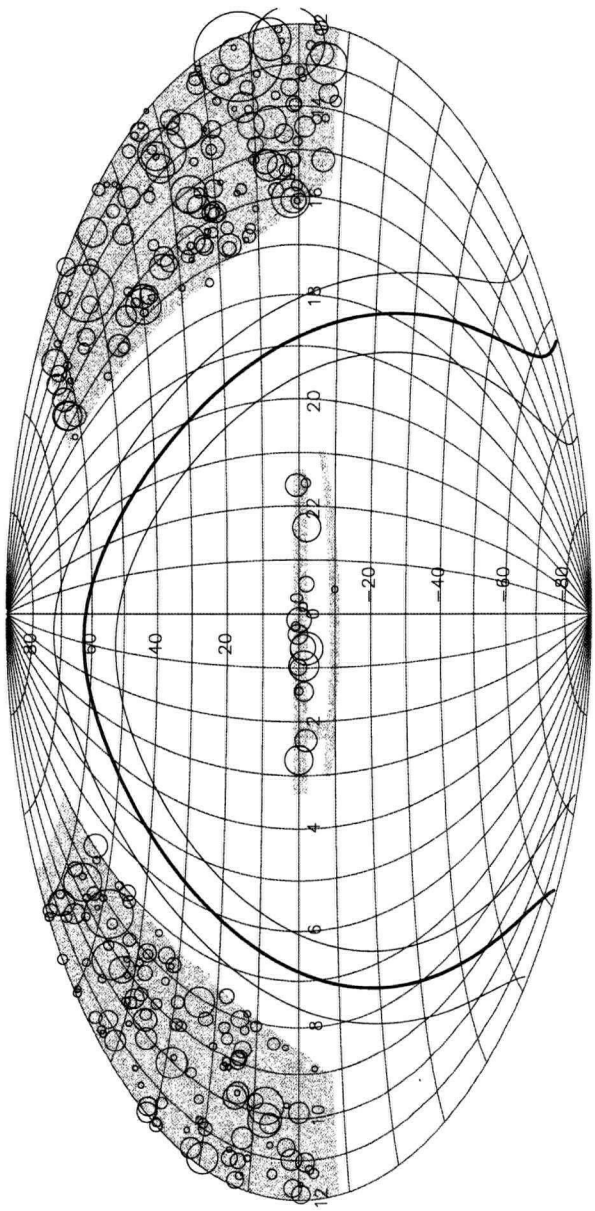

Figure 2.6: Map of the sources (Aitoff projection) from the primary sample. The grey area corresponds to the area covered by the FIRST survey. The radius of each circle is proportional to the flux density of each source.

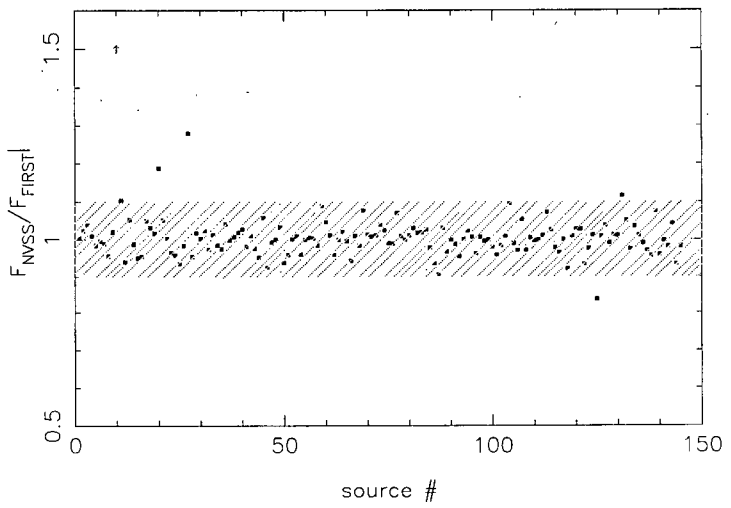

Figure 2.7: Ratio of FIRST flux to NVSS flux for objects classified as compact. The yellow hatched region correspond to the $0.9 \leq S_{FIRST}/S_{NVSS} \leq 1.1$ region. This figure illustrate that, in the case of compact sources (as opposed to resolved component of an extended source), the FIRST and NVSS fluxes are very similar.

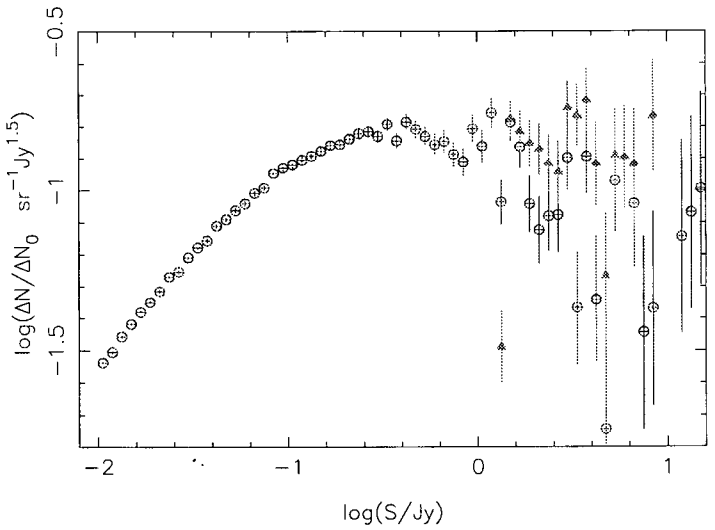

Figure 2.8: Comparison of the relative differential source count for the FIRST catalogue (red open circles) and for the original 285 sources of the primary sample (green filled triangle). The error bars correspond to $\sqrt{N}$. Note that the values of the source count for our sample are (in general) higher that the value of the source count derived from FIRST. This is due to the fact that the multiples components of extended sources resolved in FIRST have been combined to form one source, increasing the number of sources with $S \geq 1.3Jy$.

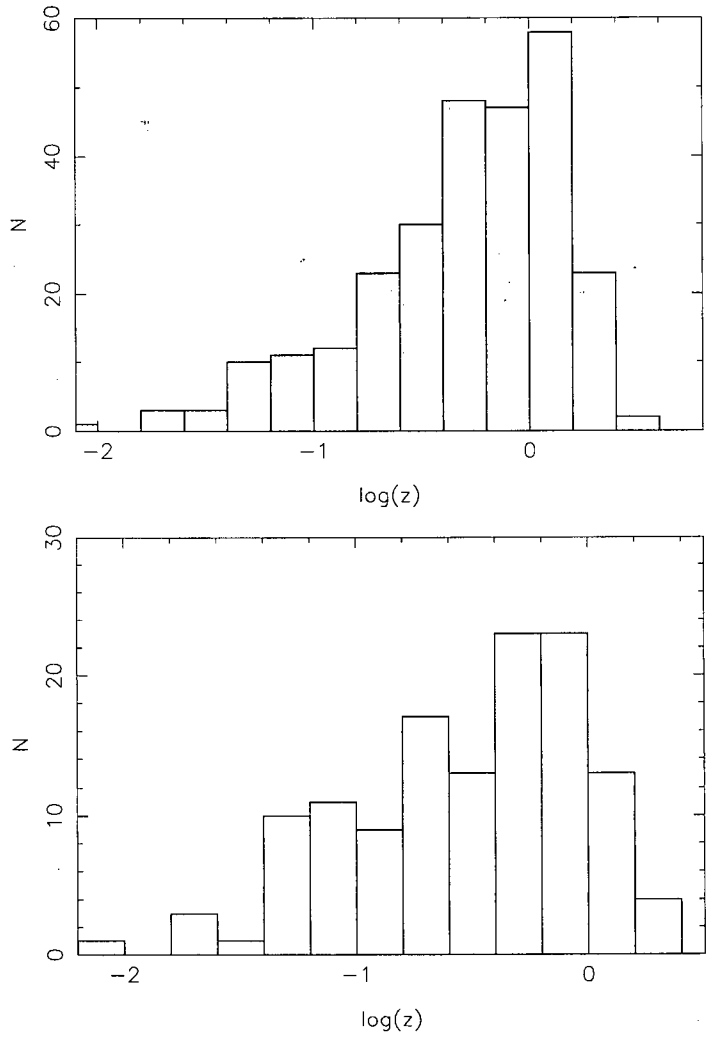

Figure 2.9: Redshift distributions for the final 274 sources with redshift of the primary sample (top panel) and the 130 sources with redshift of the sub-sample of extended sources (bottom panel).

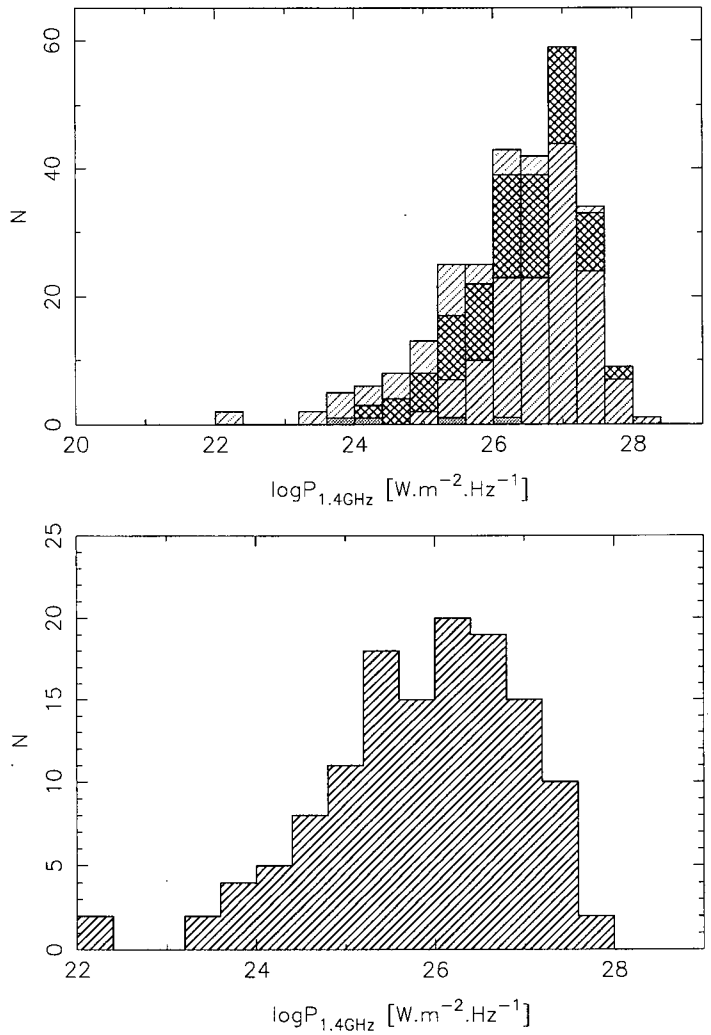

Figure 2.10: Luminosity distributions ($q_0 = 0.5$) for the 274 sources with redshift of primary sample (top panel) and for the 130 sources with redshift of the sub-sample of extended sources (bottom panel). In both cases, the range in luminosity goes from $logP \sim 24$ to $logP \sim 28$, which makes the distribution not well enough define for our analysis. Top panel: Red hatched correspond to object identified as compact, blue cross-hatched for objects identified as FRII, green hatched for objects identified as FRI, grey for other types of object.

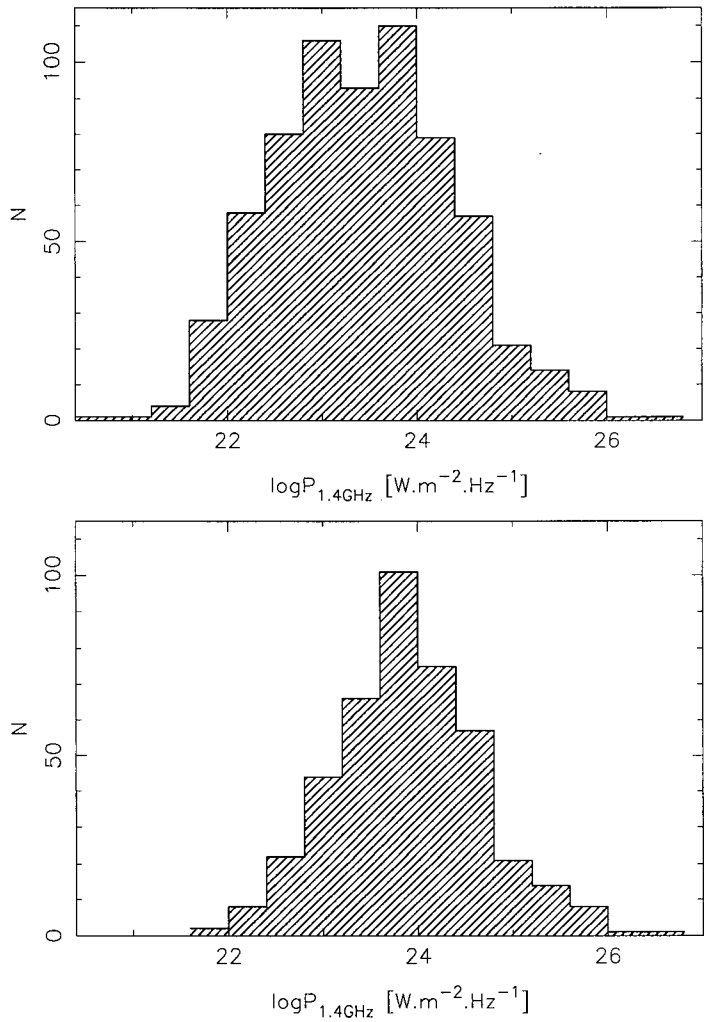

Figure 2.11: Luminosity distributions for the 2dFGRS sample, AGN and starburst galaxies (top panel) and AGN only (bottom panel) (Sadler et al., 2002). In both cases, the range in luminosity goes from $logP \sim 22$ to $logP \sim 26$, making the 2dFGRS sample a good complementary sample to our luminosity distribution. This combination of the luminosity distribution of our sample with the 2dFGRS data is possible since no evolution is observed for source with $logP \leq 24$.

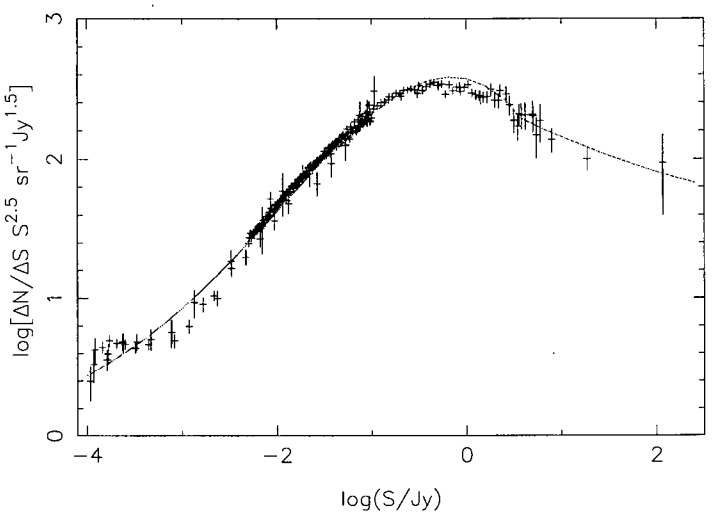

Figure 2.12: Polynomial fit to the relative differential source count. The source count is actually fitted by two polynomials: one for $logS \leq 0.5$ and one for $logS > 0.5$. This polynomial fit is used to compute the integrated source count.

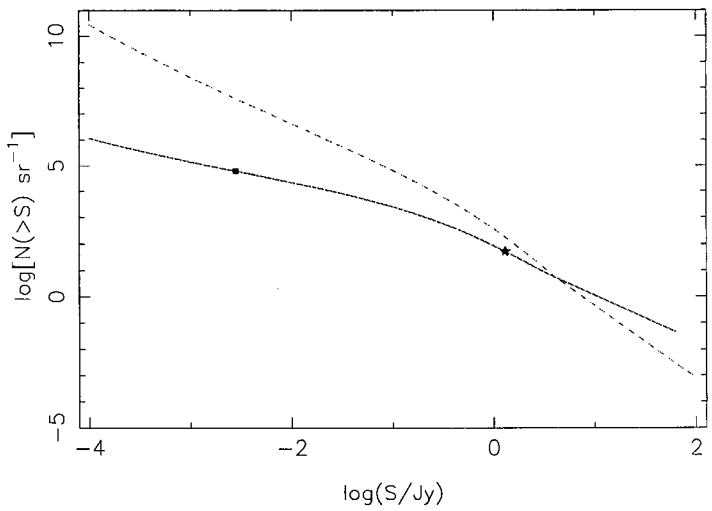

Figure 2.13: Both the differential source count $log(dN/dS)$ (dash line) and the integrated source count (solid line) are plotted. The value of the integrated count for the FIRST sample ($S_{lim} = 1.3Jy$) is represented by the red star; the value of the integrated count for the 2dFGRS sample ($S_{lim} = 3mJy$) is represented by the blue square. The ratio of the values of the integrated source count is used to normalize the flux limit of the 2dFGRS sample to the flux limit of our sample.

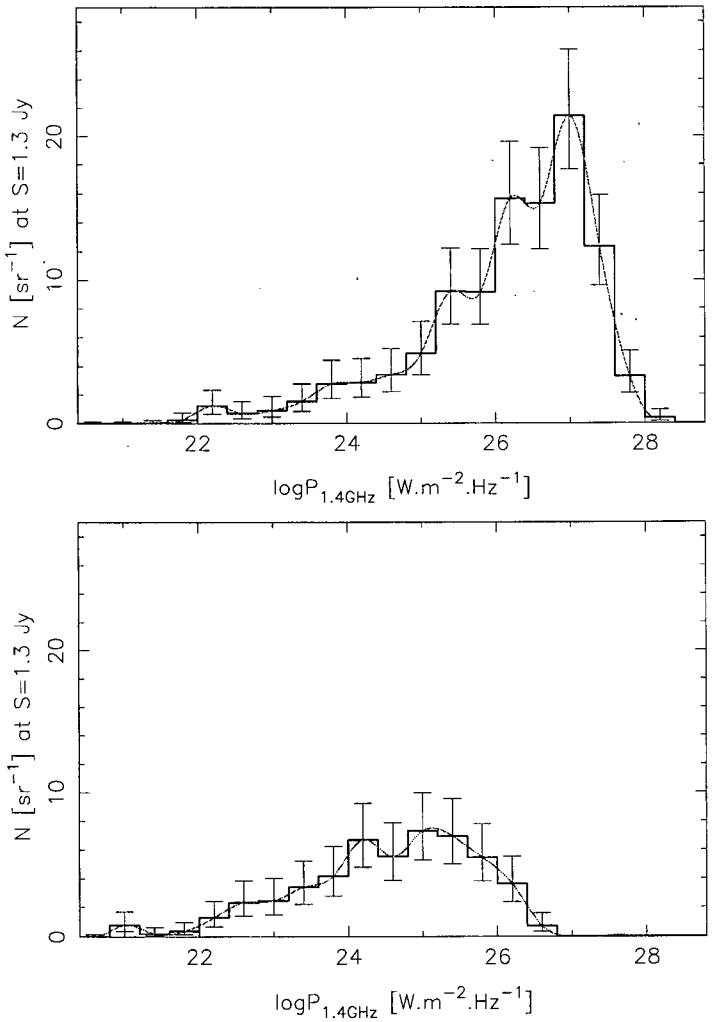

Figure 2.14: Combined luminosity distributions of the FIRST and 2dFGRS samples for the entire sample (top panel) and the extended sources only (bottom panel). The solid lines show the smoothed version of the distributions. The errors bars correspond to $\sqrt{N}$. The luminosity range goes now from $logP \sim 22$ to $logP \sim 28$. The contribution of the 2dFGRS sample to the luminosity distribution is small after normalization, but it is still enough to better define the distribution.

2.2.2 Source Count

The relative differential source count $\Delta N/\Delta N_0$ was computed for sources in the FIRST catalog, using $\Delta N_0 = 1200\Delta(S^{-1.5})$ as the source count expected in Euclidean space. Due to the low number of AGN sources at the lower and higher end of the source count, only sources with $-2.6 \leq logS \leq 0.8$ were used.

To improve the lower and higher end of the source count, data from various other surveys were used. The complete list of all the 1.4GHz source count data used is described in table 2.3 and the count is tabulated in Appendix A.3.
The resulting relative differential source count $\Delta N/\Delta N_0$ is shown in figure 2.15.

The relative differential source count was also computed with the FIRST data for extended and compact sources separately. For this purpose, each source with major axis $majA > 1.5''$ in the FIRST catalog was considered extended; otherwise, a cross-check was performed using the NVSS catalog by comparing the flux densities of the source and its NVSS counterpart (defined as any source in NVSS less than 2" away from the FIRST source). Indeed, for compact sources, the flux densities in both surveys are very close (see figure 2.7). Therefore, if the ratio of the flux densities was in the range [0.9,1.1], the source was considered compact. If not, the source was denoted as extended.

The resulting source counts (for the entire FIRST catalogue as well as for compact and extended sources separately) are shown in figure 2.16, and the proportion of compact sources in the FIRST survey is shown in figure 2.17.

Table 2.3: Survey used in the source count

Survey	Flux density limit	Approx. number of objects	Approx. area (sr)	Reference
3CR	9Jy	250	10.22	Bridle et al. (1972)
Westerbork-NRAO	2Jy	240	4.3	Fomalont et al. (1974)
GB2	90mJy	1500	0.28	Machalski (1978)
5C12	9mJy	65	0.015	Benn et al. (1982)
VLA	5mJy	160	3.610^{-3}	Condon, Condon & Hazard (1982)
VLA	70μJy	100	10^{-4}	Mitchell & Condon (1985)
Phoenix	60μJy	1250	1.410^{-3}	Hopkins et al. (2003)
ATESP	0.5mJy	1600	810^{-3}	Prandoni et al. (2001)
FIRST	1mJy	800,000	2.74	White et al. (1997)
NVSS	2.3mJy	1.7 million	10.3	Condon et al. (1998)

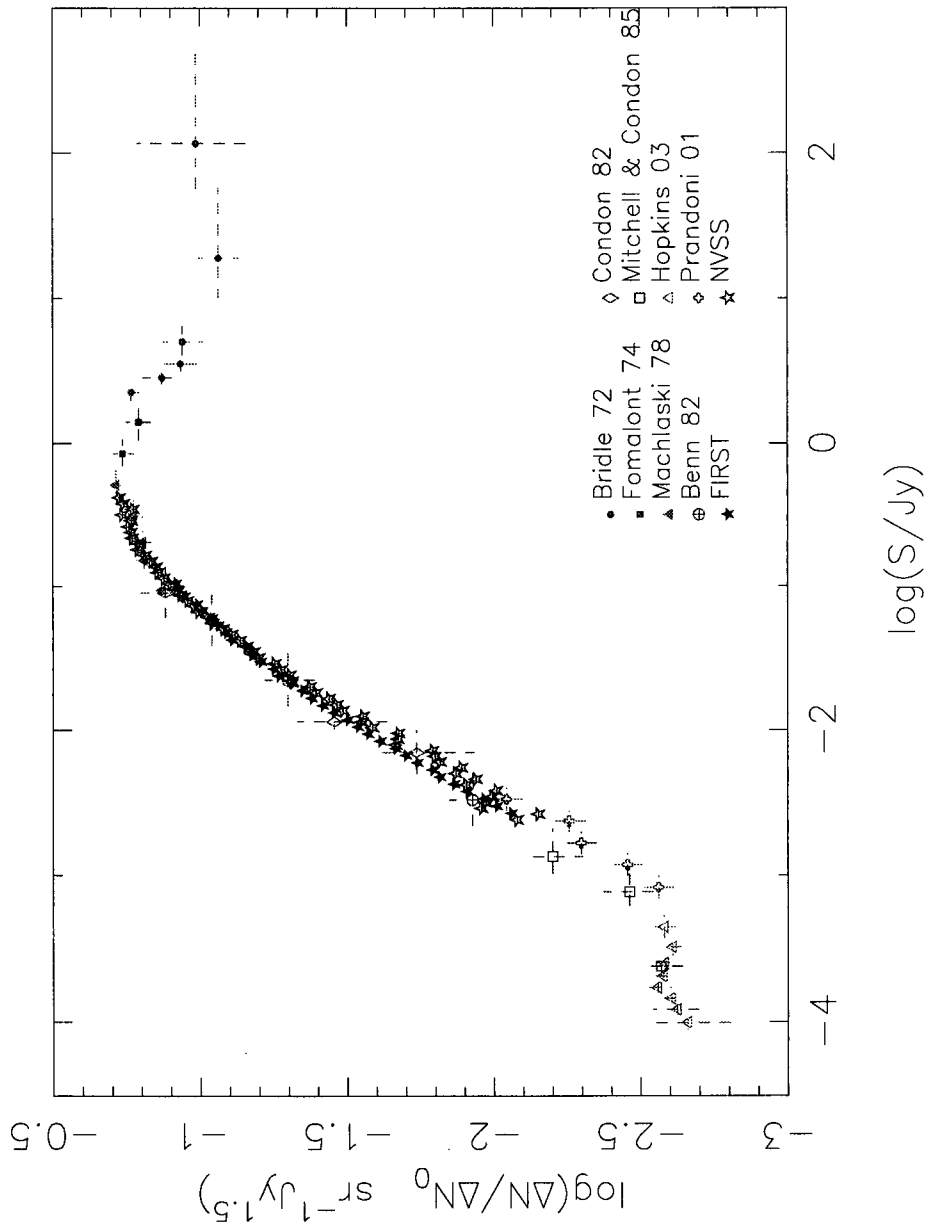

Figure 2.15: Relative differential source count $\Delta N/\Delta N_0$ where $\Delta N_0 = 1200S^{1.5}$. The error bars correspond to $\sqrt{N}$. Each source count data used to compile this source count is represented by a different symbol.

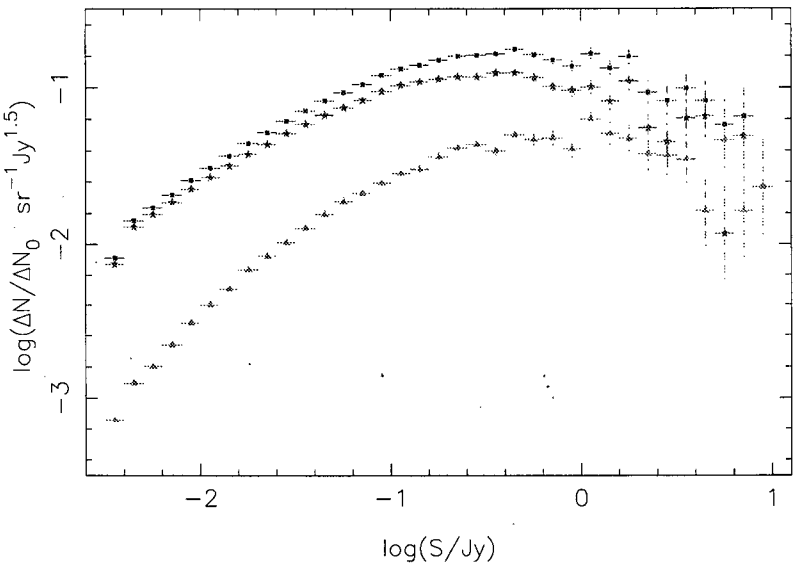

Figure 2.16: Relative differential source count for all sources in the FIRST catalogue (black squares), extended sources only (pink stars) and compact sources only (green triangles). The error bars correspond to $\sqrt{N}$. To separate compact sources from extended ones, each source with major axis $majA > 1.5''$ in the FIRST catalog was considered extended; otherwise, a cross-check was performed using the NVSS catalog by comparing the flux densities of the source and its NVSS counterpart. If the ratio of the flux densities was in the range [0.9,1.1], the source was considered compact. If not, the source was denoted as extended.

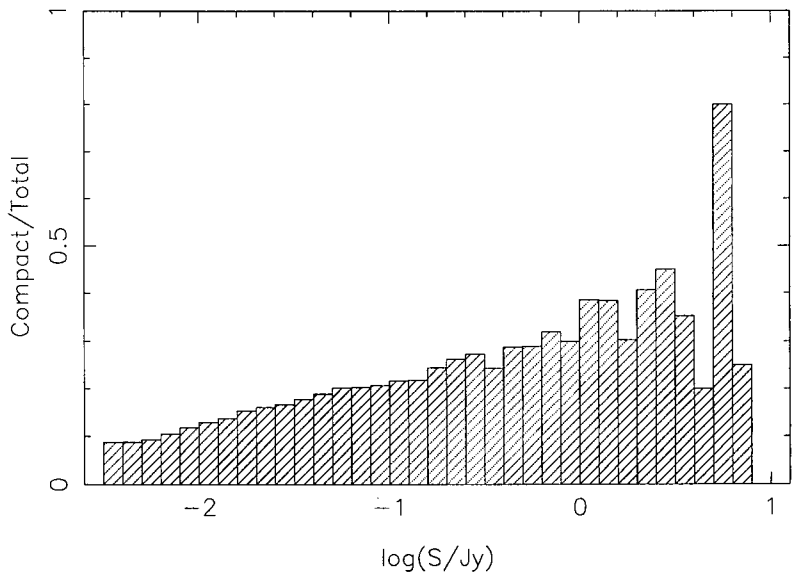

Figure 2.17: Proportion of compact sources to the total number of sources in each flux density bins for the FIRST catalogue.

Chapter 3

Modeling of the luminosity function

3.1 The Wall Pearson Longair modeling

Early models used fixed local luminosity function (not changing with varying evolution functions) to derive the luminosity function at different epoch. However, the WPL modeling technique (Wall, Pearson & Longair, 1980) was based on the idea that the evolution function modifies the local luminosity function.

3.1.1 The WPL technique

Steps in the WPL technique can be described as follow:

1. Define an evolution function F(P,z).

2. Assuming that the source count at a given frequency ν is composed of a single source population (hence, for which a single spectral index is a good approximation and one luminosity function is applicable), factorize the luminosity function $\rho(P, z)$ in the following way:

$$\rho(P, z) = F(P, z)\rho_0(P) \tag{3.1}$$

where $\rho_0(P)$ is the local luminosity function.

3. Assume a cosmology[15], providing the relation between flux density and luminosity

$$S = P/D^2(1+z)^{1+\alpha} \tag{3.2}$$

where α is the spectral index defined in the sense $S \propto \nu^{-\alpha}$ It also provides the relation between co-moving volume and redshift

$$\Delta V(z) = \frac{4}{3}\pi\Delta D^3 \tag{3.3}$$

where the effective distance D goes according to the relation (in Friedman world models $\Lambda = 0$)

$$D = \frac{2c}{H_0\Omega^2(1+z)}[\Omega z - (\Omega - 2))((\Omega z + 1)^{1/2} - 1)] \tag{3.4}$$

4. Populate the P-z plane with F(P,z) and $S(P,z)$, computed for each $(\Delta P_i, \Delta z_j)$ bin.

5. Compute an estimate of ρ_0 from the data luminosity distribution using

$$\rho_0(P)dP = n_i \Delta P_i / \sum_{j=1}^{j(S_0)} F(P_i, z_j) \Delta V(z_j) \tag{3.5}$$

where n_i is the value of the data luminosity distribution in the given ΔP_i bin and where $j(S_0)$ is the redshift index at which a source with luminosity P_i has a flux density S_0, the flux limit of the sample used.

6. Compute the model source count and the model luminosity distribution where each $(\Delta P_i, \Delta z_j)$ bin contributes

$$n_{ij} = \frac{1}{4\pi} F(P_i, z_i) \rho_0(P_i) \Delta V(z_j) \ sources \ sr^{-1} \tag{3.6}$$

7. Compare the modeled source count and luminosity distribution with the data source count and luminosity distribution. If the results are unsatisfactory, go back to step 1 and adjust F(P,z).

In this thesis, $q_0 = 0.5$ and $H_0 = 50 km/s/Mpc$ was used. The P-z plane was divided into 1000 bins for $20 \leq logP \leq 30$ and 1000 bins for $0 \leq log(1+z) \leq 1$. Since our data luminosity distribution went only up to logP=27.8, the LLF for $27.8 \leq logP \leq 30$ was extrapolated.

For each model (described in the next section), the best parameters were found by fitting the modeled source count to the data using a maximum likelyhood method, assuming Poisson noise.

3.1.2 Description of the models

Only the three models described as "satisfactory evolution models" in Wall, Pearson & Longair (1980) were used in this thesis to model the RLF. The models are the following:

model 1 Exponential law evolution.
$F = exp[M(P)(1-(1+z)^{-3/2})]$
where

$$M(P) = \begin{cases} 0 & : \ P < P_1 \\ M_{max}(logP_1 - logP)/(logP_1 - logP_2) & : \ P_1 \leq P \leq P_2 \\ M_{max} & : \ P > P_2 \end{cases}$$

This model has therefore 3 free parameters: M_{max}, P_1 and P_2.

[15]Note that as stated by Dunlop & Peacock (1990), it is not necessary to repeat the modeling for different cosmologies as the RLFs for two different geometries are related by: $\rho_1(P_1, z)\frac{dV_1}{dz} = \rho_2(P_2, z)\frac{dV_2}{dz}$

model 2 Exponential law evolution, with redshift cut-off.
$F = \begin{cases} exp[M(P)(1-(1+z)^{-3/2})] & z \leq zc \\ 0 & z > z_c \end{cases}$
where M(P) is defined as in model 1.
This model has therefore 4 free parameters: M_{max}, P_1, P_2 and z_c.

model 3 Exponential law evolution, with $P_t = alog(z) + b$.
$F = X_1 + \phi X_2$
where
$\phi = exp[M(1-(1+z)^{-3/2})]$
$X_1 = (\frac{P_t}{P})^n/[1+(\frac{P_t}{P})^n]$
$X_2 = 1/[1+(\frac{P_t}{P})^n]$
This model has therefore 4 free parameters: M, a, b and n.

In each case, a normalization parameter was added, increasing the number of free parameter by one for each model. This extra parameter is multiplied to the modeled source count to get the best fit model. It does not change the shape of the modeled source count.

3.1.3 Parameters estimation

The best fit parameters in each cases were determined by comparing the data and modeled relative differential source count using a maximum likelyhood technique (based on Poisson noise).

$$\mathcal{L} = exp[-SC_{model}] \times \frac{(SC_{model})^{SC_{data}}}{SC_{data}!} \tag{3.7}$$

where SC_{data} is the value of the data source count at a given flux density, SC_{model} is the value of the modeled source count at the same flux density and $\mathcal{L}$ is the value of the likelyhood.
The minimum value of the likelyhood was found using a downhill-simplex method.

For each model, the reduced χ^2value for the best fitting parameters was computed.

$$\chi^2 = \sum \left(\frac{SC_{data} - SC_{model}}{SC_{model}} \right)^2 \tag{3.8}$$

For the purpose of this thesis, these models were applied to two types of sample: the entire primary sample (all source types included - §3.2) and the extended sources from the primary sample (restricted to sources labeled as FRI and FRII - §3.3). In each case, a comparison plot of the modeled and data luminosity distribution is shown. Indeed, following the WPL modeling technique, the output luminosity distribution should be identical to the input one, providing a way to test if the modeling

was done properly. However, data being sparse for $logP \leq 24$, a combination of local luminosity function found in Sadler et al. (2002) and of the modeled local luminosity function was used to improve the local luminosity function at low luminosities. Due to this fact, the modeled and data luminosity distributions differ for $logP \leq 24$.

3.2 Modeling of the luminosity function on the entire primary sample

Only the AGN part of the source count ($logS \geq -3$) was used to determine the best fit parameters for the models. Indeed, starburst galaxies do not follow the same evolution than AGNs, and can therefore not be taken into account in modeling AGN evolution.

Finding the best fit parameters for model 2 was attempted, but the value of the redshift cutoff was quite high ($z_c = 8.55$), making model 2 equivalent to model 1. The results of model 2 were therefore discarded.

The modeled redshift distribution as well as the comparison of the modeled and data luminosity distribution for the entire primary sample are shown in figure 3.1 and 3.2. As discussed in section 3.1.3, both luminosity distributions being similar shows that the modeling was done successfully.

For each model, contour plots of the evolution function as a function of redshift for different luminosities and contour plots of the evolution function in the (P,z) plane (figures 3.3 and 3.8) are shown, as well as plots of the best fit to the relative differential source count (figures 3.4 and 3.9) and of the luminosity function with respect to luminosity (figures 3.6 and 3.10) and redshift (figures 3.7 and 3.11).

Table 3.1: Results from modeling of the luminosity function on the entire primary sample

model #	Best Fit Parameters	χ^2_{red} ($\nu = 29$)
1	$M_{max} = 10.7827$ $P_1 = 22.7029$ $P_2 = 28.4256$	73.65
3	$M = 9.8030$ $a = 3.8228$ $b = 26.4076$ $n = 0.6754$	24.56

In both cases, the value of χ^2_{red} is very high[16], indicating that the models are not suitable anymore to describe the data. Indeed, since Wall, Pearson & Longair (1980), the number of available radio data has increased tremendously, giving us the possibility to compute source count to a high level of accuracy. This implies that, when trying to fit the modeled source count to the data one, any point of the model not coinciding exactly with one of the recent source count data point will be many sigmas away from that point. This is illustrated in figure 3.5, showing a close-up of the source count fitting plot for model 1. The points located at $logS = -2.35$, $logS = -1.95$ and $logS = -1.55$ correspond to source count data computed from

FIRST, while the other points are source count data from previous surveys[17]. It is obvious from this figure that the contributions to $\chi^2$of the model points associated with the FIRST source count points will be large. This shows that the models used by Wall, Pearson & Longair (1980) are now too simple to describe the data.

Nevertheless, if the χ^2value for each models is only used as a comparison tool between them (the closer ${\chi^2}_{red}$ to 1, the better the fit), then model 3 seems to be the best fitting model.

A comparison plot of the local luminosity functions is given in figure 3.12. This illustrate very well the dependence of the local luminosity function on the evolution function. The comparison was done for $logP \geq 24.6$ as the local luminosity functions at lower powers are similar (no evolution).

In addition to the modeling of the luminosity function, the V/V_{max} statistics (Schmidt, 1968) was computed using the radio flux limit only. The results are shown in figures 3.13 and 3.14.

The value of the statistics was found to be $\langle V/V_{max} \rangle = 0.6113$ with $\sigma = 0.0174$, implying an increasing number of sources with epoch, as expected. The value of $\langle V/V_{max} \rangle$ is a little be low though, probably due to errors induced by the fact that the redshifts estimated using the Hubble diagram are photometric redshifts and not the actual redshifts of the sources.

[16]The reduced $\chi^2$is defined as: ${\chi^2}_{red} = \frac{\chi^2}{\nu}$

[17]see figure 2.15 or table 2.3 for details

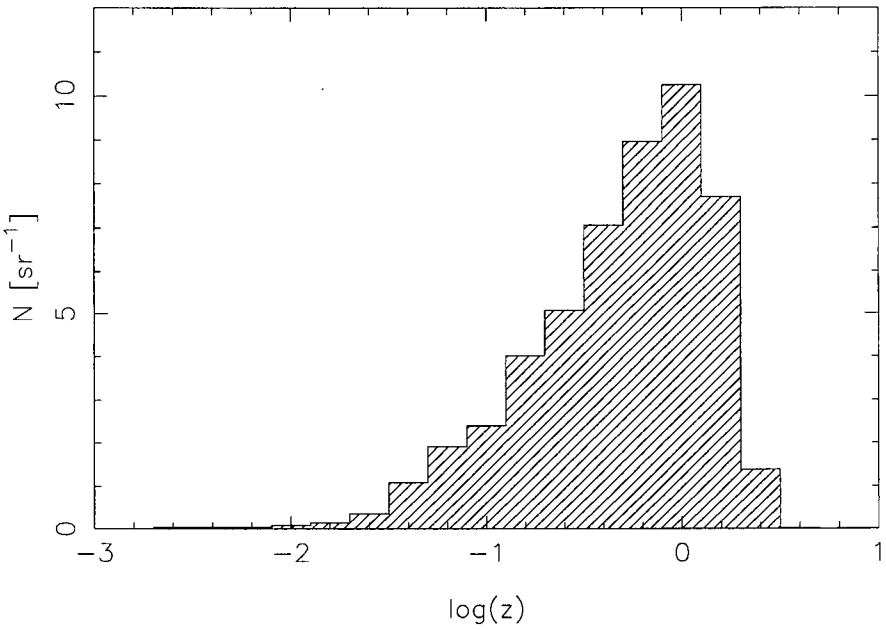

Figure 3.1: Modeled redshift distribution for the entire primary sample. The distribution is constructed by adding the number of sources n_{ij} of each $(\Delta P_i, \Delta z_j)$ bins with $S_{ij} \geq 1.3$Jy corresponding to each redshift bins.

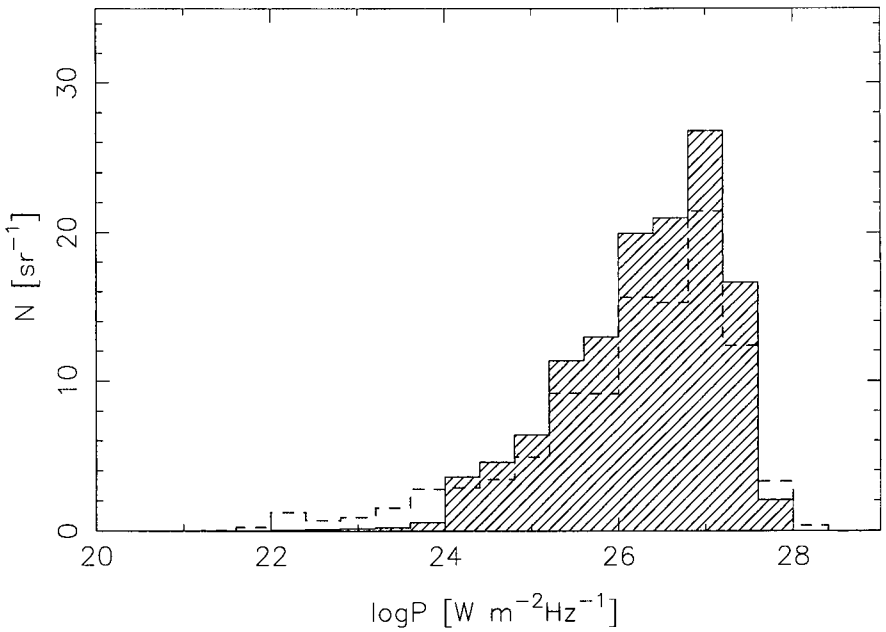

Figure 3.2: Modeled (black) and data (dashed blue) luminosity distribution ($q_0 = 0.5$) for the entire primary sample. The modeled distribution is constructed by adding the number of sources n_{ij} of each $(\Delta P_i, \Delta z_j)$ bins with $S_{ij} \geq 1.3$Jy corresponding to each luminosity bins. As discussed in section 3.1.3, both distributions being similar shows that the modeling was done successfully.

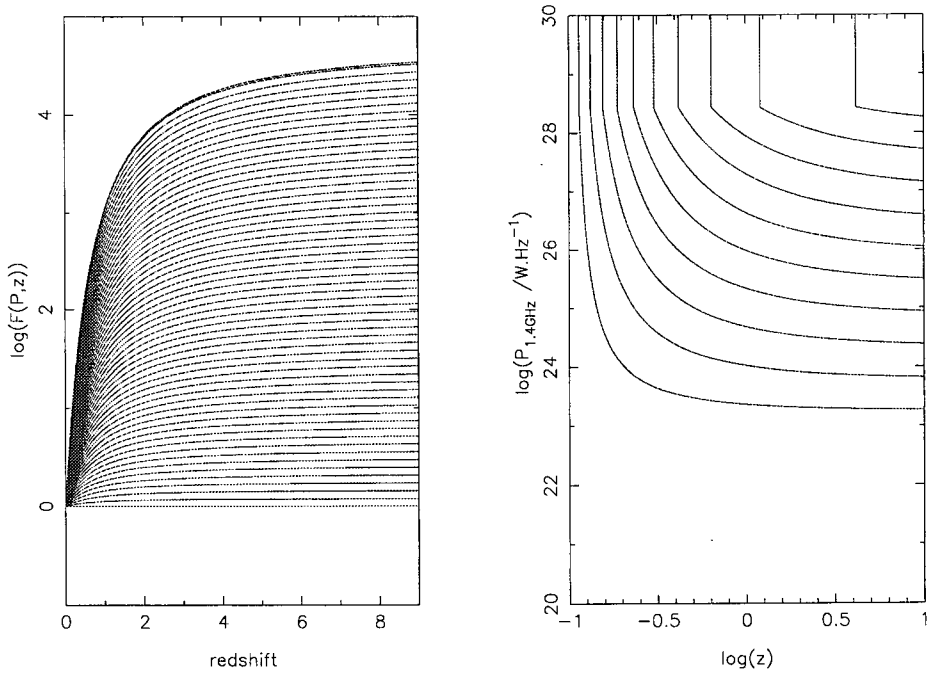

Figure 3.3: Evolution function for model 1 for the entire primary sample. The left panel represents contours of the evolution function as a function of redshift for different luminosities. The right panel represents contours of the evolution function in the (P,z) plane.

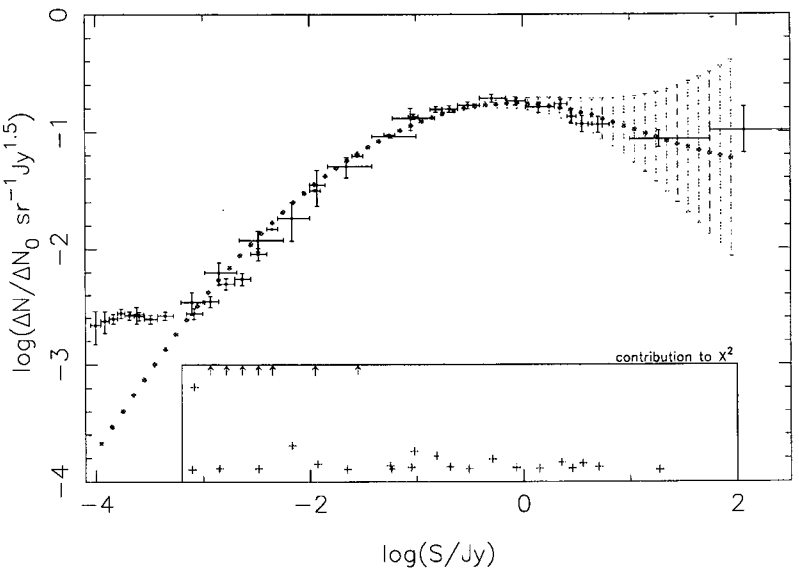

Figure 3.4: Modeled (pink filled circles) and data (black filled squares) relative differential source count for model 1 for the entire primary sample. The errors bars correspond to $\sqrt{N_{mod}}$. The bottom section shows the contribution to $\chi^2$of each point of the model, where the arrows show a contribution to the reduced χ^2greater than 3. As seen in this section, only points for $-3 \geq logS \geq 1.2$ were used to compute the value of χ^2.

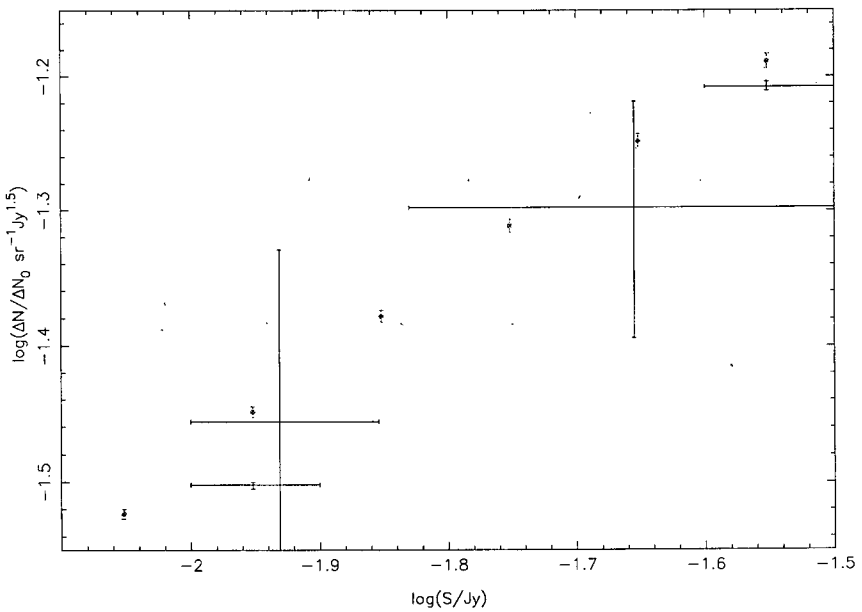

Figure 3.5: Close-up on the source count fitting plot for model 1. The points located at $logS = -2.35$, $logS = -1.95$ and $logS = -1.55$ correspond to source count data computed from FIRST, while the other points are source count data from previous surveys.It is obvious from this figure that the contributions to $\chi^2$of the model points associated with the FIRST source count points will be large, indicating that the model is not suitable anymore to describe the data.

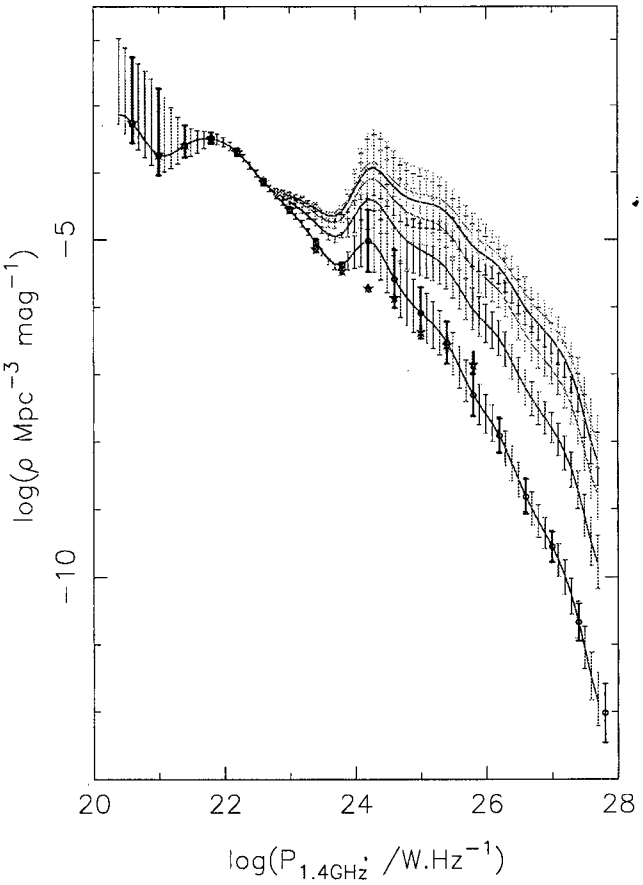

Figure 3.6: Modeled luminosity function versus luminosity for model 1, normalized to 4π sr. The pink stars represent the LLF from Sadler et al. (2002) and the black circles the final modeled LLF. The purple, red, green, blue and turquoise area correspond to the LLF (z=0.00), log(z+1)=0.2 (z=0.58), log(z+1)=0.4 (z=1.51), log(z+1)=0.6 (z=2.98) and log(z+1)=0.8 (z=5.31) respectively. Values of the luminosity function at the different redshifts were computed using $\rho(P,z) = \rho_0(P) \times F(P,z)$. The errors bars correspond to $\sqrt{N_{mod}}$.

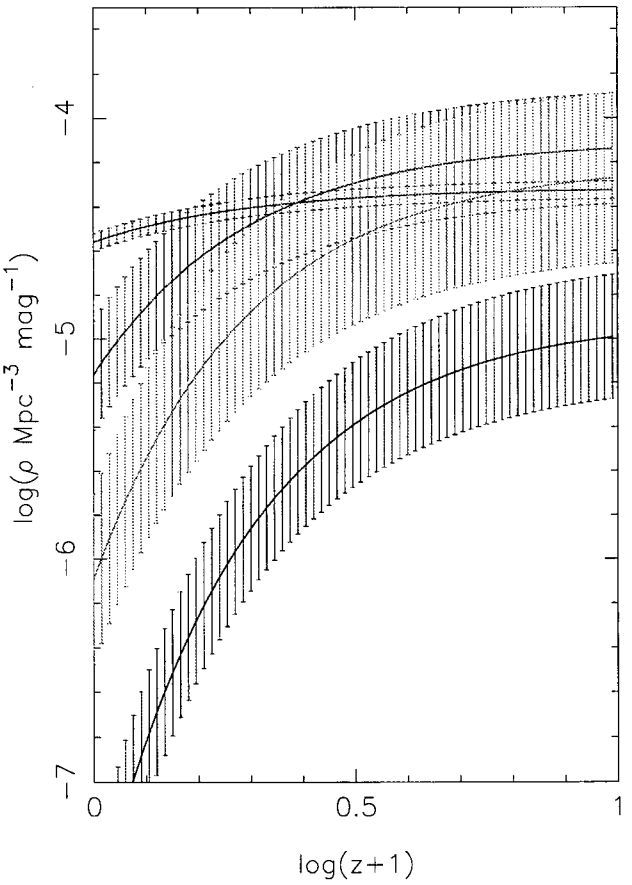

Figure 3.7: Modeled luminosity function versus redshift for model 1 for the entire primary sample. The purple, red, green and blue area correspond to $logP = 23$, $logP = 24$, $logP = 25$ and $logP = 26$ respectively. Values of the luminosity function at the different luminosities were computed using $\rho(P, z) = \rho_0(P) \times F(P, z)$. The errors bars correspond to $\sqrt{N_{mod}}$

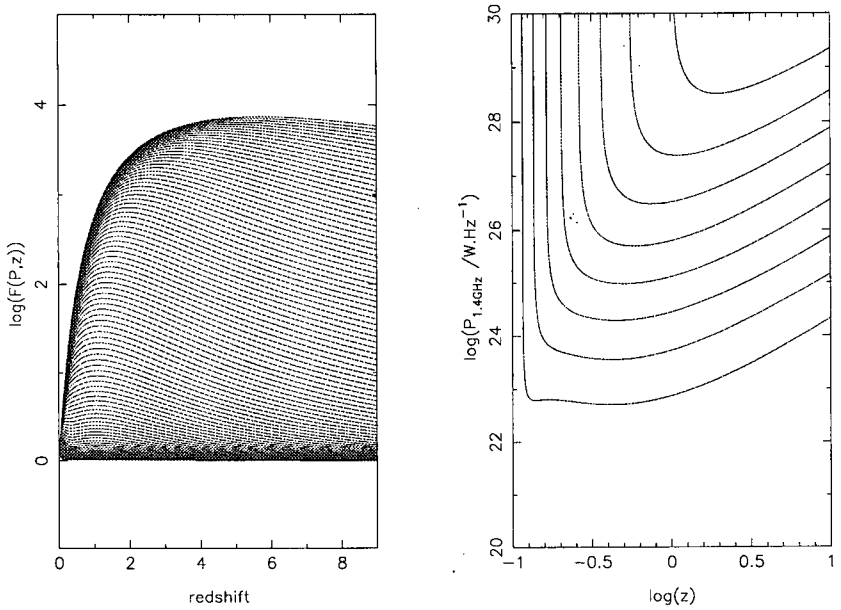

Figure 3.8: Evolution function for model 3 for the entire primary sample. The left panel represents contours of the evolution function as a function of redshift for different luminosities. The right panel represents contours of the evolution function in the (P,z) plane.

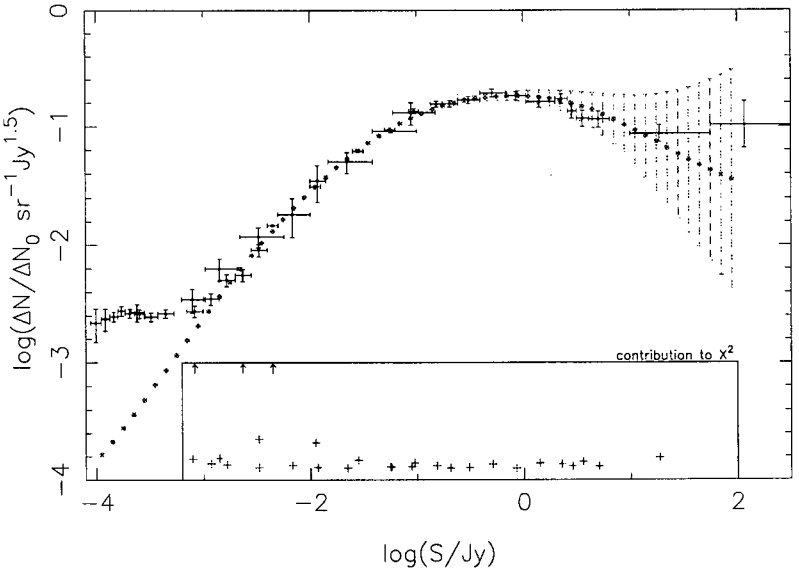

Figure 3.9: Modeled (pink filled circles) and data (black filled squares) relative differential source count for model 3 for the entire primary sample. The errors bars correspond to $\sqrt{N_{mod}}$. The bottom section shows the contribution to $\chi^2$of each point of the model, where the arrows show a contribution to the reduced χ^2greater than 3. As seen in this section, only points for $-3 \geq logS \geq 1.2$ were used to compute the value of χ^2.

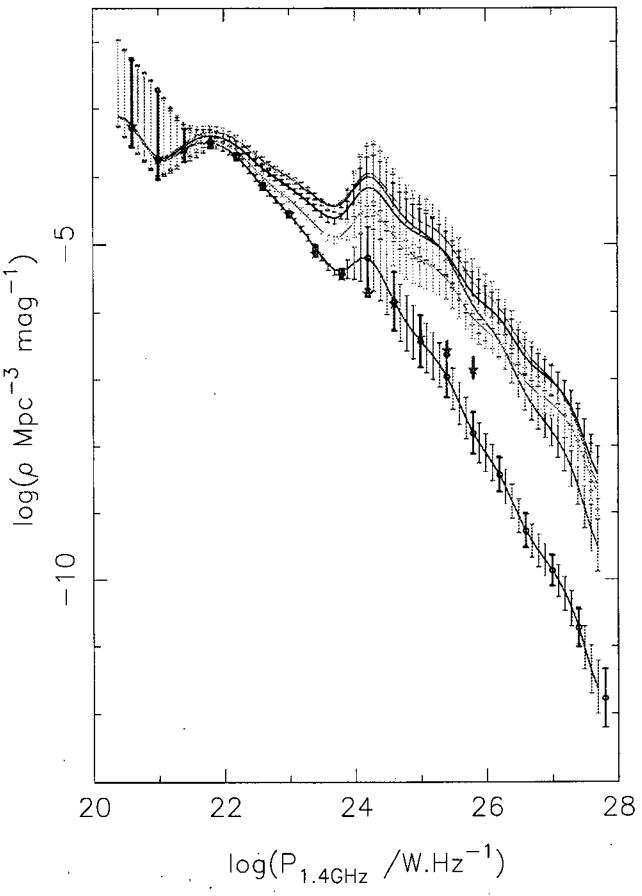

Figure 3.10: Modeled luminosity function versus luminosity for model 3, normalized to 4π sr. The pink stars represent the LLF from Sadler et al. (2002) and the black circles the final modeled LLF. The purple, red, green, blue and turquoise area correspond to the LLF (z=0.00), log(z+1)=0.2 (z=0.58), log(z+1)=0.4 (z=1.51), log(z+1)=0.6 (z=2.98) and log(z+1)=0.8 (z=5.31) respectively. Values of the luminosity function at the different redshifts were computed using $\rho(P,z) = \rho_0(P) \times F(P,z)$. The errors bars correspond to $\sqrt{N_{mod}}$.

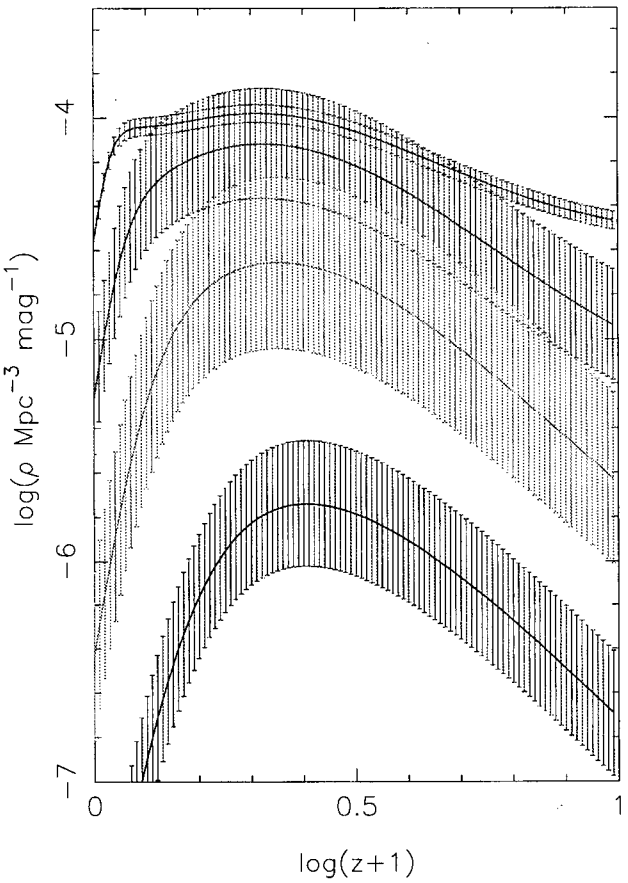

Figure 3.11: Modeled luminosity function versus redshift for model 3 for the entire primary sample. The purple, red, green and blue area correspond to $logP = 23$, $logP = 24$, $logP = 25$ and $logP = 26$ respectively. Values of the luminosity function at the different luminosities were computed using $\rho(P, z) = \rho_0(P) \times F(P, z)$. The errors bars correspond to $\sqrt{N_{mod}}$.

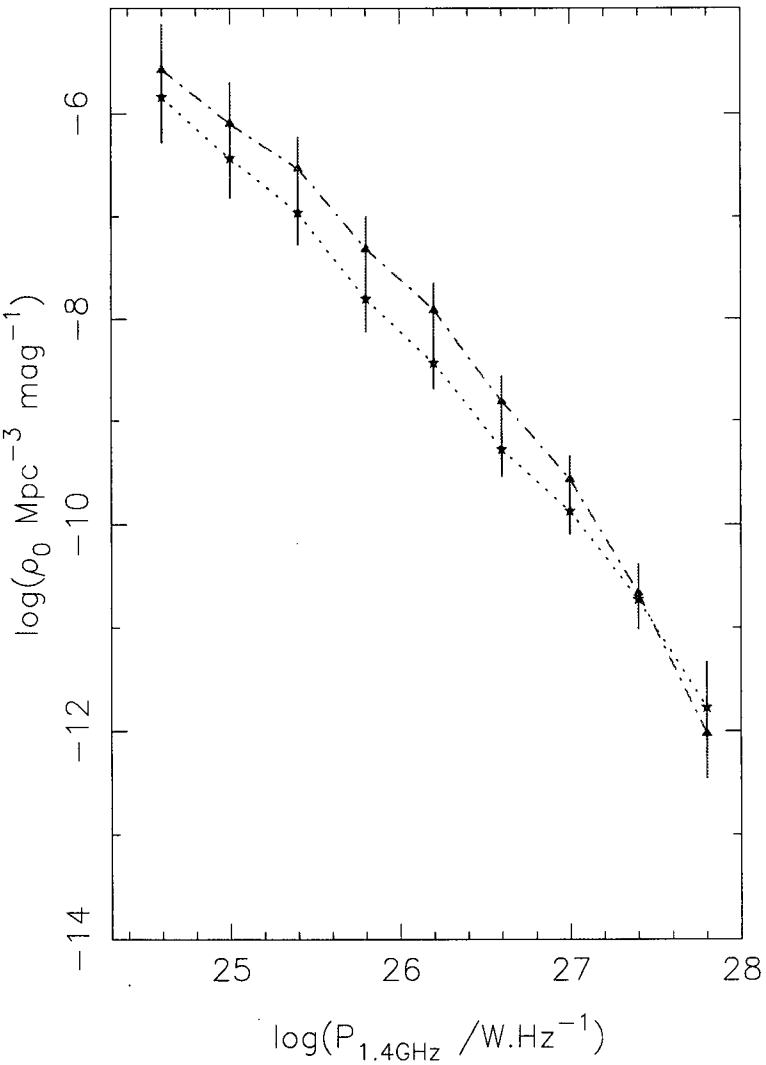

Figure 3.12: Comparison of LLF for the different models for the entire primary sample. The red dashed-dotted line and filled triangle correspond to the LLF for model 1, and the blue dotted line and filled stars correspond to the LLF for model 3. The errors bars correspond to $\sqrt{N_{mod}}$. This illustrate very well the dependence of the local luminosity function on the evolution function. The comparison is done for $logP \geq 24.6$ as the local luminosity functions at lower powers are similar (no evolution).

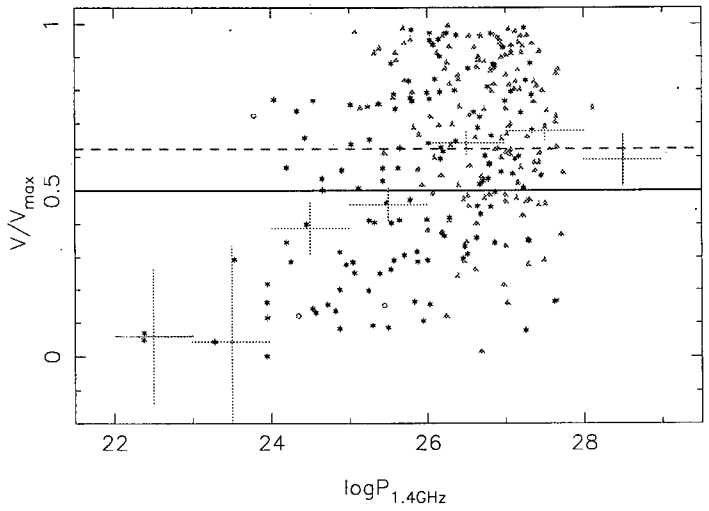

Figure 3.13: V/V_{max} with respect to radio luminosity for the FIRST sample. The black line correspond to $< V/V_{max} >= 0.5$, the red dash line to $< V/V_{max} >= 0.6113$ of the FIRST sample (implying an increasing number of sources with epoch), the blue stars to the value of V/V_{max} for each extended sources, the orange filled triangles to the value of V/V_{max} for each QSOs, the grey open circles to the value of V/V_{max} for other sources. The green crosses to $< V/V_{max} >$ for bins of $\Delta logP = 1.0$. The value of $\langle V/V_{max} \rangle$ is a little be low though, probably due to the error induced by the fact that the redshifts estimated using the Hubble diagram are photometric redshifts and not the actual redshifts of the sources.

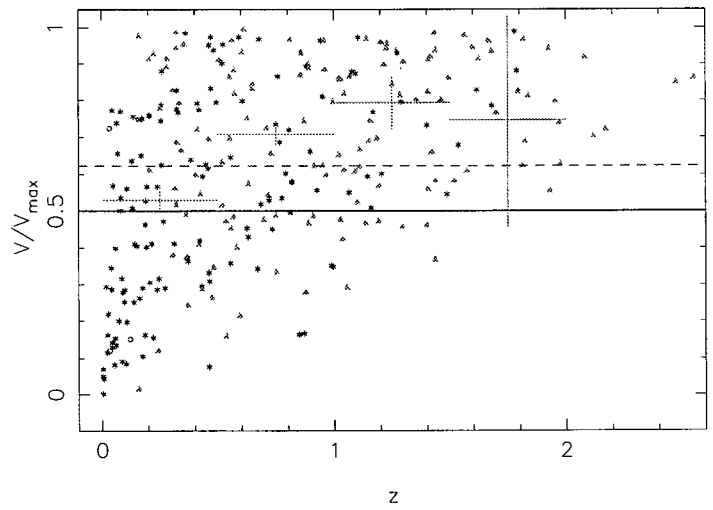

Figure 3.14: V/V_{max} with respect to redshift for the FIRST sample. Same legend as the previous figure, except for the green crosses now corresponding to $< V/V_{max} >$ for bins of $\Delta z = 0.5$.

3.3 Modeling for extended sources only

The data luminosity distribution and source count computed for extended sources only are used here.

The modeled redshift distribution as well as the comparison of the modeled and data luminosity distribution for the entire primary sample are shown in figure 3.15 and 3.16. As discussed in section 3.1.3, both luminosity distributions being similar shows that the modeling was done successfully.

For each model, plots of the best fit of the relative differential source count (figures 3.17, 3.18 and 3.20) are shown. In addition, for model 3 only (the best fitting model), contour plots of the evolution function as a function of redshift for different luminosities and contour plots of the evolution function in the (P,z) plane (figure 3.19), as well as the luminosity function with respect to luminosity (figure 3.21) and redshift (figure 3.22) are shown.

Table 3.2: Results from modeling of the luminosity function for extended sources only

model #	Best Fit Parameters	χ^2_{red} ($\nu = 28$)
1	$M_{max} = 8.8873$ $P_1 = 24.5317$ $P_2 = 26.2872$	110.77
2	$M_{max} = 9.4754$ $P_1 = 23.1103$ $P_2 = 26.6565$ $z_c = 1.3212$	271.06
3	$M = 9.6714$ $a = 2.4833$ $b = 26.2054$ $n = 0.9679$	101.67

As in §3.2, the values of χ^2_{red} are very high, implying that the models used are not suitable to describe the data.

From the comparison of the χ^2 values, model 3 is once again the best fitting model, followed by model 1. Model 2 has the worst fit, and the redshift cutoff value of $z_c = 1.32$ seems not realistic.

A comparison plot of the LLF is given in figure 3.23. Again, this illustrate the dependence of the local luminosity function on the evolution function and the comparison was done only for $logP \geq 24.8$ as the local luminosity functions at lower powers are similar (no evolution).

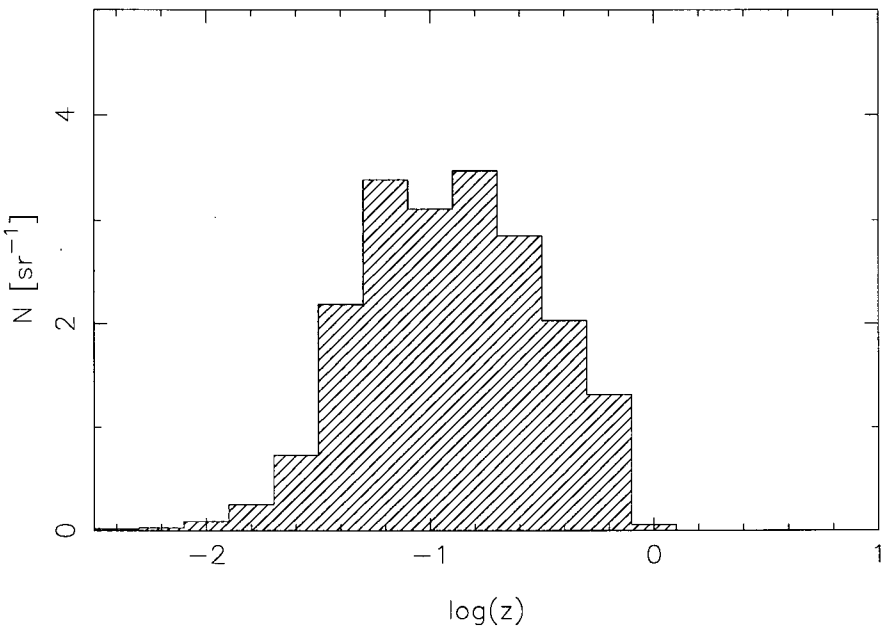

Figure 3.15: Modeled redshift distribution for extended sources only. The distribution is constructed by adding the number of sources n_{ij} of each $(\Delta P_i, \Delta z_j)$ bins with $S_{ij} \geq 1.3$Jy corresponding to each redshift bins.

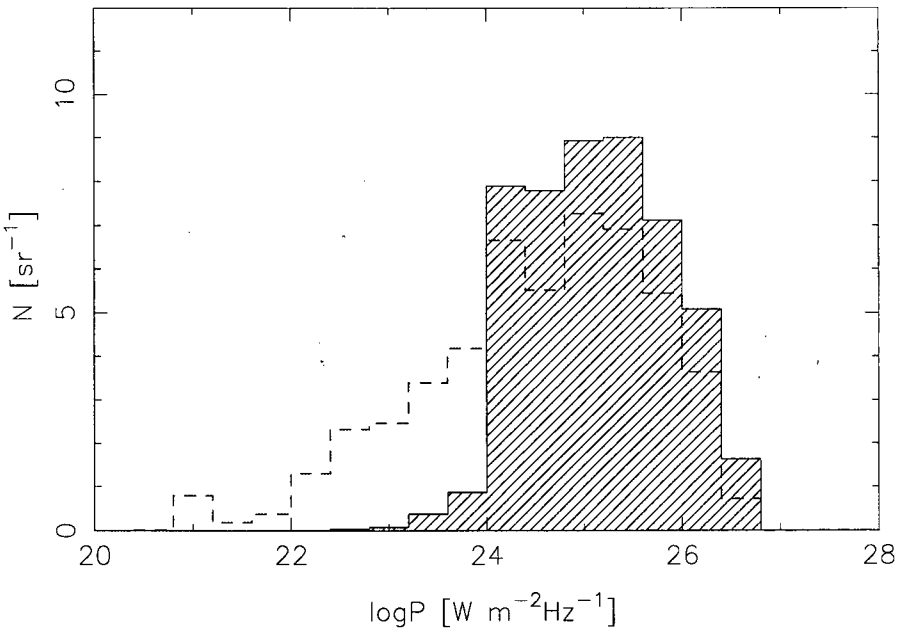

Figure 3.16: Modeled (black) and data (dashed blue) luminosity distribution for extended sources only. The modeled distribution is constructed by adding the number of sources n_{ij} of each $(\Delta P_i, \Delta z_j)$ bins with $S_{ij} \geq 1.3$Jy corresponding to each luminosity bins. As discussed in section 3.1.3, both distributions being similar shows that the modeling was done successfully.

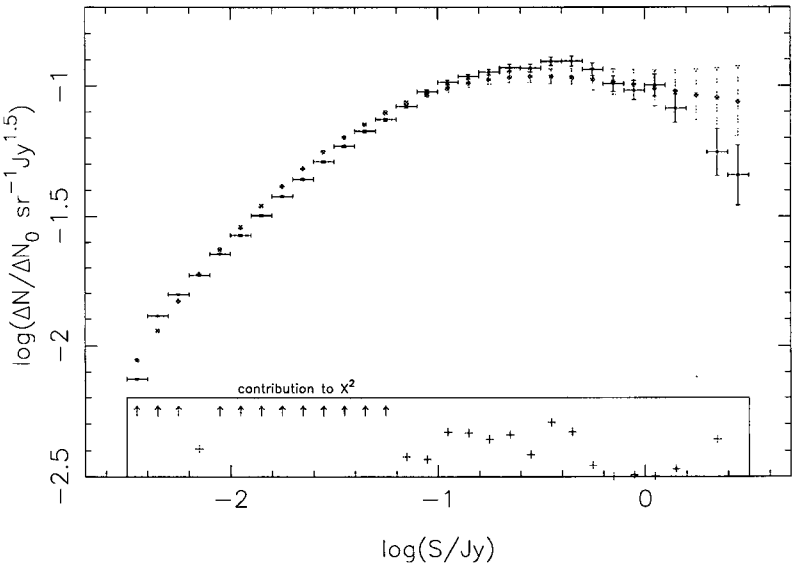

Figure 3.17: Modeled (pink filled circles) and data (black filled squares) relative differential source count for model 1 for extended sources only.The errors bars correspond to $\sqrt{N_{mod}}$. The bottom section shows the contribution to $\chi^2$of each point of the model, where the arrows show a contribution to the reduced χ^2greater than 3.

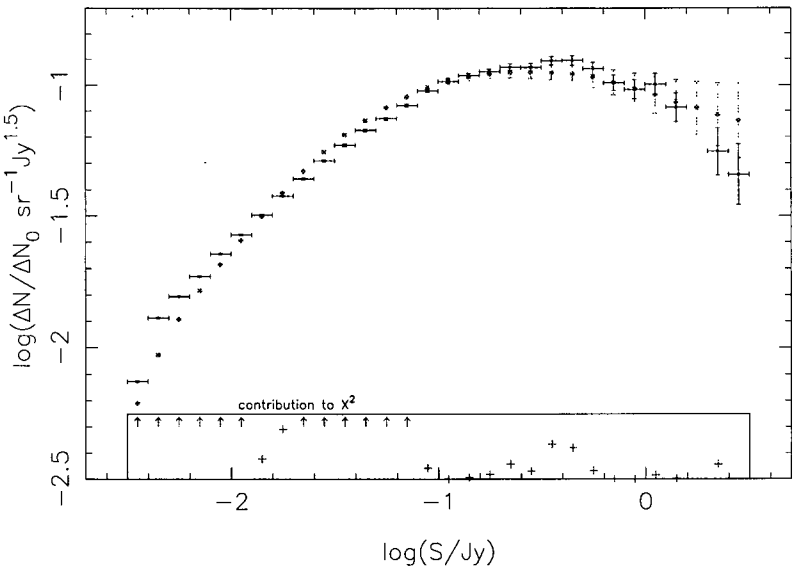

Figure 3.18: Modeled (pink filled circles) and data (black filled squares) relative differential source count for model 2 for extended sources only.The errors bars correspond to $\sqrt{N_{mod}}$. The bottom section shows the contribution to $\chi^2$of each point of the model, where the arrows show a contribution to the reduced χ^2greater than 3.

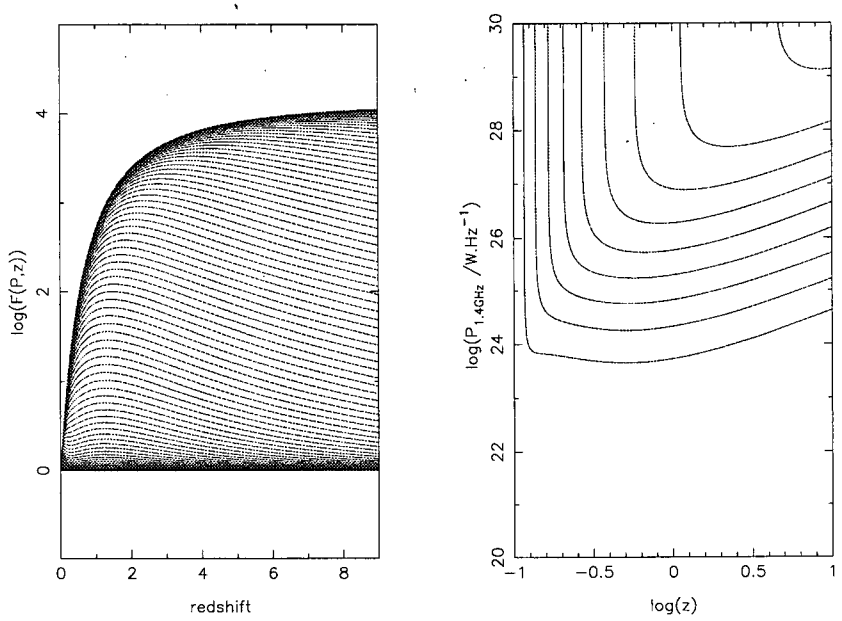

Figure 3.19: Evolution function for model 3 for extended sources only. The left panel represents contours of the evolution function as a function of redshift for different luminosities. The right panel represents contours of the evolution function in the (P,z) plane.

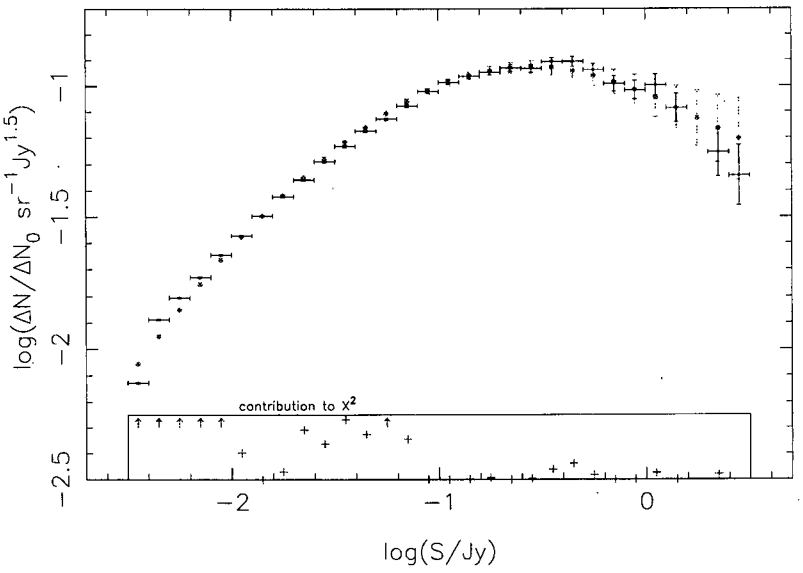

Figure 3.20: Modeled (pink filled circles) and data (black filled squares) relative differential source count for model 3 for extended sources only.The errors bars correspond to $\sqrt{N_{mod}}$. The bottom section shows the contribution to $\chi^2$of each point of the model, where the arrows show a contribution to the reduced χ^2greater than 3.

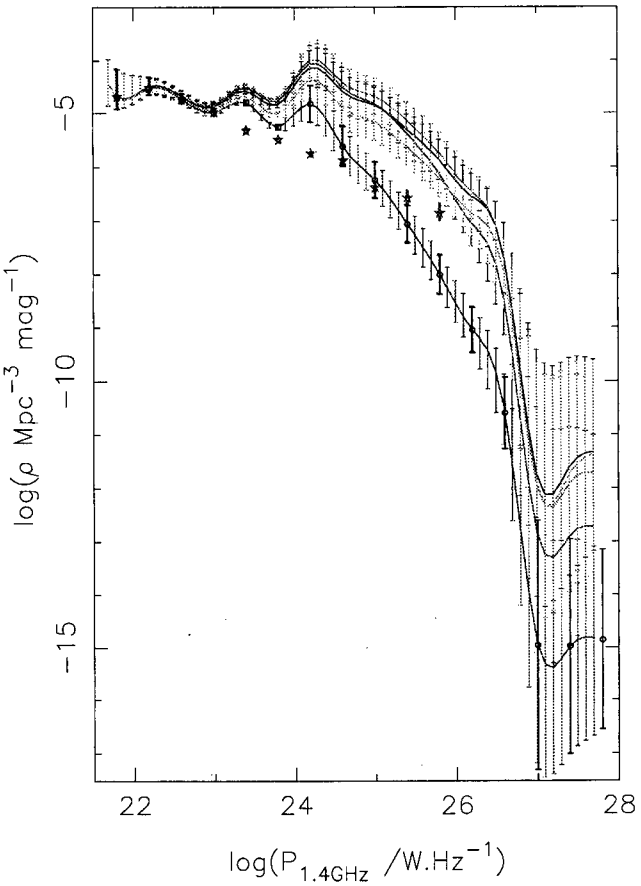

Figure 3.21: Modeled luminosity function versus luminosity for model 3, normalized to 4π sr. The pink stars represent the LLF from Sadler et al. (2002) and the black circles the final modeled LLF. The purple, red, green, blue and turquoise area correspond to the LLF (z=0.00), log(z+1)=0.2 (z=0.58), log(z+1)=0.4 (z=1.51), log(z+1)=0.6 (z=2.98) and log(z+1)=0.8 (z=5.31) respectively. Values of the luminosity function at the different redshifts were computed using $\rho(P,z) = \rho_0(P) \times F(P,z)$. The errors bars correspond to $\sqrt{N_{mod}}$.

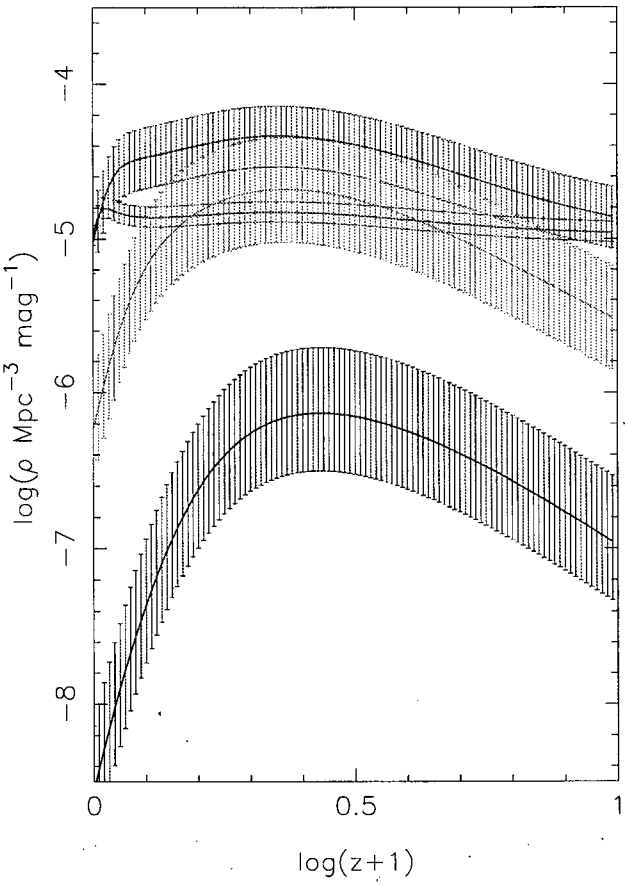

Figure 3.22: Modeled luminosity function versus redshift for model 3 for extended sources only. The purple, red, green and blue area correspond to $logP = 23$, $logP = 24$, $logP = 25$ and $logP = 26$ respectively. Values of the luminosity function at the different luminosities were computed using $\rho(P, z) = \rho_0(P) \times F(P, z)$. The errors bars correspond to $\sqrt{N_{mod}}$.

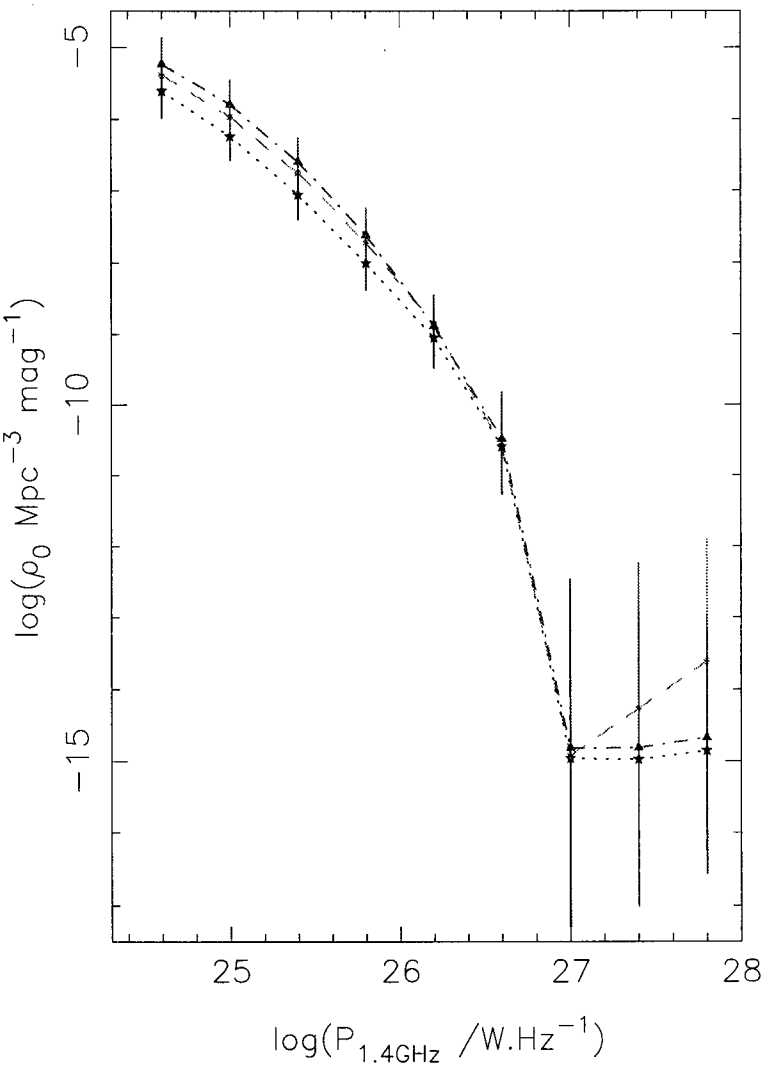

Figure 3.23: Comparison of LLF for the different models for extended sources only. The red dotted-dashed line and filled triangle correspond to the LLF for model 1, the green dashed line and filled squares correspond to model 2 and the blue dotted line and filled stars correspond to the LLF for model 3. The errors bars correspond to $\sqrt{N_{mod}}$. Again, this illustrate the dependence of the local luminosity function on the evolution function and the comparison was done only for $logP \geq 24.8$ as the local luminosity functions at lower powers are similar (no evolution).

Chapter 4

Conclusion

Summary

By combining both FIRST and NVSS data, a complete and unbiased sample of radio sources at $S_{1.4GHz} = 1.3$Jy including morphological identification was constructed. Redshift information was found for 94% of the sources in the sample, from databased such as SIMBAD or SDSS.

Models described as "successful" by Wall, Pearson & Longair (1980) were applied to this entire primary sample as well as to the sub-sample of extended sources only. Comparing the values of χ^2showed that the exponential law evolution, with $P_t = alog(z) + b$ (model 3) was the "best" model to describe both data from the entire sample and from the sub-sample of extended sources. However, in both cases, values of $\chi^2{}_{red}$ are very high, implying that none of the models used are suitable anymore to describe the new, more accurate data available. Indeed, as stated in §3.2, when trying to fit the modeled and data source counts, any point of the model not coinciding exactly with one of the recent source count data point will be many sigmas away from that point and its contribution to χ^2 will therefore be very high. The conclusion that the models are too simple to describe the new data available is emphasized even more in the case of the sub-sample of extended sources only (the best fitting model has $\chi^2{}_{red}$=101.7), for which only FIRST data were used to compute the data source count.

Overall, this pilot project was successful in showing that it was possible to model the luminosity function for a given type of sources using the primary sample selected with FIRST and NVSS. This represents a major new way in which to use the complementary nature of these surveys. However, it also showed that the modeling will not be as easy as it was first thought, especially since it will be of primary importance to compute the source count specific to the studied population to apply the WPL modeling technique.

Future work

In the follow up of this project, it would be interesting to try a different type of modeling such as the Marshall likelihood models (Marshall et al., 1983), on our sub-sample of extended sources only. All the models of the lumnosity function should be applied to different samples at various flux limits (a total of 3 or 4 different samples would provide a good range of flux limits), to provide maximum available constraints to the evolving luminosity function.

Another advantage of multiple samples at different flux limits would be to have a large number of sources from the FIRST survey with their morphological information (especially if each sample is taken over a different region of the survey, making sure all the sources in each surveys are different). Combining those samples would allow to compute a much more accurate source count for extended sources only, and even to compute the source counts for FRI and FRII sources respectively.
Then, if it is possible to compute a source count for FRI and FRII populations separately, the radio luminosity functions should be modeled for both source types (using samples from the surveys at various flux limits). By comparing them (along with the evolution function associated with each models), the basis of the dual-population unified model (Jackson & Wall, 1999) could be tested.

Finally, the limits and ranges of beaming parameters are poorly established at present because the samples from which these parameters are measured are so seriously biased. This is not the case for the samples in this project. Therefore, in anticipation of the successful outcome for the last phase, we can look forward to a thorough redevelopment of the Jackson-Wall paradigm, to find much further detail about bulk beaming properties of powerful radio AGN.

Bibliography

Becker, R. H. et al., 1995, *Astrophysical Journal*, **450**:559

Benn, C.R. et al., 1982, *MNRAS*, **200**:747

Best, P. N. et al., 2005, *MNRAS*, **362**:9

Blandford, R. D. & Rees, M. J., 1974, *MNRAS*, **169**:395

Bridle, A. H. et al., 1972, *Nature*, **235**:123

Colless, M., 1999, *Phil. Trans. R. Soc. London A.*, **357**:105

Colless, M. et al., 2001, *MNRAS*, **328**:1039

Condon, J.J., Condon, M.A & Hazard, C., 1982, *Astronomical Journal*, **87**:5

Condon, J.J., 1989, *Astrophysical Journal*, **338**:13

Condon, J. J. et al., 1998, *Astronomical Journal*, **115**:1693

Doroshkevich, A. G. et al., 1970, *MNRAS*, **147**:139

Dunlop, J. S. & Peacock, J. A., 1990, *MNRAS*, **247**:19

Fanaroff, B. L. & Riley, J. M., 1974, *MNRAS*, **167**:31p

Fomalont, E. B. et al., 1974, *Astronomy and Astrophysics*, **36**:273

Fukugita, M., Shimasaku, K. & Ichikawa, T., 1995, *PASP*,**107**:945

Hopkins, A.M. et al., 2003, *Astronomical Journal*, **125**:465

Jackson, C. A. & Wall, J. V., 1999, *MNRAS*, **304**:160

Kellerman, K. I. & Wall, J. V., 1987, *Observational Cosmology, IAU symp 124 eds* Hewitt A.,Burbidge G. & Li Zhi fang (Reidel, Dordrecht)

Laing, R. A., Riley, J. M., & Longair, M. S., 1983, *MNRAS*, **204**:151

Longair, M. S., 1966, *MNRAS*, **133**:421

Machlaski, J., 1978, *Astronomy and Astrophysics*, **65**:157

Marshal, H. L., et al., 1983, *Astrophysical Journal*, **269**:35

Mitchell, K.J. & Condon, J.J., 1985, *Astronomical Journal*, **90**:10

Orr, M. J. W. & Browne, I. W. A., 1982, *MNRAS*, **200**:1067

Parma, P., et al., 1992, *Astrophysical Jets*, Poster Papers from the Space Telescope Science Institute Symposium, *eds* D. Burgarella, M. Livio and C. O'Dea, p.30

Peacock, J. A., 1985, *MNRAS*, **217**:601

Pence, W., 1976, *Astrophysical Journal*, **203**:39

Prandoni, I. et al., 2001, *Astronomy and Astrophysics*, **365**:392

Rees, M. J., 1967, *MNRAS*, **135**:345

Rees, M. J., 1971, *Nature*, **229**:47

Ryle, M. & Clark, R. W., 1961, *MNRAS*, **122**:349

Sadler, E.M. et al., 1999, *PASA*, **329**:247

Sadler, E.M. et al., 2002, *MNRAS*, **329**:227

Sandage, A., 1972, *Astrophysical Journal*, **178**:1

Saunders W. et al, 1990, *MNRAS*, **242**:318

Seyfert, C., 1943, *Astrophysical Journal*, **97**:28

Schmidt, M., 1968, *Astrophysical Journal*, **151**:393

Scheuer, P. A. G., 1974, *MNRAS*, **166**:513

Sneller, I. A. G. & Best, P. N., 2001, *MNRAS*, **328**:897

Urry, C.M. & Padovani, P., 1995, *PASP*, **107**:803

Wall, J.V., 1983, *The Origine and Evolution of Galaxies*, *eds* Jones B. J. T. & Jones J. E. (Reidel, Dordrecht)

Wall, J.V., & Jackson, C. A., 1997, *MNRAS*, **290**:17

Wall, J.V., Pearson, T.J. & Longair, M.S., 1980, *MNRAS*, **193**:683

White, R. L. et al., 1997, *Astrophysical Journal*, **475**:479

York, D. G. et al., 2000, *Astronomical Journal*, **120**:1579

Appendix A

Data tables

A.1 Primary sample

Columns 1 and 2 correspond to the right ascension and declination of the radio identification; column 3 gives the name of the source; columns 4 and 5 correspond to the flux density from FIRST and NVSS respectively, in mJy; column 6 and 7 correspond to the B and V magnitudes; column 8 describes the source morphology (Co for compact, I for FRI, II for FRII, U for other types); column 9 corresponds to redshift; column 10 gives information on the SDSS identification (c for confirmed identification, u for possible but not confirmed, n for none) as well as information on the magnitudes and redshift estimation (B and V when the magnitudes were estimated from SDSS, H when the redshift was estimated from the Hubble diagram).

Table A.1: Primary sample

RA	DEC	Name	S_{FIRST} (mJy)	S_{NVSS}	B	V	morph.	z	
00 06 22.611	-00 04 24.48	3C 002	3879.24	3897.6	20.14	19.35	Co	1.0370	c
00 13 10.910	+00 51 42.40	3C 005	1600.68	1620.1	22.37	20.73	II	0.6060	u A
00 22 25.437	+00 14 56.08	PKS 0019-00	2938.88	3009.2	21.10	19.57	Co	0.3050	c V
00 37 04.060	-01 09 09.40	3C 015	3703.23	4067.1	15.34	17.33	I	0.0730	c V
00 38 20.410	-02 07 40.40	3C 017	6015.11	6187.8	18.02	0.00	I	0.2196	n
00 57 34.150	-01 22 58.40	3C 029	2087.33	5365.4	14.07	0.00	II	0.0448	n
00 59 05.511	+00 06 51.70	PKS 0056-00	2415.95	2508.8	17.53	17.33	Co	0.7170	c
01 25 28.853	-00 05 56.20	PKS 0122-00	1524.09	1540.2	16.50	16.70	Co	1.0700	c
01 26 4.670	-01 24 1.90	NGC 547 (3C 40)	151.38	2891.1	14.38	13.34	I	0.0185	n
02 20 54.052	-01 56 55.16	3C 063	3123.21	3419.2	18.50	0.00	I	0.1750	n
02 42 40.720	-00 00 47.70	M77	4261.56	4848.1	8.91	9.77	I	0.0038	c V
06 55 14.780	+54 09 00.00	3C 171	3636.91	3680.0	18.89	18.90	II	0.2384	n
07 02 53.639	+44 31 11.92	4C 44.15	2433.08	2397.4	0.00	0.00	Co	0.0000	n
07 06 48.083	+46 47 56.39	B3 0703+468	1589.99	1584.9	23.10	0.00	Co	1.4941	nH
07 13 38.169	+43 49 17.06	B0710+439	2032.11	2011.4	20.70	0.00	Co	0.5180	n
07 14 24.813	+35 34 39.70	B0711+35	1533.45	1467.1	18.20	17.00	Co	1.6260	n
07 16 41.090	+53 23 10.30	4C 53.16	1298.23	1501.4	14.55	14.00	II	0.0643	n
07 35 55.549	+33 07 9.44	4C 33.21	2423.09	2473.1	21.00	20.90	Co	0.5187	cHV
07 38 7.379	+17 42 19.60	J0738+1742	1101.95	2257.7	15.32	14.85	Co	0.4240	c
07 41 10.698	+31 12 0.31	J0741+3111	2071.27	2284.3	16.88	17.00	Co	0.6313	c B
07 45 42.131	+31 42 52.60	4C 31.30	1163.63	1357.8	15.92	16.00	II	0.4620	c B
07 50 52.057	+12 31 4.64	PKS 0748+126	1543.06	1452.8	18.00	17.80	Co	0.8890	n
07 58 28.601	+37 47 13.80	NGC 2484	545.97	2717.9	14.15	14.90	I	0.0410	cH
07 59 47.259	+37 38 50.20	4C 37.21	1602.00	1691.2	16.40	15.20	II	0.0681	nH
08 01 33.507	+14 14 42.66	3C 190	2597.74	2734.1	21.20	20.00	Co	1.1950	n
08 01 35.320	+50 09 43.00	TXS 0757+503	1513.94	1471.7	22.41	21.17	II	0.8811	uHA

08 04 47.970	+10 15 22.91	3C 191	1870.27	1849.3	18.65	18.40	Co	1.9560	n
08 05 31.310	+24 10 21.30	3C 192	1035.39	5330.6	15.46	0.00	II	0.0600	n
08 10 3.6701	+42 28 4.00	3C 194	2160.43	2056.6	24.00	23.47	Co	1.1840	u V
08 12 59.480	+32 43 5.60	4C 32.24	1230.17	1522.5	23.00	0.00	II	0.4700	n
08 13 36.037	+48 13 1.77	3C 196	14693.27	15010.0	18.36	17.79	II	0.8710	c
08 14 43.589	+12 58 10.00	4C 13.37	1370.77	1603.3	20.00	18.00	II	0.3226	nH
08 19 47.550	+52 32 29.50	4C 52.18	2049.12	2104.2	19.95	18.00	II	0.1890	u B
08 21 33.771	+47 02 35.70	3C 197.1	1711.27	1787.1	16.90	16.50	I	0.1300	c
08 21 44.034	+17 48 20.30	PKS 0818+17	1960.03	1875.1	19.00	0.00	Co	0.2044	nH
08 22 31.400	+05 57 24.00	3C 198	77.39	1965.5	16.78	0.00	I	0.0813	n
08 23 24.755	+22 23 3.27	PKS 0820+22	2163.90	2272.4	19.50	19.67	Co	0.9510	c V
08 24 47.239	+55 52 42.75	4C 56.16A	1404.55	1449.4	18.69	18.00	Co	1.4170	c B
08 24 55.475	+39 16 41.76	4C 39.23A	1456.09	1480.8	18.58	18.50	Co	1.2156	c B
08 25 50.370	+03 09 24.80	B0823+033	1178.73	1400.1	18.80	17.60	Co	0.5060	c B
08 27 25.398	+29 18 44.80	3C 200	1966.59	2043.1	20.00	19.85	II	0.4580	c V
08 31 10.032	+37 42 9.61	4C 37.24	2148.17	2259.6	18.53	18.11	Co	0.9140	c
08 33 18.801	+51 03 7.80	4C 51.25	1215.36	1313.5	20.00	0.00	II	0.4700	n
08 34 48.216	+17 00 42.81	3C 202	1642.16	1882.8	19.50	0.00	II	0.2562	nH
08 34 54.914	+55 34 20.96	4C 55.16	8254.60	8283.1	17.50	17.41	Co	0.2420	c V
08 39 6.500	+57 54 13.40	3C 205	2430.10	2257.7	17.62	17.62	II	1.5360	u
08 40 47.712	+13 12 23.64	3C 207	2777.47	2613.0	18.15	18.15	II	0.6840	n
08 43 31.653	+42 15 29.49	B3 0840+424A	1458.79	1409.7	23.54	22.00	Co	1.4390	cHA
08 47 53.831	+53 52 36.80	S4 0844+54	1114.29	1542.3	15.00	13.91	I	0.0453	c V
08 53 9.008	+13 52 55.83	3C 208	2465.40	2364.3	18.60	17.40	Co	1.1100	n
08 53 28.286	-03 41 6.77	PKS 0850-03	1445.69	1354.0	19.20	0.00	Co	0.2236	nH
08 54 39.387	+14 05 52.23	3C 208.1	2198.42	2163.8	20.85	20.00	Co	1.0200	n
08 54 48.871	+20 06 30.70	J0854+2006	1182.12	1511.8	14.39	14.00	Co	0.3060	n
08 57 40.638	+34 04 6.40	3C 211	1650.11	1798.4	0.00	0.00	II	0.7500	n
08 58 10.071	+27 50 50.80	3C 210	1805.28	1807.8	22.00	23.22	II	1.1690	c V

08 58 41.539	+14 09 43.24	3C 212	2482.35	2370.8	20.26	19.06	Co	1.0430	n B
09 01 5.321	+29 01 46.46	3C 213.1	1675.77	2003.4	19.00	20.00	I	0.1940	c V
09 03 3.979	+46 51 4.51	4C 47.29	1724.45	1754.9	18.90	18.70	Co	1.4620	c
09 06 31.879	+16 46 13.00	3C 215	1456.80	1586.2	18.48	18.27	II	0.4115	n
09 07 34.920	+41 34 53.80	4C 41.19	1245.85	1612.6	0.00	0.00	II	0.0000	n
09 08 50.561	+37 48 20.20	3C 217	2138.72	2086.4	22.00	21.72	II	0.8980	u V
09 09 33.497	+42 53 46.54	3C 216	4009.50	4233.8	18.97	18.48	II	0.6702	c
09 12 3.999	+16 18 29.70	4C 16.27	1370.34	1374.6	19.70	18.50	Co	0.2808	nH
09 14 4.831	+17 15 52.40	4C 17.48	1383.73	1527.3	20.00	0.00	I	0.3226	nH
09 21 8.650	+45 38 57.40	3C 219	3734.27	8101.6	17.22	17.29	II	0.1744	c V
09 22 49.930	+53 02 21.20	4C 53.18	1560.73	1597.8	0.00	0.00	Co	0.0000	n
09 27 3.024	+39 02 20.72	4C 39.25	2958.51	2884.6	17.92	17.86	Co	0.6980	c
09 30 33.450	+36 01 23.60	3C 220.2	1851.78	1875.1	19.00	18.20	Co	1.1570	c
09 39 50.199	+35 55 53.10	3C 223	1326.33	3719.0	17.10	17.10	II	0.1368	n
09 41 25.700	+39 42 18.00	3C 223.1	1409.37	1976.8	16.36	16.40	II	0.1073	n
09 42 8.441	+13 51 53.66	3CR 225A	1357.48	1338.5	22.00	0.00	Co	1.5650	n
09 42 15.365	+13 45 50.64	3C 225	3420.63	3336.4	19.00	20.00	Co	0.5800	n
09 43 12.739	+02 43 27.50	SDSS	1299.66	1331.5	0.00	22.99	I	0.5920	c B
09 44 16.401	+09 46 19.20	3C 226	2324.27	2393.7	19.50	0.00	II	0.8178	n
09 47 47.270	+07 25 13.81	3C 227	3117.11	7617.0	17.53	16.33	II	0.0865	n B
09 48 55.357	+40 39 44.67	4C 40.24	1537.07	1599.5	18.13	17.50	Co	1.2520	c B
09 50 10.566	+14 19 40.30	3C 228	3387.33	3711.6	21.00	0.00	II	0.5524	n
09 51 58.830	-00 01 26.80	3C 230	3263.32	3152.1	0.00	0.00	I	1.4870	n
09 52 0.519	+24 22 29.70	3C 229	1308.40	1788.6	18.50	0.00	II	0.1696	nH
09 52 6.090	+28 28 32.35	4C 28.24	1364.17	1362.7	23.13	21.06	Co	1.2035	cHA
09 57 38.155	+55 22 57.89	4C 55.17	3056.17	3079.2	18.90	17.70	Co	0.9090	c B
10 01 46.200	+28 46 54.69	3C 234	3200.60	5597.0	17.27	17.10	II	0.1849	n
10 06 1.738	+34 54 10.43	3C 236	3399.40	3236.6	15.97	15.81	II	0.0989	c V
10 08 0.033	+07 30 16.50	3C 237	6400.71	6522.1	21.00	21.31	Co	0.8770	c V

10 11 0.346	+06 24 40.75	3C 238	2883.45	2964.2	22.50	0.00	Co	1.4050	n
10 11 45.460	+46 28 20.10	3C 239	1573.93	1557.2	22.50	22.53	II	1.7900	c V
10 17 14.176	+39 01 22.79	B3 1014+392	1416.71	1392.2	19.50	21.76	Co	0.2060	c V
10 21 54.533	+21 59 30.50	3C 241	1733.51	1686.2	23.50	0.00	II	1.6170	n
10 23 38.792	+59 04 49.48	S4 1020+59	1592.35	1609.3	19.00	20.27	Co	0.2044	cHV
10 33 33.870	+58 14 37.90	3C 244.1	3850.49	4187.9	19.00	19.00	II	0.4300	u
10 34 17.888	+50 13 29.73	4C 50.30	1580.31	1545.2	22.77	20.83	Co	1.0294	uHA
10 35 7.069	+56 28 46.83	B1031+567	1890.63	1801.9	20.20	21.25	Co	0.4597	c V
10 41 17.175	+06 10 16.57	PKS 1038+064	1329.00	1405.2	16.97	16.81	Co	1.2700	c
10 41 39.026	+02 42 31.99	PKS 1039+02	2926.41	2710.1	23.11	21.09	Co	0.5350	c A
10 42 44.586	+12 03 31.32	3C 245	3326.87	3305.7	17.75	17.29	Co	1.0286	c
10 51 48.799	+21 19 52.36	PKS 1049+215	1474.34	1474.3	19.70	18.50	Co	1.3000	n
10 52 26.095	+20 29 48.07	4C 20.23	1672.18	1727.5	21.62	0.00	Co	0.6277	nH
10 58 17.461	+19 52 11.40	PKS 1055+20	2281.88	2143.0	17.51	17.07	Co	1.1100	n
10 58 29.565	+01 33 58.45	PKS 1055+01	3353.64	3220.2	18.46	18.00	Co	0.8900	n
10 58 58.360	+43 01 21.66	3C 247	2869.58	2875.1	21.50	22.31	Co	0.7489	c V
11 02 4.329	-01 16 24.09	3C 249	2834.24	2799.6	0.00	0.00	II	0.3110	n
11 08 8.277	+14 35 35.54	PKS 1105+14	1335.14	1348.7	20.00	0.00	Co	0.3226	nH
11 09 46.071	+10 43 43.56	PKS 1107+10	1540.81	1481.3	0.00	0.00	Co	0.5500	n
11 11 31.558	+35 40 45.50	3C 252	1179.48	1336.3	22.00	0.00	II	1.1050	n
11 13 32.130	-02 12 55.20	3C 253	1239.15	1595.6	20.90	0.00	II	0.4942	nH
11 14 38.814	+40 37 19.13	3C 254	3037.20	3127.9	18.13	17.98	II	0.7340	c
11 16 34.699	+29 15 20.50	4C 29.41	1400.13	1927.9	15.02	14.90	II	0.0487	n
11 18 57.297	+12 34 41.86	PKS 1116+12	2322.07	2322.1	19.39	19.25	Co	2.1180	c
11 19 25.273	-03 02 51.12	3C 255	1720.32	1730.4	24.20	23.00	Co	1.3550	n
11 20 27.810	+14 20 54.99	PKS 1117+14	2438.53	2446.9	20.00	20.94	Co	0.3620	c V
11 20 43.012	+23 27 55.32	3C 256	1382.33	1362.0	21.50	0.00	Co	1.8190	n
11 23 9.062	+05 30 20.58	3C 257	1580.13	1721.1	24.32	24.29	Co	2.4740	c A
11 26 23.674	+33 45 26.64	4C 33.26	1316.07	1376.8	23.55	22.66	Co	1.2300	u A

11 31 38.917	+45 14 51.00	B3 1128+455	2025.82	2048.8	20.00	20.22	Co	0.4040	c V
11 34 38.490	+43 28 0.67	4C 43.22	1631.67	1567.1	20.00	21.65	Co	0.5724	c V
11 35 13.029	-00 21 18.75	PKS 1132-000	1321.23	1321.2	0.00	0.00	Co	0.1600	n
11 35 56.000	+42 58 44.64	B3 1133+432	1419.16	1448.8	21.39	23.66	Co	0.5690	uHA
11 40 27.690	+12 03 7.60	BWE 1137+1219	669.63	1527.0	16.50	15.32	I	0.0810	cHV
11 40 49.562	+59 12 25.38	4C 59.16	2187.20	2179.4	0.00	0.00	Co	0.0000	n
11 41 8.250	+01 14 17.74	3C 262	2846.79	2690.8	21.38	19.85	Co	0.5666	cHA
11 43 25.040	+22 06 56.00	3C 263.1	3095.70	3128.7	20.00	0.00	Co	0.3660	n
11 45 5.229	+19 36 37.80	3C 264	2090.46	5689.0	12.74	13.67	I	0.0214	n
11 45 31.181	+31 33 35.82	3C 265	2442.03	2890.9	20.00	0.00	II	0.8105	n
11 45 43.384	+49 46 7.90	3C 266	1471.82	1424.5	22.00	21.70	II	1.2750	c V
11 49 55.540	+12 47 15.90	3C 267	2266.56	2519.9	22.50	0.00	II	1.1440	n
11 50 43.890	-00 23 54.00	PKS 1148-00	2816.39	2773.9	17.77	17.60	Co	1.9762	c
11 53 24.455	+49 31 8.52	4C 49.22	1459.19	1572.2	17.40	16.10	Co	0.3339	c
11 54 13.011	+29 16 8.50	4C 29.44	1583.76	1620.3	19.20	18.00	I	0.3292	n
11 56 3.720	+58 47 4.92	S4 1153+590	1569.85	1591.7	18.40	18.62	Co	0.1568	uHV
11 56 18.746	+31 28 4.74	4C 31.38	2954.65	2978.3	19.33	18.96	Co	0.4180	c
11 59 13.771	+53 53 6.90	4C 54.25	1719.68	1740.6	20.63	20.48	Co	0.4122	cHA
11 59 31.842	+29 14 43.94	4C 29.45	1952.59	2030.8	16.80	15.60	Co	0.7290	n
12 00 59.000	+31 31 12.00	3C 268.2	907.29	1301.6	19.00	0.00	II	0.3620	n
12 04 2.476	-04 22 41.24	PKS 1201-041	1916.60	2141.3	18.00	0.00	I	0.1319	nH
12 06 19.931	+04 06 12.20	4C 04.40	1502.91	1501.2	22.06	20.94	II	0.7579	uHA
12 09 13.401	+43 39 16.89	3C 268.4	2049.01	1979.9	19.00	18.42	II	1.4000	c
12 12 56.057	+20 32 37.47	PKS 1210+20	1382.56	1417.9	19.70	18.50	Co	0.2808	nH
12 13 32.147	+13 07 20.44	PKS 1210+134	1356.25	1344.2	18.57	18.09	Co	1.1410	c
12 14 4.115	+33 09 45.74	B1211+334	1417.99	1403.6	17.95	17.90	Co	1.5980	c B
12 15 28.907	+53 36 7.16	4C 53.24	1377.88	2755.0	18.92	17.90	II	1.0650	c B
12 15 55.613	+34 48 15.02	4C 35.28	1407.90	1506.8	20.74	20.00	Co	0.8570	c B
12 19 15.329	+05 49 40.40	3C 270	316.39	10445.0	10.40	0.00	I	0.0073	n

12 20 33.888	+33 43 7.97	3C 270.1	2819.00	2845.9	18.80	18.61	Co	1.5190	u
12 24 30.200	+42 06 24.00	3C 272	1215.72	1352.3	22.00	0.00	II	0.9440	n
12 24 52.427	+03 30 50.35	PKS 1222+037	1348.77	1348.8	19.46	19.02	Co	0.9570	c
12 24 54.621	+21 22 47.20	4C 21.35	2024.87	2094.4	17.56	17.50	I	0.4350	n
12 25 3.781	+12 52 35.20	M84 (3C 272.1)	797.28	6012.8	10.80	8.67	I	0.0034	c
12 27 58.727	+36 35 11.96	B1225+368	2074.50	2098.4	21.50	21.50	Co	1.9730	c
12 29 6.410	+02 03 5.10	3C 273	53353.10	54991.2	13.07	12.86	Co	0.1583	c
12 30 49.460	+12 23 21.60	M87 (3C 274)	101109.16	138487.0	8.70	12.86	I	0.0043	c
12 31 59.955	-02 24 5.17	PKS 1229-02	1617.56	1646.7	17.23	16.75	Co	1.0450	c
12 35 22.971	+21 20 18.30	3C 274.1	1757.98	2918.5	20.00	0.00	II	0.4220	n
12 42 19.610	-04 46 20.45	3C 275	3600.19	3672.1	21.00	0.00	Co	0.4800	n
12 43 57.650	+16 22 48.13	3C 275.1	2819.51	2895.8	19.23	19.00	Co	0.5570	n
12 44 49.201	+40 48 6.35	S4 1242+41	1369.08	1341.8	19.00	19.00	Co	0.8130	c
12 52 26.324	+56 34 19.65	3C 277.1	2442.12	2288.3	17.76	17.93	Co	0.3200	c
12 53 3.549	+02 38 22.30	4C 02.34	1610.45	1604.9	19.00	19.42	II	0.2044	uHV
12 53 32.425	+15 42 25.29	3C 277.2	1406.92	1952.2	21.50	0.00	II	0.7660	n
12 54 11.678	+27 37 32.70	3C 277.3	2567.56	2923.9	15.94	0.00	II	0.0858	n
12 56 11.163	-05 47 21.70	3C 279	10708.10	9711.2	18.01	17.75	Co	0.5362	n
12 56 57.380	+47 20 19.80	3C 280	5064.38	5099.6	22.00	21.58	II	0.9960	u V
13 00 32.870	+40 09 9.20	3C 280.1	1326.97	1368.9	19.31	19.44	Co	1.6670	u
13 05 36.051	+08 55 15.90	4C 09.45	1508.02	1461.8	19.05	18.79	Co	1.4090	c A
13 09 49.660	-00 12 36.60	4C 00.46	1329.61	1636.7	19.40	19.73	II	0.4190	u V
13 10 28.668	+32 20 43.95	B1308+326	1686.60	1686.6	17.00	19.00	Co	0.9960	c
13 11 6.600	+27 26 6.00	3C 284	1334.54	2044.6	18.00	0.00	II	0.2394	n
13 13 37.870	+54 58 23.89	TXS 1311+552	1319.71	1304.6	23.44	21.74	Co	0.6130	cHA
13 19 38.734	-00 49 39.98	PKS 1317-00	1536.50	1468.9	17.84	17.32	Co	0.8920	c
13 20 21.450	+17 43 12.40	4C 17.56	1652.75	1573.2	19.50	0.00	II	0.2566	nH
13 21 18.803	+11 06 48.79	PKS 1318+11	2233.52	2238.0	19.25	19.13	Co	2.1710	c
13 21 20.300	+42 36 0.00	3C 285	739.45	2085.0	15.99	16.00	II	0.0794	n

13 26 16.513	+31 54 9.52	4C 32.44	4749.98	4861.9	19.00	19.00	Co	0.3700	c
13 27 31.709	+31 51 27.30	4C 32.44B	965.67	1415.1	18.50	18.25	I	0.2600	c V
13 30 37.694	+25 09 10.87	3C 287	6999.01	7052.2	18.30	17.67	Co	1.0550	n
13 31 8.285	+30 30 32.95	3C 286	15023.95	14902.7	17.51	17.25	II	0.8490	c
13 32 56.368	+02 00 46.50	3C 287.1	2029.13	2648.5	18.27	18.50	II	0.2155	n
13 38 8.071	-06 27 11.20	J1338-0627	2258.07	2958.5	17.82	17.68	I	0.6250	n
13 38 49.670	+38 51 11.10	3C 288	3195.65	3358.9	18.30	0.00	I	0.2460	n
13 42 13.085	+60 21 42.39	3C 288.1	1548.93	1493.3	18.51	18.12	Co	0.9610	c
13 42 43.570	+05 04 31.50	4C 05.57	1607.16	1600.9	17.80	16.86	I	0.1360	c V
13 44 23.749	+14 09 15.30	4C 14.49	1293.22	1302.8	20.00	0.00	Co	0.3226	nH
13 45 26.699	+49 46 31.39	3C 289	2405.00	2398.3	23.00	22.30	Co	0.9674	u V
13 47 1.736	-08 03 23.64	PKS 1344-07	1928.64	1906.3	0.00	0.00	I	0.3840	n
13 47 33.377	+12 17 24.09	PKS 1345+12	4859.88	5397.2	17.33	17.00	U	0.1217	c B
13 49 38.963	+21 07 28.89	3C 291	1346.66	1346.7	0.00	0.00	Co	0.0000	n
13 52 17.842	+31 26 46.48	3C 293	3709.14	4844.2	15.60	14.65	I	0.0450	c V
13 52 56.370	+11 07 7.67	PKS 1350+113	1566.65	1537.9	20.00	21.85	Co	0.6500	c V
13 57 1.510	+01 04 39.70	4C 01.39	2292.61	2400.4	24.48	22.17	II	0.8190	u A
13 57 4.437	+19 19 7.23	PKS 1354+19	2330.01	2585.6	16.20	16.02	I	0.7200	n
13 57 53.716	+00 46 33.46	PKS 1355+01	2000.43	1921.6	23.92	22.56	Co	1.6996	cHA
14 00 28.694	+62 10 38.41	4C 62.22	4374.44	4307.6	20.90	20.38	Co	0.4310	c V
14 06 44.101	+34 11 26.20	3C 294	1316.23	1316.1	23.49	23.64	II	1.7790	u A
14 11 20.592	+52 12 9.44	3C 295	22171.09	22720.1	20.10	19.25	II	0.4610	c V
14 13 48.342	-05 59 54.20	4C-05.60	1383.61	1520.8	0.00	0.00	II	1.0940	n
14 16 4.202	+34 44 36.60	S4 1413+34	1846.18	4445.3	0.00	0.00	Co	0.0000	n
14 16 53.499	+10 48 40.20	NGC 5532	387.20	1430.2	12.19	12.45	I	0.0240	c V
14 17 23.934	-04 00 46.66	3C 297	1539.82	1687.2	21.90	20.50	Co	1.4061	n
14 19 8.200	+06 28 34.74	3C 298	6155.57	6100.3	17.12	16.79	Co	1.4360	c
14 21 5.829	+41 44 49.98	3C 299	2886.19	3146.9	20.49	19.40	U	0.3670	u B
14 23 0.626	+19 35 17.41	3C 300	3069.12	3738.8	18.00	16.79	II	0.2720	n V

14 24 56.928	+20 00 22.70	7C 1422+2013	1859.46	1808.5	18.30	17.86	Co	0.8710	n
14 25 50.669	+24 04 6.70	4C 24.31	1479.51	1558.7	18.40	17.20	Co	0.6490	c
14 28 31.220	-01 24 8.70	3C 300.1	3064.68	3157.4	19.00	0.00	II	1.1590	n
14 36 57.024	+03 24 11.14	PKS 1434+03	2874.59	2797.3	19.00	0.00	Co	1.4380	n
14 38 44.762	+62 11 54.12	B1437+6224	2397.69	2410.4	19.54	19.00	Co	1.0900	c B
14 43 1.012	+52 01 40.79	3C 303	2119.30	2543.0	17.01	17.00	II	0.1410	c
14 45 16.483	+09 58 36.30	PKS 1442+101	2422.90	2417.6	18.58	17.78	Co	3.5220	c
14 48 39.981	+00 18 17.90	4C 00.52	1722.13	1651.5	19.50	0.00	I	0.2562	nH
14 49 21.786	+63 16 14.27	3C 305	2922.87	3006.0	13.74	13.74	I	0.0416	c
15 04 9.231	+60 00 55.53	3C 311	1552.94	1553.1	20.65	18.00	Co	1.0220	c B
15 04 24.977	+10 29 38.82	PKS 1502+106	1753.33	1774.2	18.87	15.50	Co	1.8390	c B
15 04 58.979	+25 59 49.00	3C 310	429.48	7613.4	15.24	15.93	I	0.0535	u V
15 10 53.593	-05 43 6.89	PKS 1508-05	3328.40	3569.3	17.10	0.00	Co	1.1910	n
15 10 57.030	+07 51 24.80	3C 313	2365.36	3799.1	21.00	19.99	II	0.4610	u V
15 12 25.548	+01 21 11.03	4C 01.42	2313.15	2262.7	22.82	21.32	I	0.7920	c A
15 13 39.899	+26 07 33.70	3C 315	982.06	4332.7	16.30	17.28	I	0.1080	c V
15 13 40.180	+23 38 35.34	PKS 1511+23	1722.12	1767.5	20.00	22.25	Co	0.3226	cHV
15 16 44.566	+07 01 19.36	3C 317	4479.02	5499.3	13.50	13.34	U	0.0344	c V
15 16 56.588	+18 30 21.77	3C 316	1363.18	1335.2	20.20	19.00	Co	0.3542	nH
15 20 5.485	+20 16 5.74	3C 318	2778.47	2688.0	20.30	20.23	Co	1.5740	c V
15 21 14.415	+04 30 21.69	PKS 1518+047	3924.44	3927.2	18.20	0.00	Co	1.2960	n
15 24 5.639	+54 28 18.40	3C 319	2116.45	2624.0	18.50	0.00	II	0.1920	n
15 25 48.956	+03 08 25.93	4C 03.33	2124.95	1960.0	0.00	0.00	Co	0.0000	n
15 31 25.360	+35 33 40.60	3CR 320	1802.50	1820.7	18.00	0.00	Co	0.3420	n
15 31 50.622	+24 02 42.33	3C 321	1312.35	3577.3	16.00	0.00	II	0.0962	n
15 34 52.449	+01 31 3.30	B1532+016	1283.42	1320.4	19.00	18.50	Co	1.4350	n
15 35 1.269	+55 36 49.80	3C 322	1824.08	1846.9	23.00	0.00	II	1.6810	n
15 37 32.369	+13 44 48.47	4C 13.56	1755.96	1805.6	21.91	0.00	Co	0.7106	nH
15 40 49.492	+14 47 46.09	PKS 1538+149	1482.61	1386.8	16.02	15.50	Co	0.6050	n

15 41 45.642	+60 15 36.20	3C 323	1304.37	1337.4	21.00	0.00	II	0.6790	n
15 46 9.531	+00 26 24.72	PKS 1543+005	1871.69	1830.3	22.78	21.12	Co	0.5500	c A
15 47 44.228	+20 52 41.00	3C 323.1	2082.57	2396.2	16.80	16.69	II	0.2640	n
15 49 49.170	+21 25 39.50	3C 324	2597.44	2522.0	21.50	21.92	II	1.2061	u V
15 49 59.206	+62 41 18.31	3C 325	3520.19	3563.7	22.20	21.00	Co	1.1350	n
15 50 35.266	+05 27 10.42	PKS 1548+056	2751.78	2303.3	18.50	17.70	Co	1.4220	c
15 52 26.800	+20 07 24.00	3C 326	111.07	3214.1	17.00	0.00	II	0.0900	n
15 56 9.984	+20 04 20.81	3C 326.1	2293.37	2313.7	21.20	20.00	Co	1.8250	n
15 56 36.351	+42 57 9.60	5C 13.42	1146.15	1656.4	22.59	0.00	II	0.9523	nH
16 02 7.228	+33 26 53.17	4C 33.38	2881.27	2990.6	24.20	23.00	Co	1.1000	n
16 02 17.212	+01 58 19.40	3C 327	5333.86	8298.7	15.88	0.00	II	0.1041	n
16 04 45.290	+01 17 51.70	3C 327.1	4446.05	4075.3	20.50	0.00	II	0.4630	n
16 05 46.571	+00 25 54.30	J1605+0025	1372.51	1376.6	21.00	19.90	II	0.4821	cHA
16 06 12.697	+00 00 27.40	4C 00.58	1987.34	2343.1	16.85	15.51	I	0.0590	c V
16 08 46.194	+10 29 7.70	PKS 1606+10	1402.43	1392.0	18.50	18.00	Co	1.2260	n
16 09 13.326	+26 41 29.00	PKS 1607+26	4845.05	4908.2	19.00	21.04	Co	0.4730	c V
16 12 18.971	+22 22 15.61	3C 331	1386.04	1401.9	22.35	20.85	Co	0.8586	cHA
16 13 41.058	+34 12 47.83	B1611+3420	3605.54	4024.1	17.98	17.50	Co	1.4010	c B
16 16 38.342	+26 47 1.40	PKS 1614+26	1412.82	1484.4	24.38	22.82	Co	2.0809	cHA
16 17 15.750	+21 07 29.40	3C 333	1718.15	1748.5	23.29	21.59	II	1.2903	uHA
16 17 43.277	+32 23 2.40	3C 332	2184.98	2598.5	16.00	16.00	II	0.1517	n
16 20 21.398	+17 36 29.30	3C 334	1700.01	1993.9	16.53	16.41	II	0.5550	n
16 24 39.695	+23 45 24.17	3C 336	2587.92	2612.7	17.91	17.47	II	0.9270	n
16 25 57.672	+41 34 40.60	4C 41.32	1717.27	1677.4	23.24	22.00	Co	2.5500	c B
16 28 3.572	+27 41 36.10	3C 341	1908.62	1998.6	19.00	0.00	II	0.4480	n
16 28 38.337	+39 33 0.00	3C 338	1922.45	3678.7	13.90	12.61	I	0.0266	cH
16 28 53.870	+44 19 3.52	3C 337	2490.08	3155.8	20.00	0.00	II	0.6300	n
16 29 37.862	+23 20 14.41	3C 340	2337.66	2599.0	22.00	0.00	II	0.7754	n
16 31 45.260	+11 56 3.19	PKS 1629+120	1674.02	1733.7	18.48	18.50	Co	1.7950	n

16 34 33.772	+62 45 35.36	3C 343	4987.55	5001.9	21.05	20.60	II	0.9880	n
16 35 15.483	+38 08 4.56	4C 38.41	2694.06	2726.0	17.90	18.00	Co	1.8135	c B
16 36 37.382	+26 48 6.60	3C 342	1347.66	1336.1	18.01	17.75	Co	0.5610	n
16 38 28.194	+62 34 43.95	3C 343.1	4740.74	4610.8	20.70	20.70	Co	0.7500	n
16 40 47.956	+12 20 2.08	4C 12.60	2159.37	2070.1	19.50	0.00	Co	1.1520	n
16 42 58.799	+39 48 37.16	3C 345	6598.61	7098.6	16.25	15.96	Co	0.5928	c
16 43 5.928	+37 29 34.40	3C 344	1365.92	1418.1	20.00	0.00	II	0.5200	n
16 43 48.696	+17 15 49.14	3C 346	3675.07	3666.2	17.20	0.00	I	0.1620	n
16 44 41.069	+13 05 15.10	4C 13.62	1358.49	1336.4	0.00	0.00	II	0.0000	n
16 47 41.835	+17 20 11.76	PKS 1645+17	2215.98	2130.2	18.50	0.00	Co	0.3140	n
16 53 52.214	+39 45 36.65	4C 39.49	1420.36	1558.0	14.54	13.80	B	0.0336	c
16 59 27.570	+47 03 13.10	3C 349	3104.99	3358.4	19.00	19.00	II	0.2050	n
17 04 7.198	+29 46 59.31	4C 29.50	1416.51	1413.9	19.29	19.14	Co	1.9270	c
17 04 43.427	+60 44 52.56	3C 351	2797.48	3259.0	15.41	15.28	II	0.3715	c
17 10 44.108	+46 01 30.30	3C 352	1956.83	1865.5	22.80	0.00	II	0.8060	n
17 19 8.937	+22 45 6.08	PKS 1717+22	1602.03	1574.9	19.50	18.30	Co	0.2528	n
17 24 18.400	+50 57 54.00	3C 356	1453.41	1509.1	21.50	0.00	II	1.0790	n
17 42 51.838	+61 45 51.00	4C 61.34	1343.28	1354.7	19.80	18.60	II	0.5230	n
21 34 10.335	-01 53 17.39	PKS 2131-021	1619.87	1689.5	18.60	19.00	Co	1.2850	n
21 36 38.600	+00 41 54.47	PKS 2134+004	3712.01	3472.5	17.10	16.79	Co	1.9320	c
22 23 48.000	-02 09 24.00	3C 445	744.57	4783.5	18.70	17.50	II	0.0564	n
23 26 54.468	-02 02 10.30	PKS 2324-02	538.48	2370.5	18.30	0.00	I	0.1880	n
23 32 25.585	-09 57 56.42	PKS 2329-10	1449.58	1425.7	19.50	19.06	Co	1.6800	c V
23 51 56.210	-01 09 16.30	B2349-0125	1460.41	1608.4	15.45	15.30	I	0.1740	c

A.2 Luminosity distribution

Column 1 correspond to the center of the luminosity bin, in $W.m^{-2}.Hz^{-1}$; column 2 corresponds to the number of sources in the given luminosity bin for the entire primary sample; column 3 corresponds to the number of sources in the given luminosity bin for the sub-sample of extended sources.

Table A.2: Data luminosity distribution for the entire sample

log(P) $(W.m^{-2}.Hz^{-1})$	N_{all}	N_{ext}
22.2	2.0	2.0
22.6	0.0	0.0
23.0	0.0	0.0
23.4	2.0	2.0
23.8	5.0	4.0
24.2	6.0	5.0
24.6	8.0	8.0
25.0	13.0	11.0
25.4	25.0	18.0
25.8	25.0	15.0
26.2	43.0	20.0
26.6	42.0	19.0
27.0	59.0	15.0
27.4	34.0	10.0
27.8	9.0	2.0
28.2	1.0	0.0
28.6	0.0	0.0

A.3 Source count

Columns 1 and 2 correspond to the log of the lower and higher limit of the flux density bin, in Jy; column 3 correspond to the value of the relative differential source count for the given flux density bin; column 4 correspond to the number of sources, not normalized to 1 sr, for each bin.

Table A.3: Data source count at 1.4GHz for the entire sample

S1	S2	$\Delta N/\Delta N_0$	N
(Jy)		$(sr^{-1}Jy^{1.5})$	
0.300	0.417	$-0.765^{+0.041}_{-0.040}$	104
0.417	0.500	$-0.870^{+0.063}_{-0.063}$	41
0.500	0.615	$-0.933^{+0.068}_{-0.068}$	35
0.615	0.810	$-0.939^{+0.069}_{-0.068}$	34
1.000	1.752	$-1.062^{+0.072}_{-0.072}$	31
1.752	2.699	$-0.986^{+0.198}_{-0.198}$	3
-0.152	0.026	$-0.737^{+0.037}_{-0.034}$	151
0.027	0.300	$-0.791^{+0.048}_{-0.042}$	92
-1.071	-0.979	$-0.870^{+0.022}_{-0.021}$	433
-0.870	-0.757	$-0.810^{+0.024}_{-0.023}$	340
-0.757	-0.611	$-0.805^{+0.029}_{-0.027}$	292
-0.611	-0.403	$-0.774^{+0.031}_{-0.029}$	246
-0.403	-0.158	$-0.714^{+0.035}_{-0.033}$	152
-2.658	-2.244	$-1.927^{+0.095}_{-0.078}$	9
-1.830	-1.415	$-1.298^{+0.096}_{-0.079}$	8
-1.415	-1.000	$-1.039^{+0.013}_{-0.012}$	8
-2.301	-2.000	$-1.737^{+0.196}_{-0.135}$	31
-2.000	-1.854	$-1.456^{+0.180}_{-0.127}$	25
-1.222	-0.824	$-0.882^{+0.104}_{-0.084}$	22
-3.682	-3.553	$-2.570^{+0.079}_{-0.067}$	17
-3.206	-2.984	$-2.462^{+0.113}_{-0.089}$	10
-2.984	-2.683	$-2.201^{+0.105}_{-0.085}$	10
-4.051	-3.955	$-2.660^{+0.167}_{-0.121}$	159
-3.955	-3.876	$-2.625^{+0.103}_{-0.084}$	157
-3.876	-3.799	$-2.606^{+0.042}_{-0.039}$	154
-3.799	-3.730	$-2.558^{+0.044}_{-0.040}$	157
-3.730	-3.644	$-2.578^{+0.037}_{-0.035}$	157
-3.644	-3.550	$-2.583^{+0.038}_{-0.035}$	150

-3.550	-3.425	$-2.609^{+0.038}_{-0.034}$	155
-3.425	-3.275	$-2.581^{+0.038}_{-0.035}$	151
-3.155	-3.004	$-2.561^{+0.050}_{-0.047}$	466
-3.000	-2.854	$-2.456^{+0.051}_{-0.047}$	372
-2.854	-2.703	$-2.298^{+0.053}_{-0.048}$	331
-2.703	-2.553	$-2.256^{+0.056}_{-0.050}$	222
-2.553	-2.402	$-2.043^{+0.057}_{-0.050}$	220
-2.600	-2.550	$-2.062^{+0.002}_{-0.002}$	36028
-2.550	-2.500	$-2.012^{+0.003}_{-0.002}$	33992
-2.500	-2.450	$-1.967^{+0.003}_{-0.002}$	31749
-2.450	-2.400	$-1.912^{+0.002}_{-0.003}$	30348
-2.400	-2.350	$-1.866^{+0.003}_{-0.003}$	28365
-2.350	-2.300	$-1.818^{+0.003}_{-0.002}$	26636
-2.300	-2.250	$-1.793^{+0.002}_{-0.003}$	23780
-2.250	-2.200	$-1.741^{+0.003}_{-0.003}$	22551
-2.200	-2.150	$-1.702^{+0.003}_{-0.003}$	20754
-2.150	-2.100	$-1.667^{+0.004}_{-0.003}$	18898
-2.100	-2.050	$-1.615^{+0.004}_{-0.003}$	17927
-2.050	-2.000	$-1.573^{+0.004}_{-0.003}$	16615
-2.000	-1.950	$-1.538^{+0.004}_{-0.003}$	15159
-1.950	-1.900	$-1.505^{+0.004}_{-0.004}$	13765
-1.900	-1.850	$-1.457^{+0.004}_{-0.003}$	12927
-1.850	-1.800	$-1.419^{+0.004}_{-0.004}$	11893
-1.800	-1.750	$-1.381^{+0.004}_{-0.004}$	10905
-1.750	-1.700	$-1.350^{+0.005}_{-0.004}$	9852
-1.700	-1.650	$-1.315^{+0.004}_{-0.005}$	9000
-1.650	-1.600	$-1.269^{+0.005}_{-0.004}$	8403
-1.600	-1.550	$-1.253^{+0.005}_{-0.005}$	7350
-1.550	-1.500	$-1.208^{+0.006}_{-0.005}$	6845
-1.500	-1.450	$-1.177^{+0.006}_{-0.005}$	6190
-1.450	-1.400	$-1.156^{+0.005}_{-0.006}$	5473
-1.400	-1.350	$-1.110^{+0.006}_{-0.006}$	5114
-1.350	-1.300	$-1.090^{+0.007}_{-0.006}$	4503
-1.300	-1.250	$-1.063^{+0.006}_{-0.007}$	4039
-1.250	-1.200	$-1.042^{+0.007}_{-0.007}$	3564
-1.200	-1.150	$-1.009^{+0.008}_{-0.007}$	3233
-1.150	-1.100	$-0.992^{+0.008}_{-0.008}$	2830

-1.100	-1.050	$-0.946^{+0.009}_{-0.008}$	2645
-1.050	-1.000	$-0.929^{+0.009}_{-0.008}$	2314
-1.000	-0.950	$-0.919^{+0.010}_{-0.009}$	1993

Appendix B

Results tables - Local luminosity function

B.1 Entire primary sample

Column 1 correspond to the luminosity in $W.m^{-2}.Hz^{-1}$; columns 2 and 3 correspond to the value of the local luminosity function estimated using model 1 and 3 respectively, in Mpc^{-3}.

Table B.1: Modeled local luminosity function for the entire primary sample

log(P) $(W.m^{-2}.Hz^{-1})$	$log(\rho_0)$ (Mpc^{-3})	
	model 1	model 3
20.6	$-3.2620^{+1.00}_{-0.30}$	$-3.2620^{+1.00}_{-0.30}$
21.0	$-3.7420^{+1.00}_{-0.30}$	$-3.7420^{+1.00}_{-0.30}$
21.4	$-3.5920^{+0.30}_{-0.18}$	$-3.5920^{+0.30}_{-0.18}$
21.8	$-3.4920^{+0.09}_{-0.08}$	$-3.4920^{+0.09}_{-0.08}$
22.2	$-3.7020^{+0.06}_{-0.05}$	$-3.7020^{+0.06}_{-0.05}$
22.6	$-4.1420^{+0.05}_{-0.05}$	$-4.1420^{+0.05}_{-0.05}$
23.0	$-4.5620^{+0.04}_{-0.04}$	$-4.5620^{+0.04}_{-0.04}$
23.4	$-5.0440^{+0.05}_{-0.05}$	$-5.0619^{+0.05}_{-0.05}$
23.8	$-5.3639^{+0.04}_{-0.04}$	$-5.3899^{+0.04}_{-0.04}$
24.2	$-5.0167^{+0.46}_{-0.46}$	$-5.2032^{+0.46}_{-0.46}$
24.6	$-5.5839^{+0.43}_{-0.43}$	$-5.8415^{+0.43}_{-0.43}$
25.0	$-6.0919^{+0.39}_{-0.39}$	$-6.4327^{+0.39}_{-0.39}$
25.4	$-6.5344^{+0.31}_{-0.31}$	$-6.9619^{+0.31}_{-0.31}$
25.8	$-7.3112^{+0.31}_{-0.31}$	$-7.8075^{+0.31}_{-0.31}$
26.2	$-7.9107^{+0.26}_{-0.26}$	$-8.4286^{+0.26}_{-0.26}$
26.6	$-8.8117^{+0.26}_{-0.26}$	$-9.2741^{+0.26}_{-0.26}$
27.0	$-9.5631^{+0.23}_{-0.23}$	$-9.8728^{+0.23}_{-0.23}$
27.4	$-10.6671^{+0.28}_{-0.28}$	$-10.7307^{+0.28}_{-0.28}$
27.8	$-12.0236^{+0.44}_{-0.44}$	$-11.7723^{+0.44}_{-0.44}$

B.2 Extended sources only

Column 1 correspond to the luminosity in $W.m^{-2}.Hz^{-1}$; columns 2 and 3 correspond to the value of the local luminosity function estimated using model 1, 2 and 3 respectively, in Mpc^{-3}.

Table B.2: Modeled local luminosity function for the extended sources only

log(P) $(W.m^{-2}.Hz^{-1})$	$log(\rho_0)$ (Mpc^{-3})		
	model 1	model 2	model 3
21.8	$-4.6920^{+0.53}_{-0.23}$	$-4.6920^{+0.53}_{-0.23}$	$-4.6920^{+0.53}_{-0.23}$
22.2	$-4.5220^{+0.19}_{-0.13}$	$-4.5220^{+0.19}_{-0.13}$	$-4.5220^{+0.19}_{-0.13}$
22.6	$-4.7320^{+0.10}_{-0.08}$	$-4.7320^{+0.10}_{-0.08}$	$-4.7320^{+0.10}_{-0.08}$
23.0	$-4.9820^{+0.07}_{-0.06}$	$-4.9820^{+0.07}_{-0.06}$	$-4.9820^{+0.07}_{-0.06}$
23.4	$-4.7267^{+0.06}_{-0.06}$	$-4.7328^{+0.06}_{-0.06}$	$-4.7993^{+0.06}_{-0.06}$
23.8	$-5.1738^{+0.05}_{-0.05}$	$-5.1905^{+0.05}_{-0.05}$	$-5.2536^{+0.05}_{-0.05}$
24.2	$-4.5749^{+0.35}_{-0.35}$	$-4.6522^{+0.35}_{-0.35}$	$-4.8241^{+0.35}_{-0.35}$
24.6	$-5.2398^{+0.37}_{-0.37}$	$-5.3898^{+0.37}_{-0.37}$	$-5.6121^{+0.37}_{-0.37}$
25.0	$-5.7978^{+0.34}_{-0.34}$	$-5.9667^{+0.34}_{-0.34}$	$-6.2370^{+0.34}_{-0.34}$
25.4	$-6.5956^{+0.34}_{-0.34}$	$-6.7578^{+0.34}_{-0.34}$	$-7.0589^{+0.34}_{-0.34}$
25.8	$-7.6139^{+0.37}_{-0.37}$	$-7.7178^{+0.37}_{-0.37}$	$-8.0058^{+0.37}_{-0.37}$
26.2	$-8.8874^{+0.42}_{-0.42}$	$-8.8522^{+0.42}_{-0.42}$	$-9.0507^{+0.42}_{-0.42}$
26.6	$-10.4881^{+0.67}_{-0.67}$	$-10.5924^{+0.67}_{-0.67}$	$-10.5985^{+0.67}_{-0.67}$
27.0	$-14.8203^{+2.35}_{-2.35}$	$-14.9226^{+2.35}_{-2.35}$	$-14.9590^{+2.35}_{-2.35}$
27.4	$-14.8151^{+2.03}_{-2.03}$	$-14.2694^{+2.03}_{-2.03}$	$-14.9781^{+2.03}_{-2.03}$
27.8	$-14.6727^{+1.70}_{-1.70}$	$-13.6108^{+1.70}_{-1.70}$	$-14.8547^{+1.70}_{-1.70}$

Appendix C

Contour plots

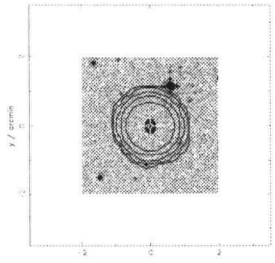

00 06 22.611 -00 04 24.48
3C 002

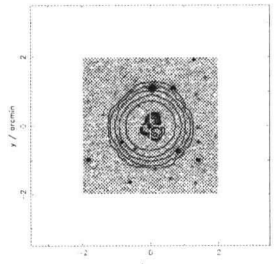

00 38 20.410 -02 07 40.40
3C 017

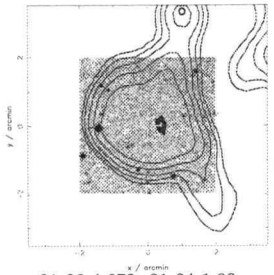

01 26 4.670 -01 24 1.90
NGC 547

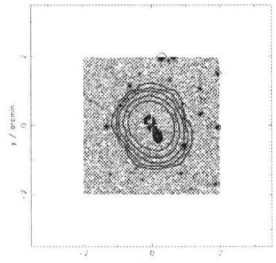

00 13 10.910 +00 51 42.40
3C 005

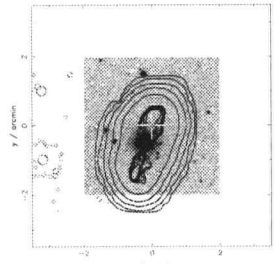

00 57 34.150 -01 22 58.40
3C 029

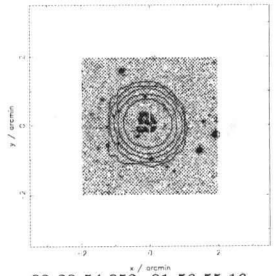

02 20 54.052 -01 56 55.16
3C 063

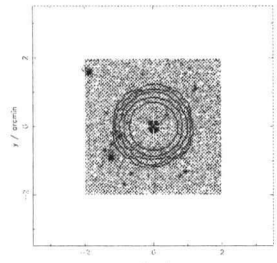

00 22 25.437 +00 14 56.08
PKS 0019-00

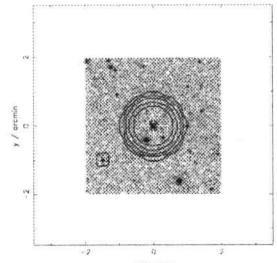

00 59 05.511 +00 06 51.70
PKS 0056-00

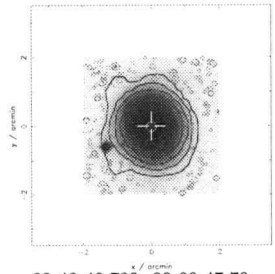

02 42 40.720 -00 00 47.70
M77

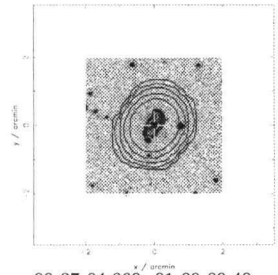

00 37 04.060 -01 09 09.40
3C 015

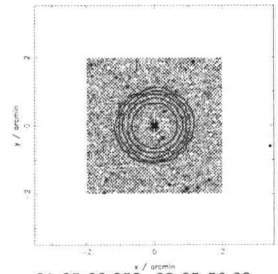

01 25 28.853 -00 05 56.20
PKS 0122-00

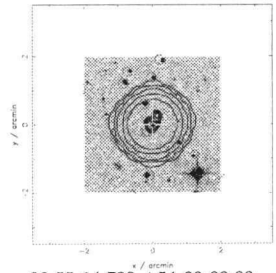

06 55 14.780 +54 09 00.00
3C 171

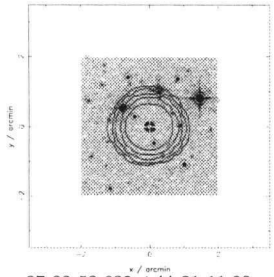

07 02 53.639 +44 31 11.92
4C 44.15

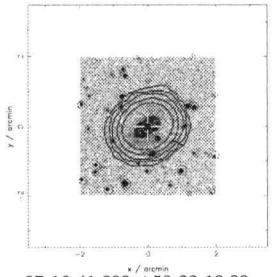

07 16 41.090 +53 23 10.30
4C 53.16

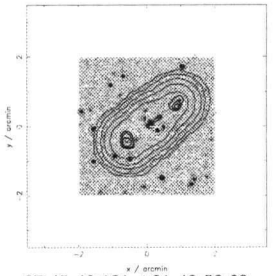

07 45 42.131 +31 42 52.60
4C 31.30

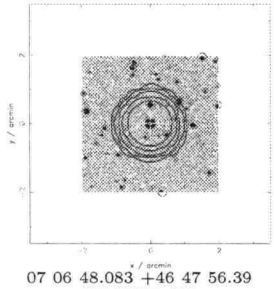

07 06 48.083 +46 47 56.39
B3 0703+468

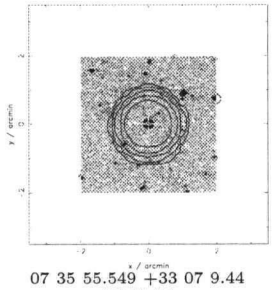

07 35 55.549 +33 07 9.44
4C 33.21

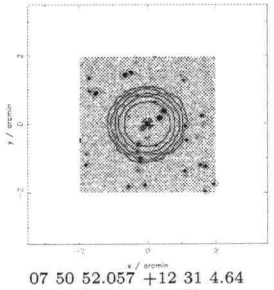

07 50 52.057 +12 31 4.64
PKS 0748+126

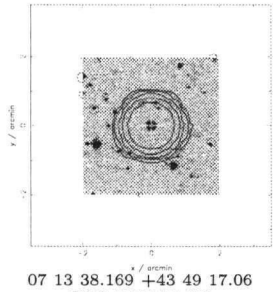

07 13 38.169 +43 49 17.06
QSO B0710+439

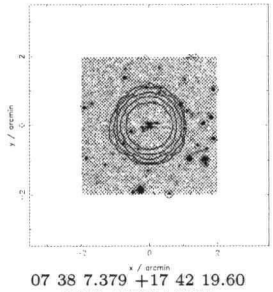

07 38 7.379 +17 42 19.60
QSO J0738+1742

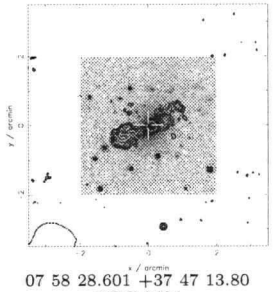

07 58 28.601 +37 47 13.80
NGC 2484

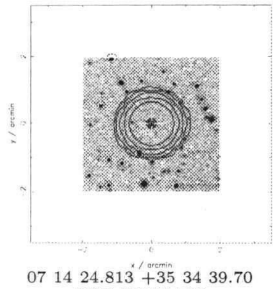

07 14 24.813 +35 34 39.70
QSO B0711+35

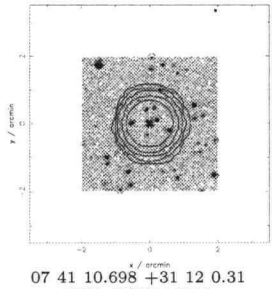

07 41 10.698 +31 12 0.31
QSO J0741+3111

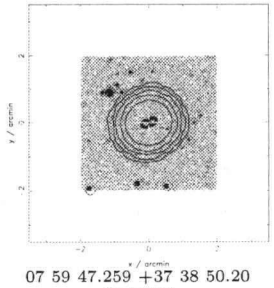

07 59 47.259 +37 38 50.20
4C 37.21

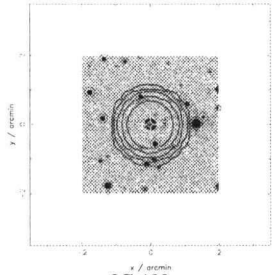

3C 190
08 01 33.507 +14 14 42.66

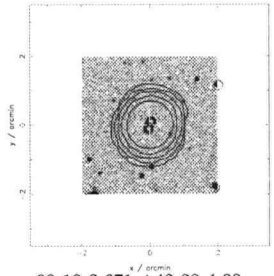

08 10 3.671 +42 28 4.00
3C 194

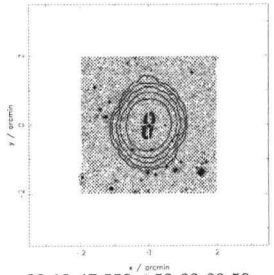

08 19 47.550 +52 32 29.50
4C 52.18

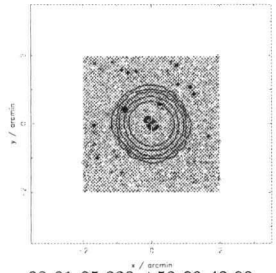

08 01 35.320 +50 09 43.00
TXS 0757+503

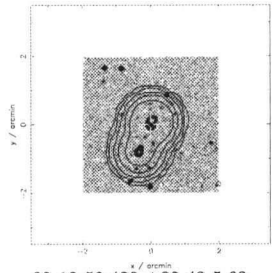

08 12 59.480 +32 43 5.60
4C 32.24

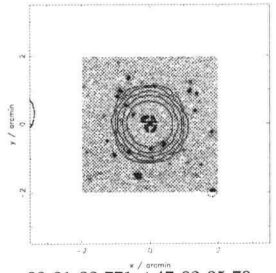

08 21 33.771 +47 02 35.70
3C 197.1

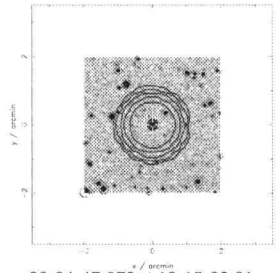

08 04 47.970 +10 15 22.91
3C 191

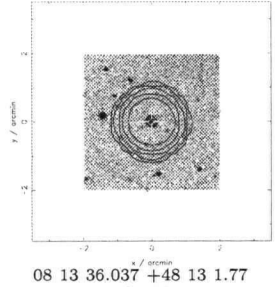

08 13 36.037 +48 13 1.77
3C 196

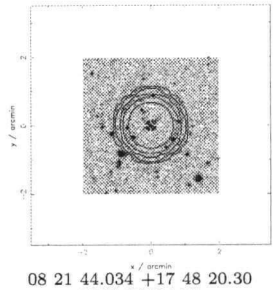

08 21 44.034 +17 48 20.30
PKS 0818+17

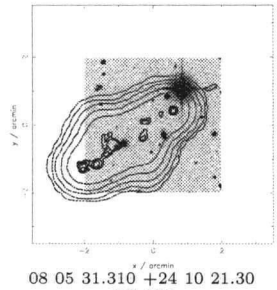

08 05 31.310 +24 10 21.30
3C 192

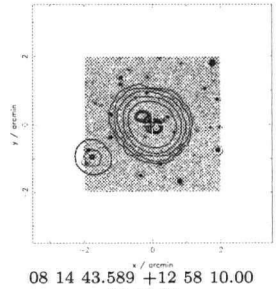

08 14 43.589 +12 58 10.00
4C 13.37

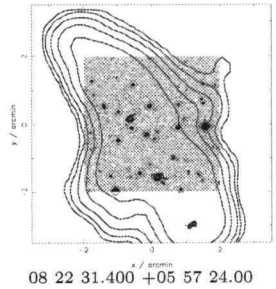

08 22 31.400 +05 57 24.00
3C 198

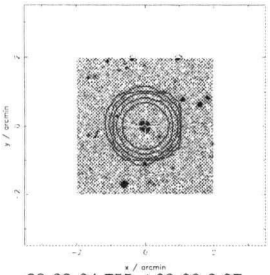

08 23 24.755 +22 23 3.27
PKS 0820+22

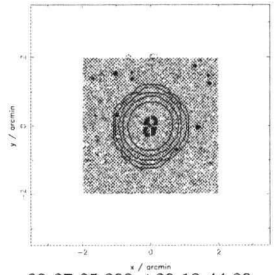

08 27 25.398 +29 18 44.80
3C 200

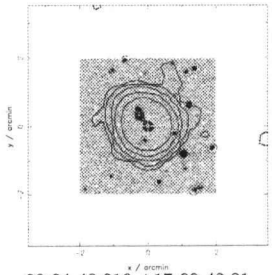

08 34 48.216 +17 00 42.81
3C 202

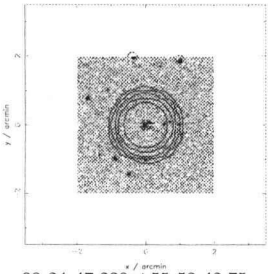

08 24 47.239 +55 52 42.75
4C 56.16A

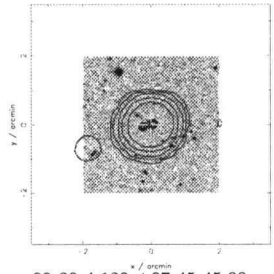

08 30 4.120 +07 45 45.00
PKS 0830+0745

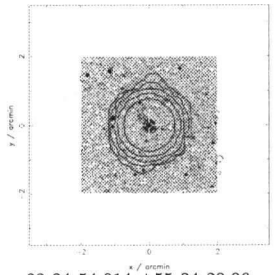

08 34 54.914 +55 34 20.96
4C 55.16

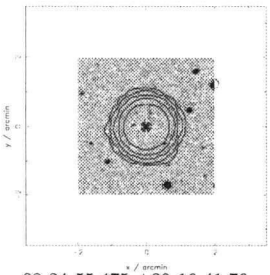

08 24 55.475 +39 16 41.76
4C 39.23A

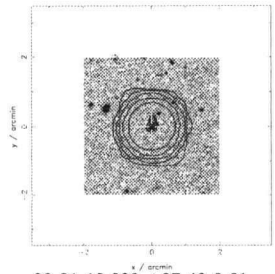

08 31 10.032 +37 42 9.61
4C 37.24

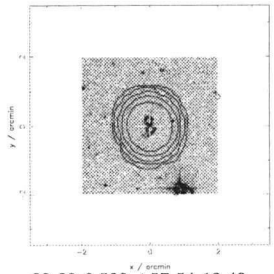

08 39 6.500 +57 54 13.40
3C 205

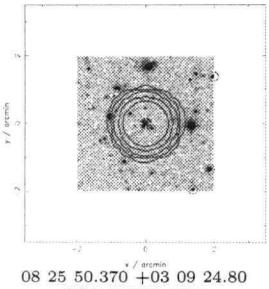

08 25 50.370 +03 09 24.80
QSO B0823+033

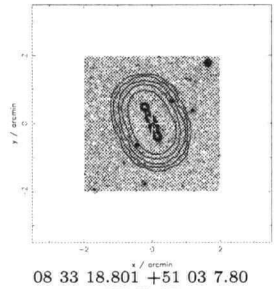

08 33 18.801 +51 03 7.80
4C 51.25

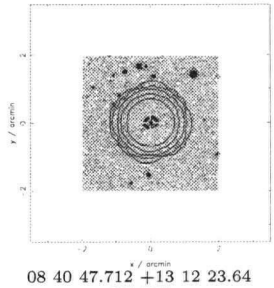

08 40 47.712 +13 12 23.64
3C 207

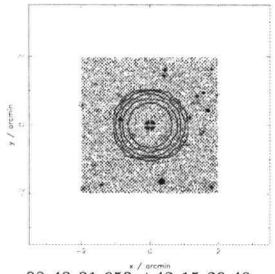

08 43 31.653 +42 15 29.49
B3 0840+424A

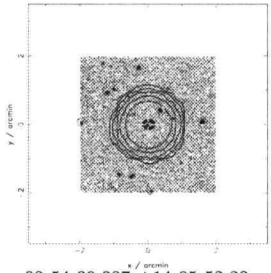

08 54 39.387 +14 05 52.23
3C 208.1

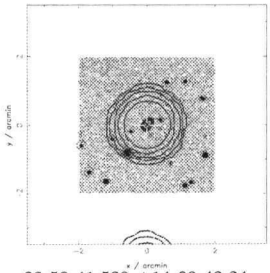

08 58 41.539 +14 09 43.24
3C 212

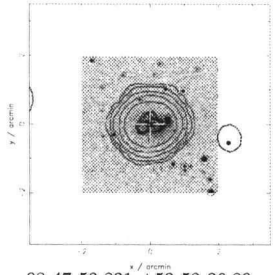

08 47 53.831 +53 52 36.80
S4 0844+54

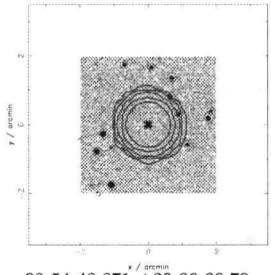

08 54 48.871 +20 06 30.70
QSO J0854+2006

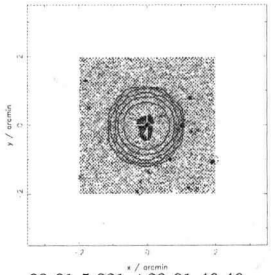

09 01 5.321 +29 01 46.46
3C 213.1

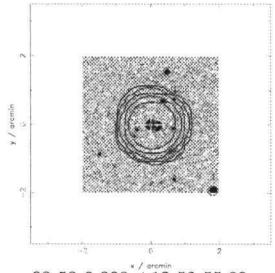

08 53 9.008 +13 52 55.83
3C 208

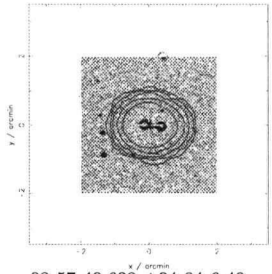

08 57 40.638 +34 04 6.40
3C 211

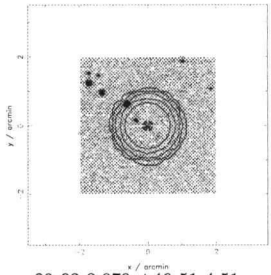

09 03 3.979 +46 51 4.51
4C 47.29

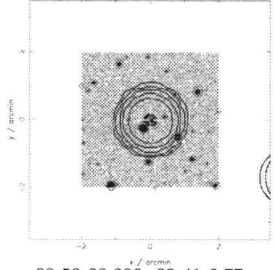

08 53 28.286 -03 41 6.77
PKS 0850-03

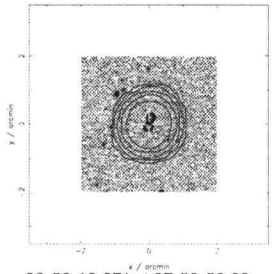

08 58 10.071 +27 50 50.80
3C 210

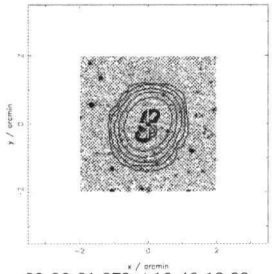

09 06 31.879 +16 46 13.00
3C 215

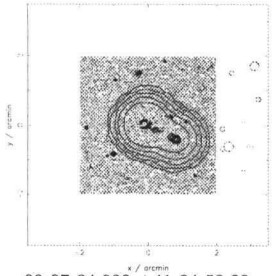

09 07 34.920 +41 34 53.80
4C 41.19

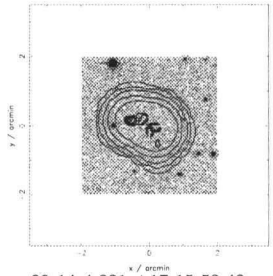

09 14 4.831 +17 15 52.40
4C 17.48

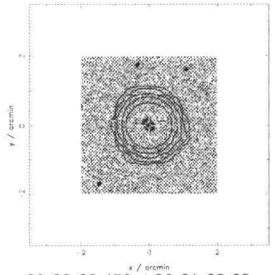

09 30 33.450 +36 01 23.60
3C 220.2

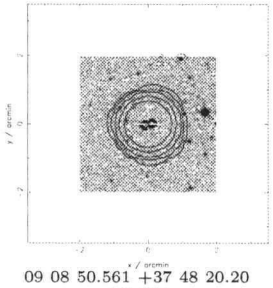

09 08 50.561 +37 48 20.20
3C 217

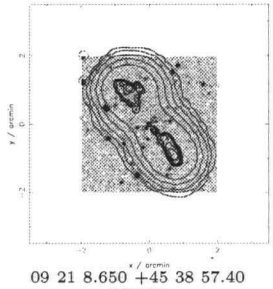

09 21 8.650 +45 38 57.40
3C 219

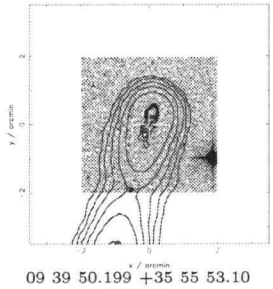

09 39 50.199 +35 55 53.10
3C 223

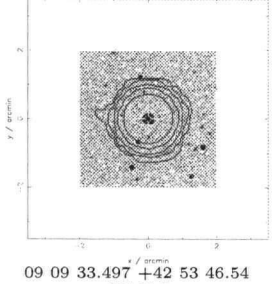

09 09 33.497 +42 53 46.54
3C 216

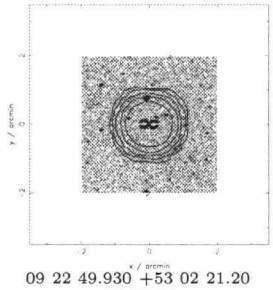

09 22 49.930 +53 02 21.20
4C 53.18

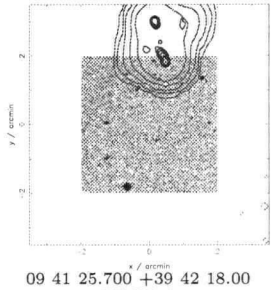

09 41 25.700 +39 42 18.00
3C 223.1

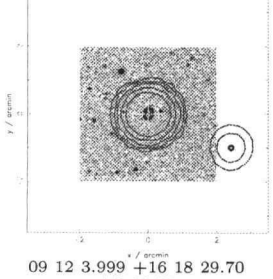

09 12 3.999 +16 18 29.70
4C 16.27

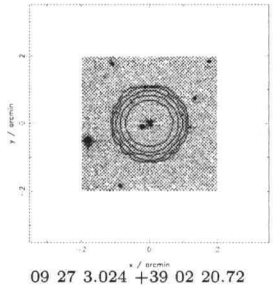

09 27 3.024 +39 02 20.72
4C 39.25

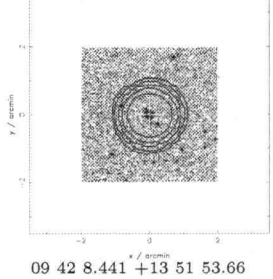

09 42 8.441 +13 51 53.66
3CR 225A

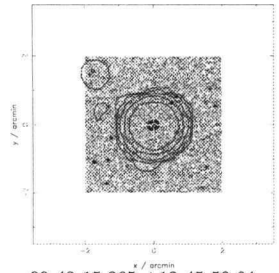

09 42 15.365 +13 45 50.64
3C 225

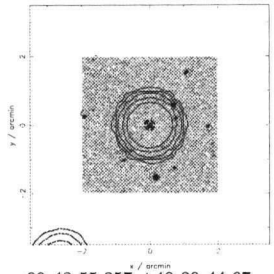

09 48 55.357 +40 39 44.67
4C 40.24

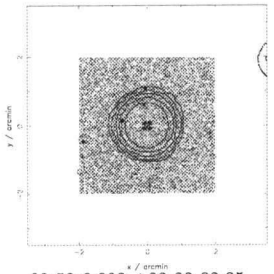

09 52 6.090 +28 28 32.35
4C 28.24

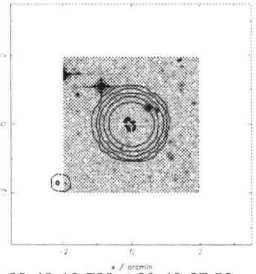

09 43 12.739 +02 43 27.50
SDSS J094312.82+024325.8

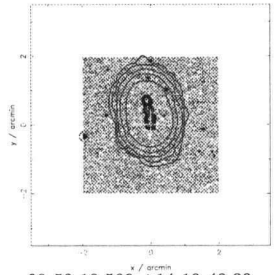

09 50 10.566 +14 19 40.30
3C 228

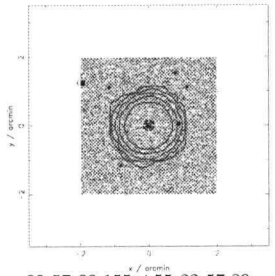

09 57 38.155 +55 22 57.89
4C 55.17

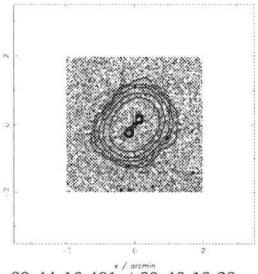

09 44 16.401 +09 46 19.20
3C 226

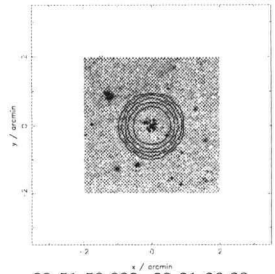

09 51 58.830 -00 01 26.80
3C 230

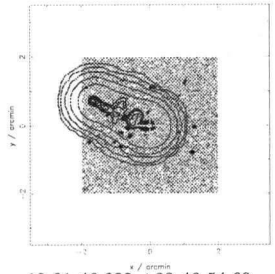

10 01 46.200 +28 46 54.69
3C 234

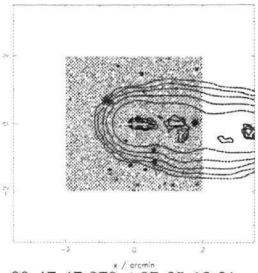

09 47 47.270 +07 25 13.81
3C 227

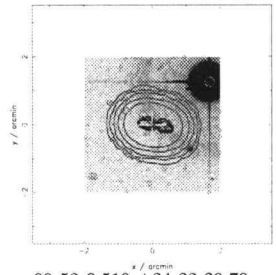

09 52 0.519 +24 22 29.70
3C 229

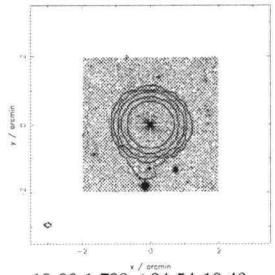

10 06 1.738 +34 54 10.43
3C 236

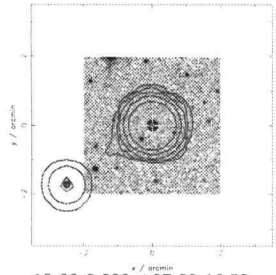

10 08 0.033 +07 30 16.50
3C 237

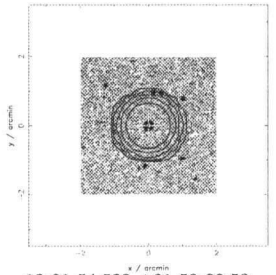

10 21 54.533 +21 59 30.50
3C 241

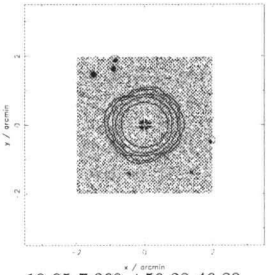

10 35 7.069 +56 28 46.83
QSO B1031+567

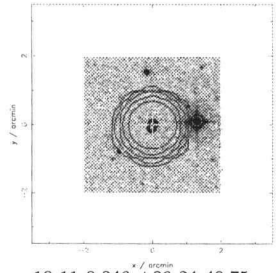

10 11 0.346 +06 24 40.75
3C 238

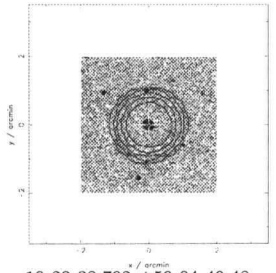

10 23 38.792 +59 04 49.48
S4 1020+59

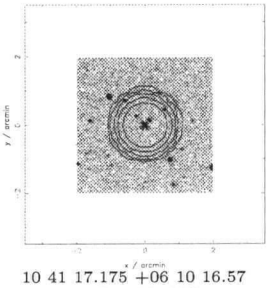

10 41 17.175 +06 10 16.57
PKS 1038+064

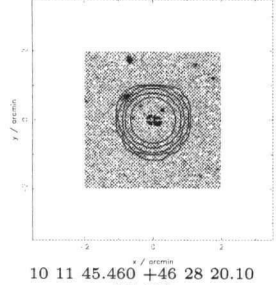

10 11 45.460 +46 28 20.10
3C 239

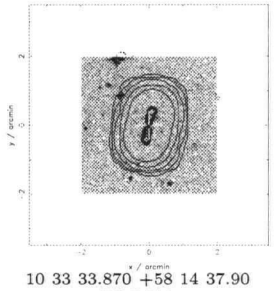

10 33 33.870 +58 14 37.90
3C 244.1

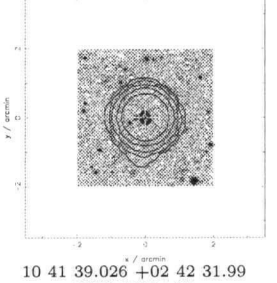

10 41 39.026 +02 42 31.99
PKS 1039+02

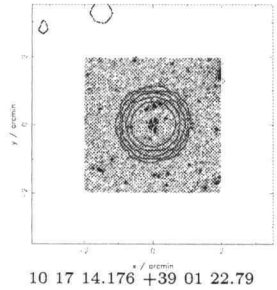

10 17 14.176 +39 01 22.79
B3 1014+392

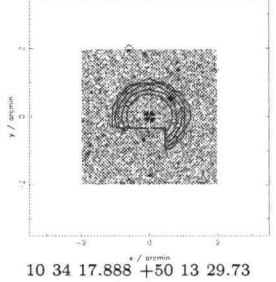

10 34 17.888 +50 13 29.73
4C 50.30

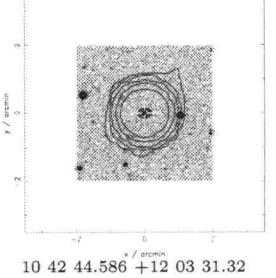

10 42 44.586 +12 03 31.32
3C 245

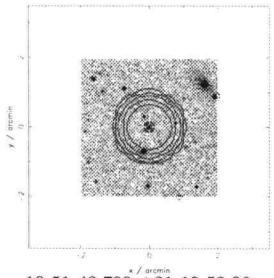

10 51 48.799 +21 19 52.36
PKS 1049+215

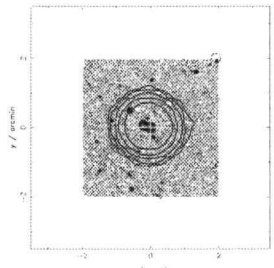

10 58 58.360 +43 01 21.66
3C 247

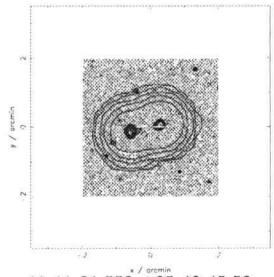

11 11 31.558 +35 40 45.50
3C 252

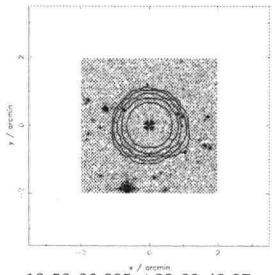

10 52 26.095 +20 29 48.07
4C 20.23

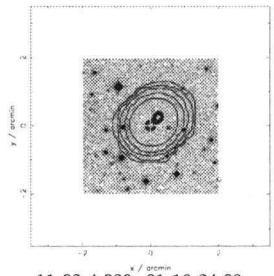

11 02 4.329 -01 16 24.09
3C 249

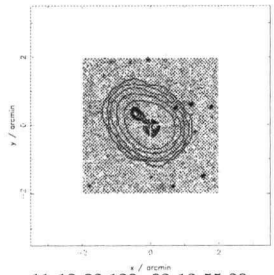

11 13 32.130 -02 12 55.20
3C 253

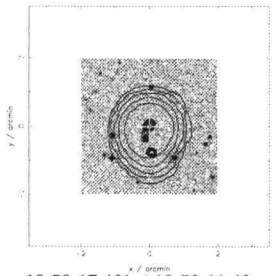

10 58 17.461 +19 52 11.40
PKS 1055+20

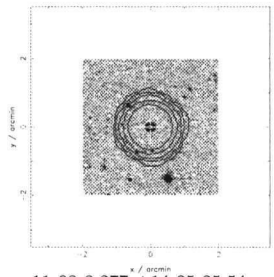

11 08 8.277 +14 35 35.54
PKS 1105+14

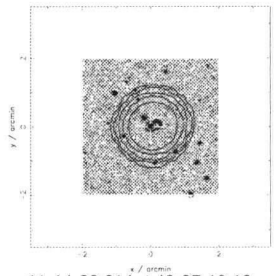

11 14 38.814 +40 37 19.13
3C 254

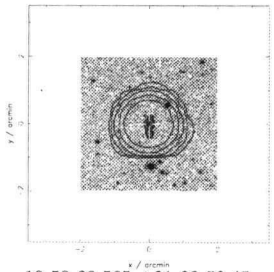

10 58 29.565 +01 33 58.45
PKS 1055+01

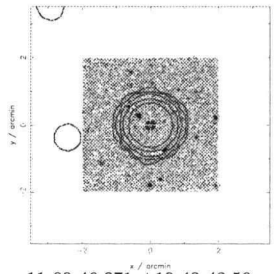

11 09 46.071 +10 43 43.56
PKS 1107+10

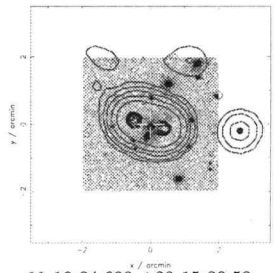

11 16 34.699 +29 15 20.50
4C 29.41

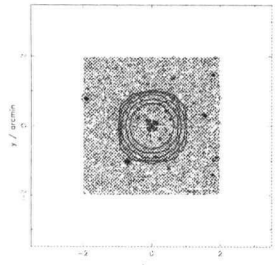

11 18 57.297 +12 34 41.86
PKS 1116+12

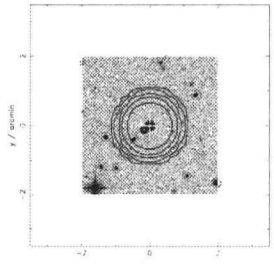

11 23 9.062 +05 30 20.58
3C 257

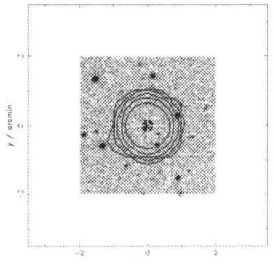

11 35 13.029 -00 21 18.75
PKS 1132-000

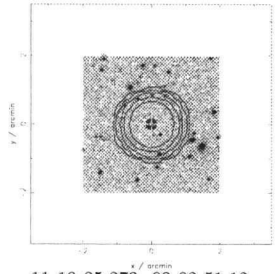

11 19 25.273 -03 02 51.12
3C 255

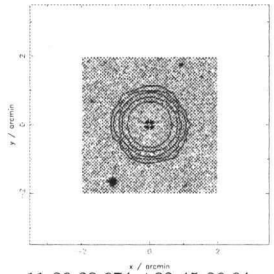

11 26 23.674 +33 45 26.64
4C 33.26

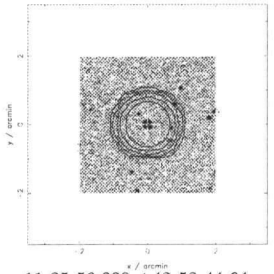

11 35 56.000 +42 58 44.64
B3 1133+432

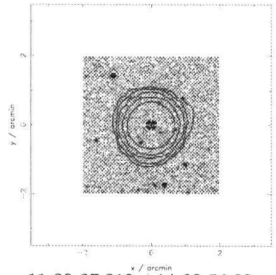

11 20 27.810 +14 20 54.99
PKS 1117+14

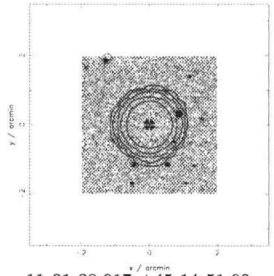

11 31 38.917 +45 14 51.00
B3 1128+455

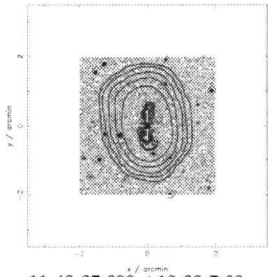

11 40 27.690 +12 03 7.60
BWE 1137+1219

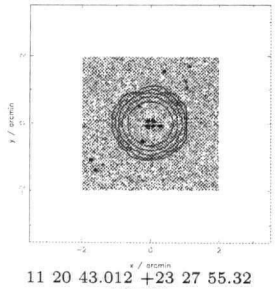

11 20 43.012 +23 27 55.32
3C 256

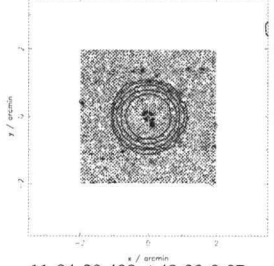

11 34 38.490 +43 28 0.67
4C 43.22

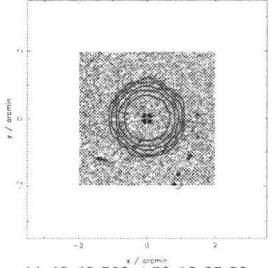

11 40 49.562 +59 12 25.38
4C 59.16

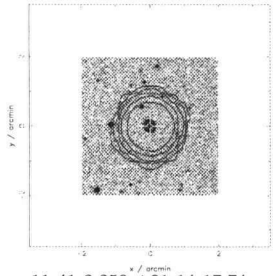

11 41 8.250 +01 14 17.74
3C 262

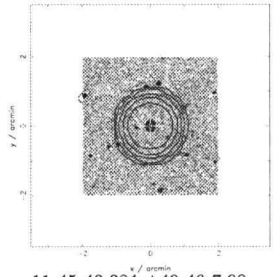

11 45 43.384 +49 46 7.90
3C 266

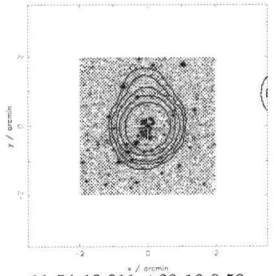

11 54 13.011 +29 16 8.50
4C 29.44

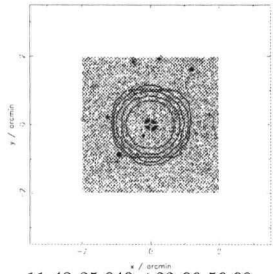

11 43 25.040 +22 06 56.00
3C 263.1

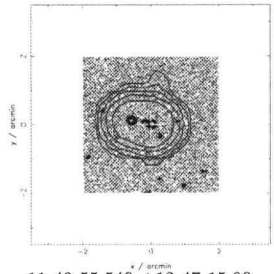

11 49 55.540 +12 47 15.90
3C 267

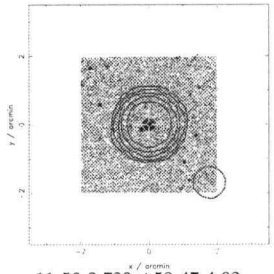

11 56 3.720 +58 47 4.92
S4 1153+590

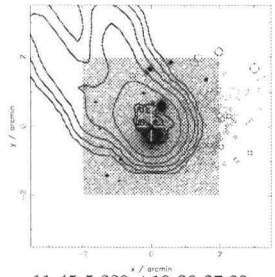

11 45 5.229 +19 36 37.80
3C 264

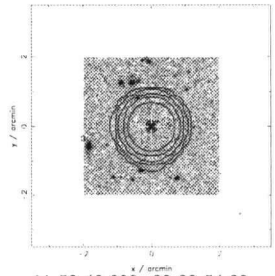

11 50 43.890 -00 23 54.00
PKS 1148-00

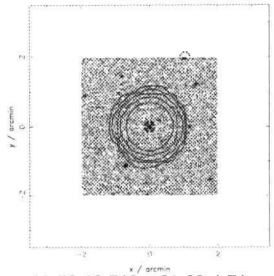

11 56 18.746 +31 28 4.74
4C 31.38

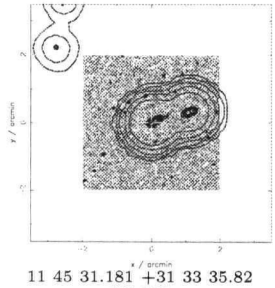

11 45 31.181 +31 33 35.82
3C 265

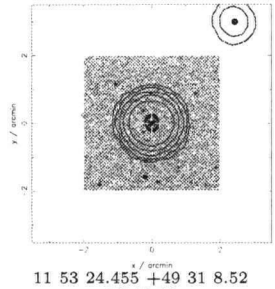

11 53 24.455 +49 31 8.52
4C 49.22

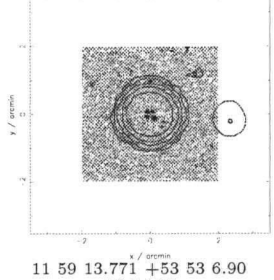

11 59 13.771 +53 53 6.90
4C 54.25

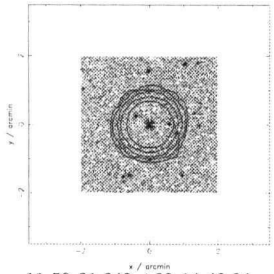

11 59 31.842 +29 14 43.94
4C 29.45

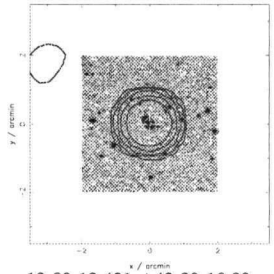

12 09 13.401 +43 39 16.89
3C 268.4

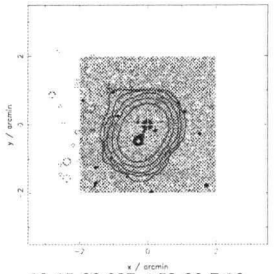

12 15 28.907 +53 36 7.16
4C 53.24

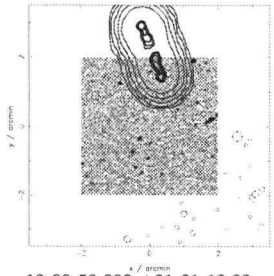

12 00 59.000 +31 31 12.00
3C 268.2

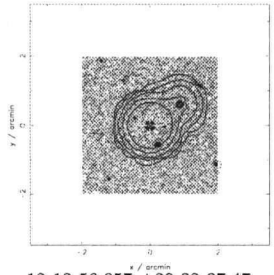

12 12 56.057 +20 32 37.47
PKS 1210+20

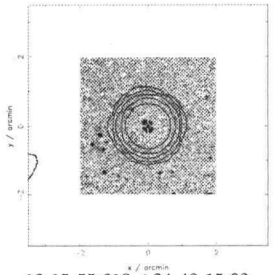

12 15 55.613 +34 48 15.02
4C 35.28

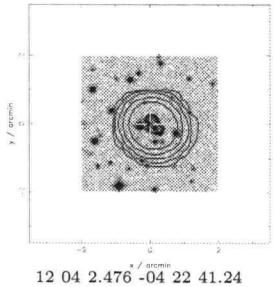

12 04 2.476 -04 22 41.24
PKS 1201-041

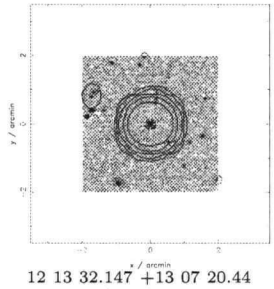

12 13 32.147 +13 07 20.44
PKS 1210+134

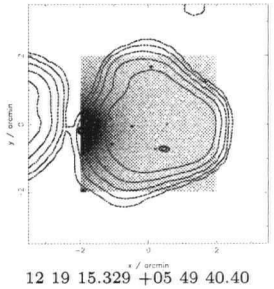

12 19 15.329 +05 49 40.40
3C 270

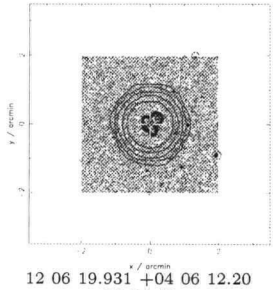

12 06 19.931 +04 06 12.20
4C 04.40

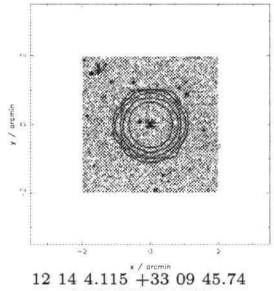

12 14 4.115 +33 09 45.74
QSO B1211+334

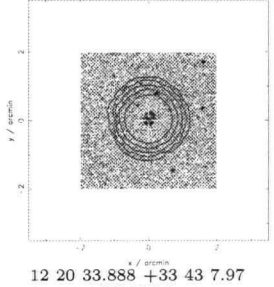

12 20 33.888 +33 43 7.97
3C 270.1

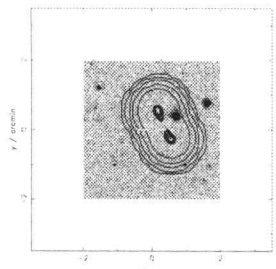

12 24 30.200 +42 06 24.00
3C 272

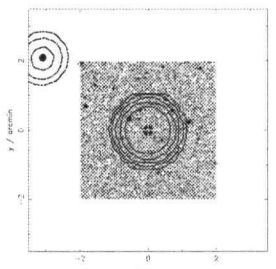

12 27 58.727 +36 35 11.96
QSO B1225+368

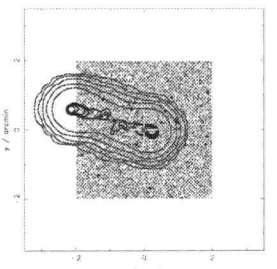

12 35 22.971 +21 20 18.30
3C 274.1

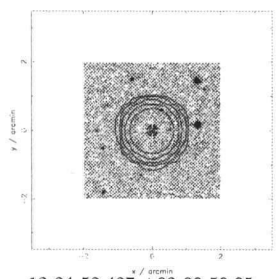

12 24 52.427 +03 30 50.35
PKS 1222+037

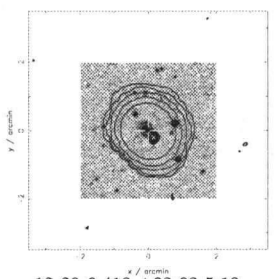

12 29 6.410 +02 03 5.10
3C 273

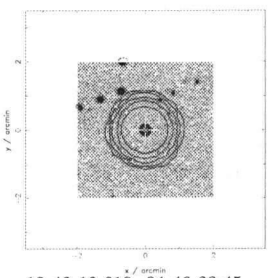

12 42 19.610 -04 46 20.45
3C 275

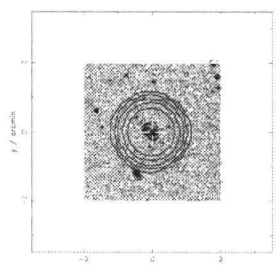

12 24 54.621 +21 22 47.20
4C 21.35

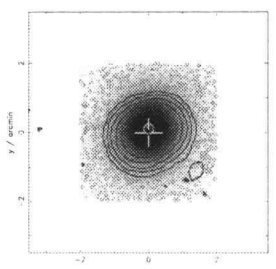

12 30 49.460 +12 23 21.60
M87

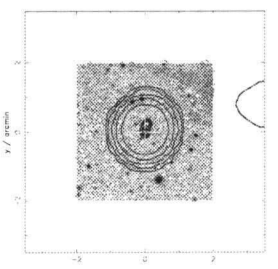

12 43 57.650 +16 22 48.13
3C 275.1

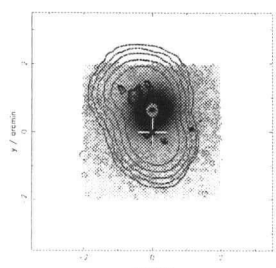

12 25 3.781 +12 52 35.20
M84

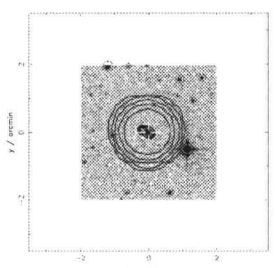

12 31 59.955 -02 24 5.17
PKS 1229-02

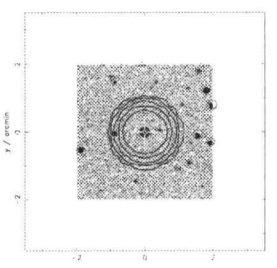

12 44 49.201 +40 48 6.35
S4 1242+41

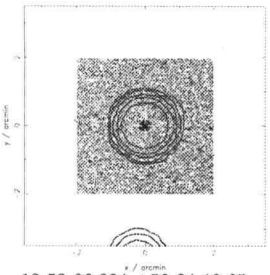

12 52 26.324 +56 34 19.65
3C 277.1

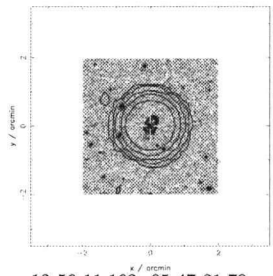

12 56 11.163 -05 47 21.70
3C 279

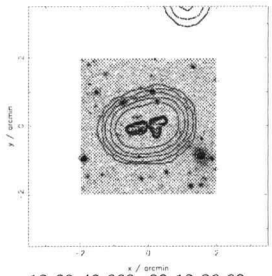

13 09 49.660 -00 12 36.60
4C 00.46

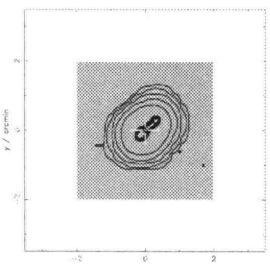

12 53 3.549 +02 38 22.30
4C 02.34

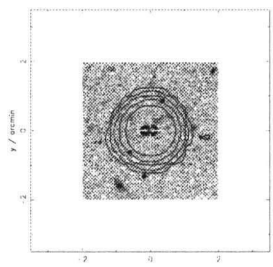

12 56 57.380 +47 20 19.80
3C 280

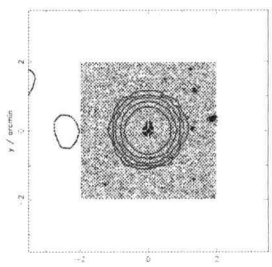

13 10 28.668 +32 20 43.95
QSO B1308+326

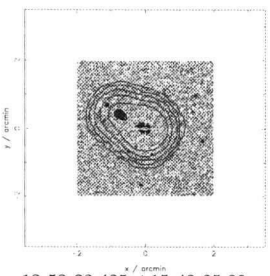

12 53 32.425 +15 42 25.29
3C 277.2

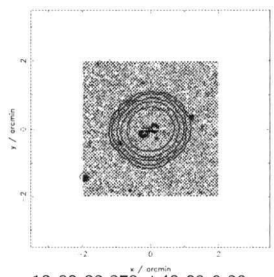

13 00 32.870 +40 09 9.20
3C 280.1

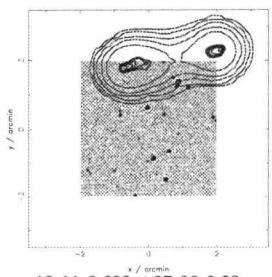

13 11 6.600 +27 26 6.00
3C 284

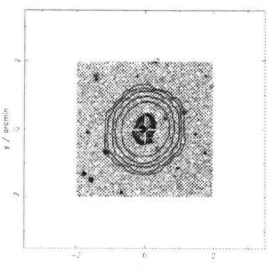

12 54 11.678 +27 37 32.70
3C 277.3

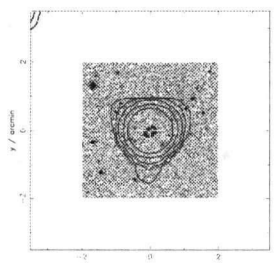

13 05 36.051 +08 55 15.90
4C 09.45

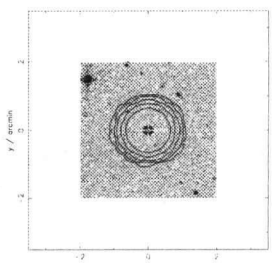

13 13 37.870 +54 58 23.89
TXS 1311+552

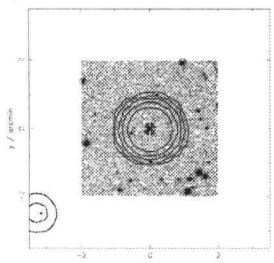

13 19 38.734 -00 49 39.98
PKS 1317-00

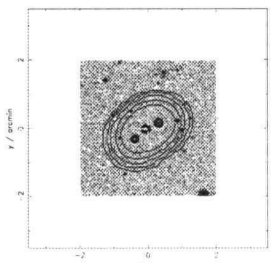

13 23 2.331 +29 41 34.00
FIRST J132302.6+294133

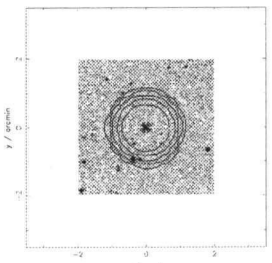

13 31 8.285 +30 30 32.95
3C 286

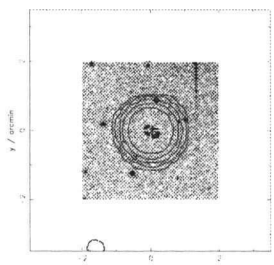

13 20 21.450 +17 43 12.40
4C 17.56

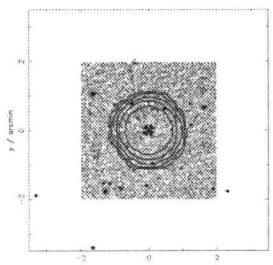

13 26 16.513 +31 54 9.52
4C 32.44

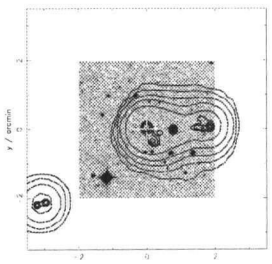

13 32 56.368 +02 00 46.50
3C 287.1

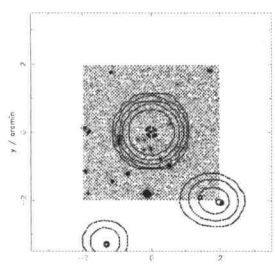

13 21 18.803 +11 06 48.79
PKS 1318+11

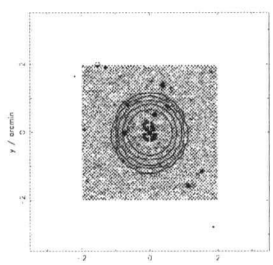

13 27 31.709 +31 51 27.30
4C 32.44B

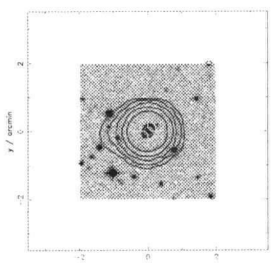

13 38 8.071 -06 27 11.20
QSO J1338-0627

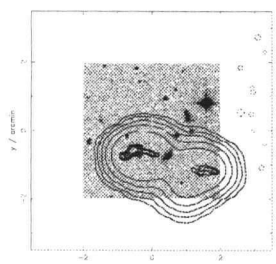

13 21 20.300 +42 36 0.00
3C 285

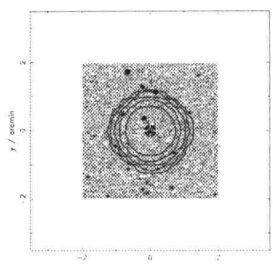

13 30 37.694 +25 09 10.87
3C 287

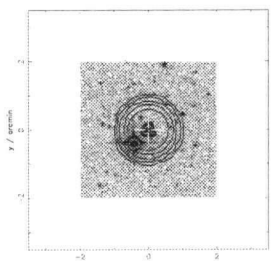

13 38 49.670 +38 51 11.10
3C 288

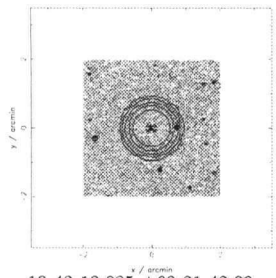

13 42 13.085 +60 21 42.39
3C 288.1

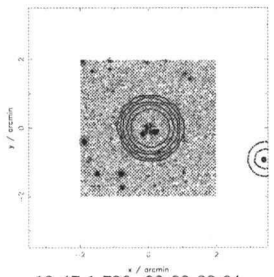

13 47 1.736 -08 03 23.64
PKS 1344-07

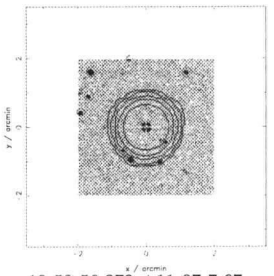

13 52 56.370 +11 07 7.67
PKS 1350+113

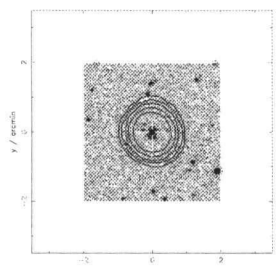

13 42 43.570 +05 04 31.50
4C 05.57

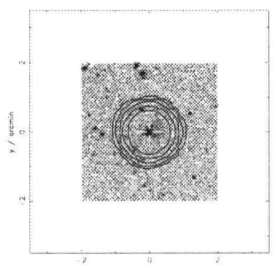

13 47 33.377 +12 17 24.09
PKS 1345+12

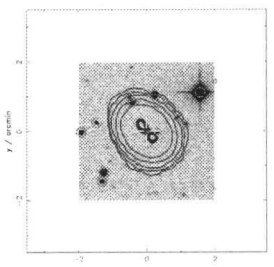

13 57 1.510 +01 04 39.70
4C 01.39

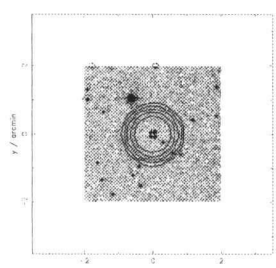

13 44 23.749 +14 09 15.30
4C 14.49

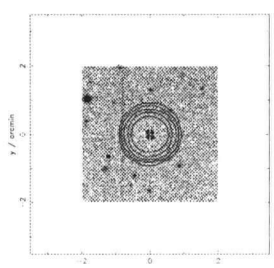

13 49 38.963 +21 07 28.89
3C 291

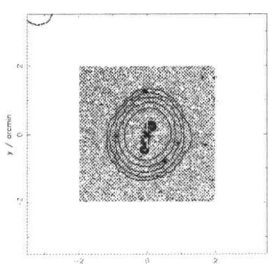

13 57 4.437 +19 19 7.23
PKS 1354+19

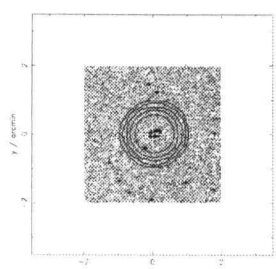

13 45 26.699 +49 46 31.39
3C 289

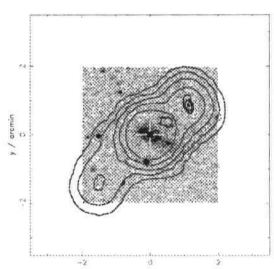

13 52 17.842 +31 26 46.48
3C 293

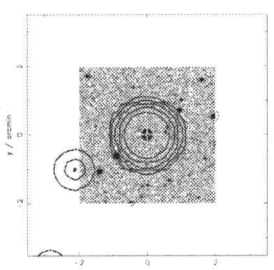

13 57 53.716 +00 46 33.46
PKS 1355+01

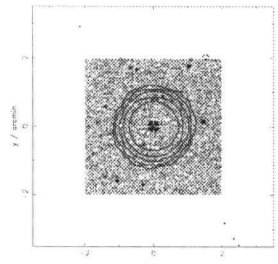

14 00 28.694 +62 10 38.41
4C 62.22

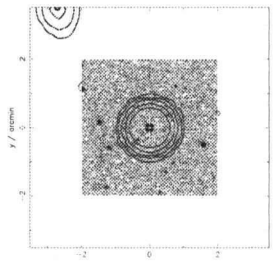

14 16 4.202 +34 44 36.60
S4 1413+34

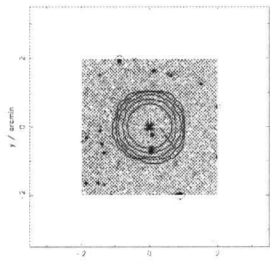

14 19 8.200 +06 28 34.74
3C 298

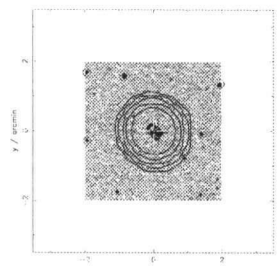

14 06 44.101 +34 11 26.20
3C 294

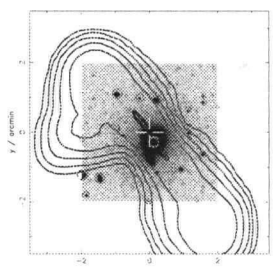

14 16 53.499 +10 48 40.20
NGC 5532

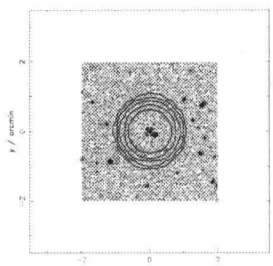

14 21 5.829 +41 44 49.98
3C 299

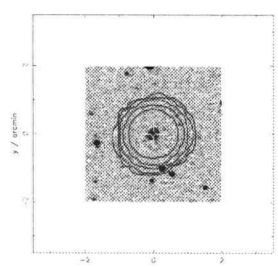

14 11 20.592 +52 12 9.44
3C 295

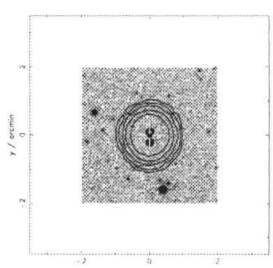

14 17 0.489 +07 10 50.20
4C 07.35

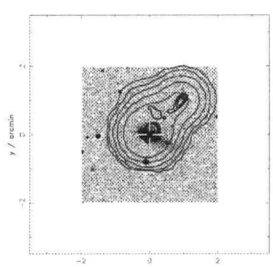

14 23 0.626 +19 35 17.41
3C 300

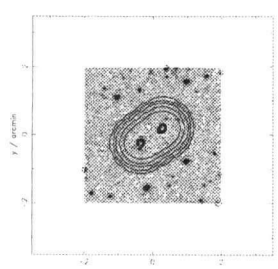

14 13 48.342 -05 59 54.20
4C-05.60

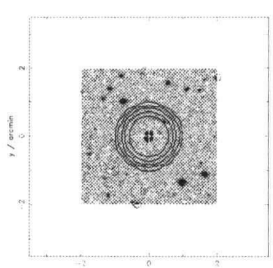

14 17 23.934 -04 00 46.66
3C 297

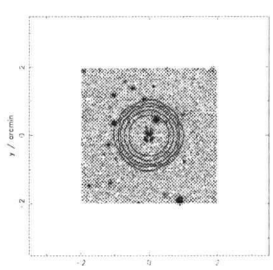

14 24 56.928 +20 00 22.70
7C 1422+2013

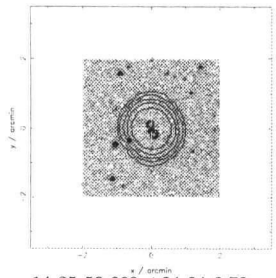

14 25 50.669 +24 04 6.70
4C 24.31

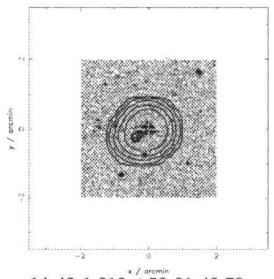

14 43 1.012 +52 01 40.79
3C 303

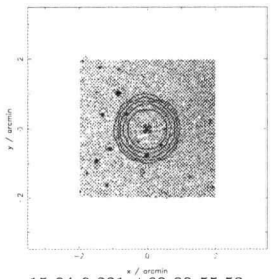

15 04 9.231 +60 00 55.53
3C 311

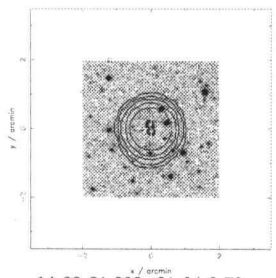

14 28 31.220 -01 24 8.70
3C 300.1

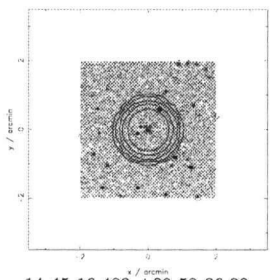

14 45 16.483 +09 58 36.30
PKS 1442+101

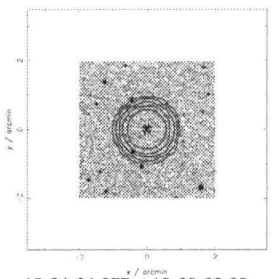

15 04 24.977 +10 29 38.82
PKS 1502+106

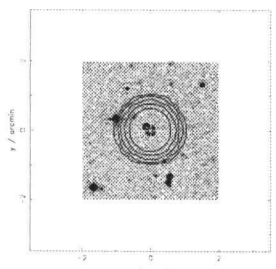

14 36 57.024 +03 24 11.14
PKS 1434+03

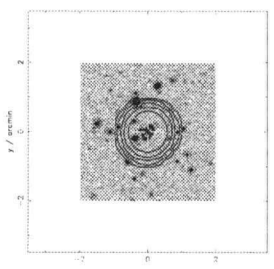

14 48 39.981 +00 18 17.90
4C 00.52

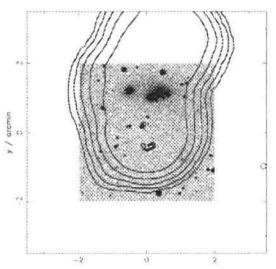

15 04 58.979 +25 59 49.00
3C 310

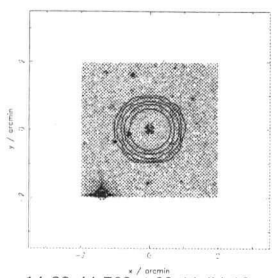

14 38 44.762 +62 11 54.12
QSO B1437+6224

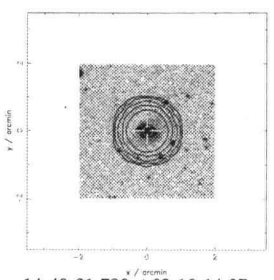

14 49 21.786 +63 16 14.27
3C 305

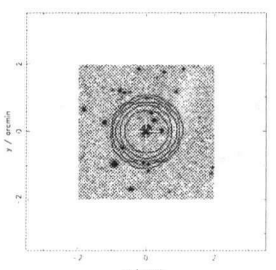

15 10 53.593 -05 43 6.89
PKS 1508-05

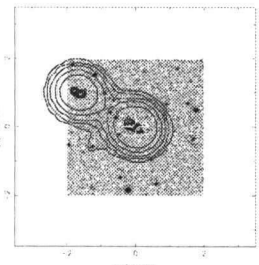

15 10 57.030 +07 51 24.80
3C 313

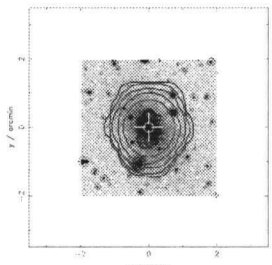

15 16 44.566 +07 01 19.36
3C 317

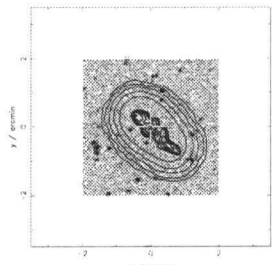

15 24 5.639 +54 28 18.40
3C 319

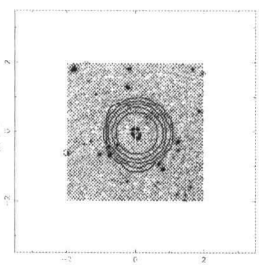

15 12 25.548 +01 21 11.03
4C 01.42

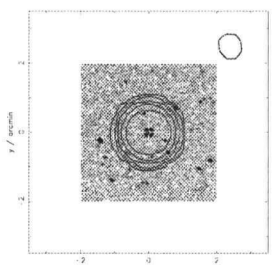

15 16 56.588 +18 30 21.77
3C 316

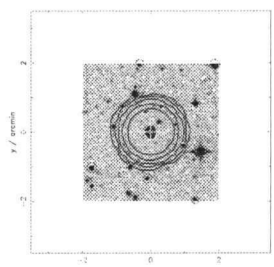

15 25 48.956 +03 08 25.93
4C 03.33

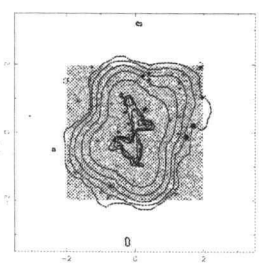

15 13 39.899 +26 07 33.70
3C 315

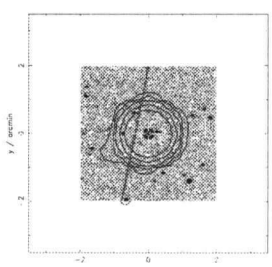

15 20 5.485 +20 16 5.74
3C 318

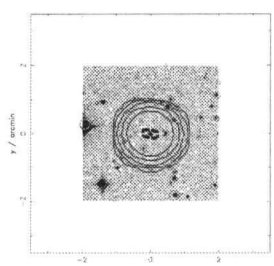

15 31 25.360 +35 33 40.60
3CR 320

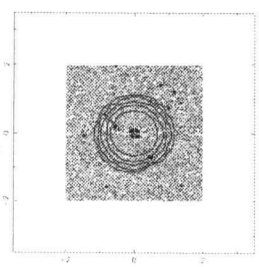

15 13 40.180 +23 38 35.34
PKS 1511+23

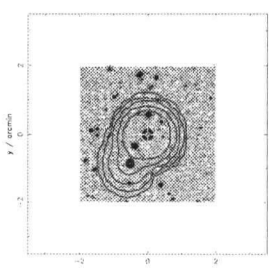

15 21 14.415 +04 30 21.69
PKS 1518+047

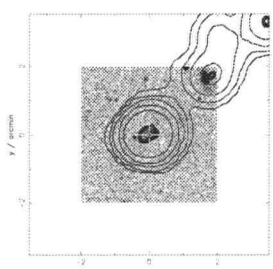

15 31 50.622 +24 02 42.33
3C 321

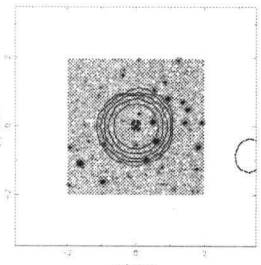

15 34 52.449 +01 31 3.30
QSO B1532+016

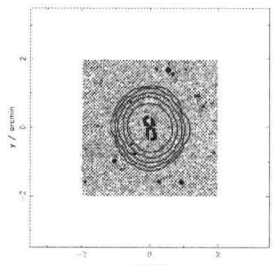

15 41 45.642 +60 15 36.20
3C 323

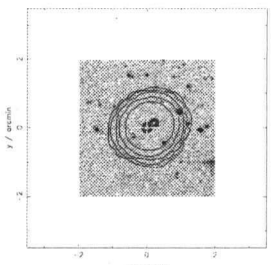

15 49 59.206 +62 41 18.31
3C 325

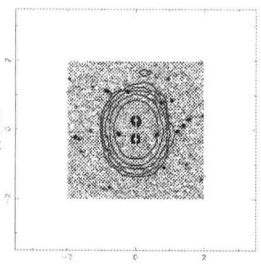

15 35 1.269 +55 36 49.80
3C 322

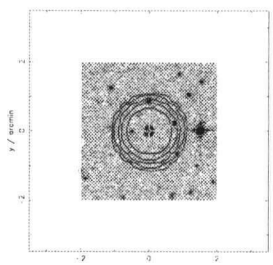

15 46 9.531 +00 26 24.72
PKS 1543+005

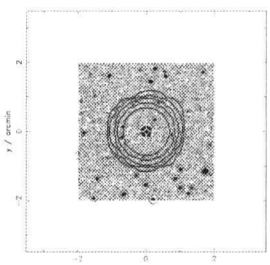

15 50 35.266 +05 27 10.42
PKS 1548+056

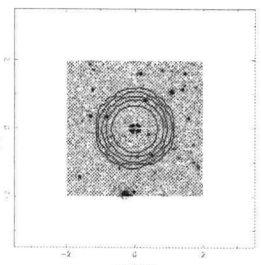

15 37 32.369 +13 44 48.47
4C 13.56

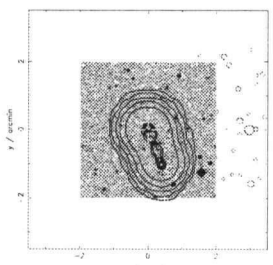

15 47 44.228 +20 52 41.00
3C 323.1

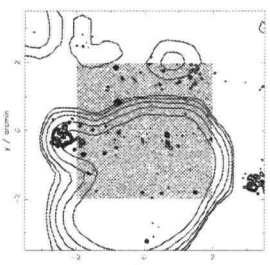

15 52 26.800 +20 07 24.00
3C 326

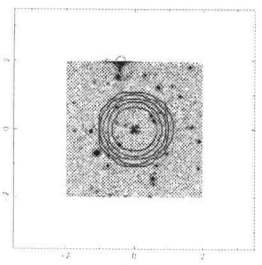

15 40 49.492 +14 47 46.09
PKS 1538+149

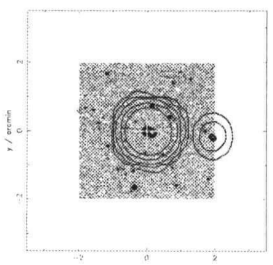

15 49 49.170 +21 25 39.50
3C 324

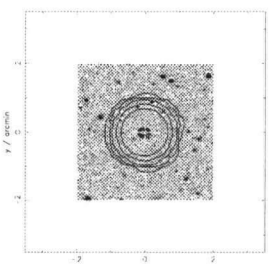

15 56 9.984 +20 04 20.81
3C 326.1

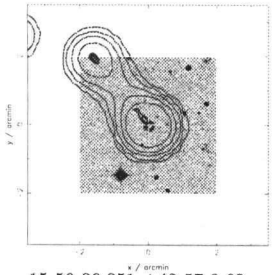

15 56 36.351 +42 57 9.60
5C 13.42

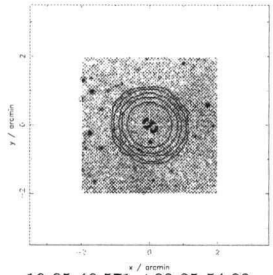

16 05 46.571 +00 25 54.30
PKS J1605+0025

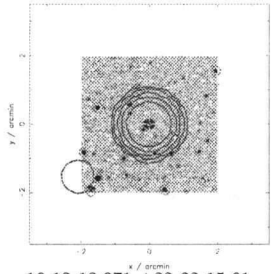

16 12 18.971 +22 22 15.61
3C 331

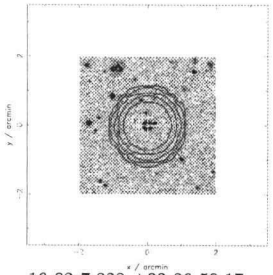

16 02 7.228 +33 26 53.17
4C 33.38

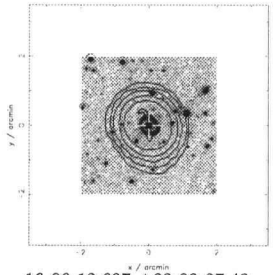

16 06 12.697 +00 00 27.40
4C 00.58

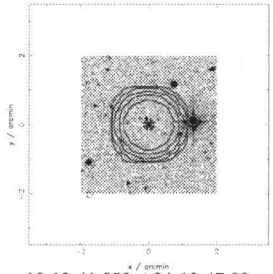

16 13 41.058 +34 12 47.83
QSO B1611+3420

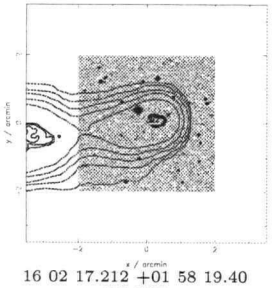

16 02 17.212 +01 58 19.40
3C 327

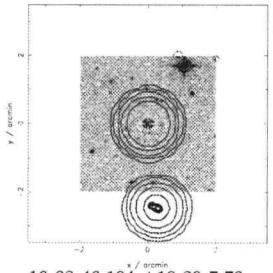

16 08 46.194 +10 29 7.70
PKS 1606+10

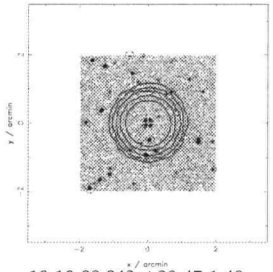

16 16 38.342 +26 47 1.40
PKS 1614+26

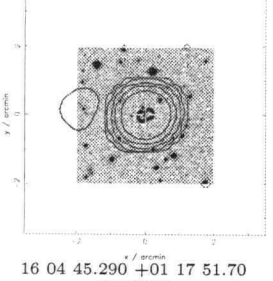

16 04 45.290 +01 17 51.70
3C 327.1

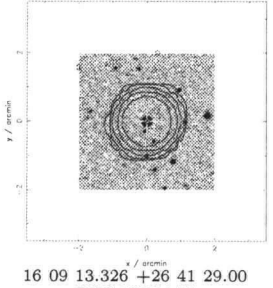

16 09 13.326 +26 41 29.00
PKS 1607+26

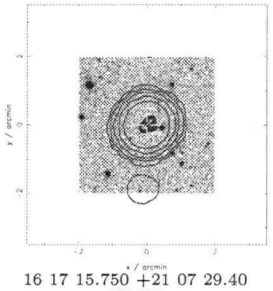

16 17 15.750 +21 07 29.40
3C 333

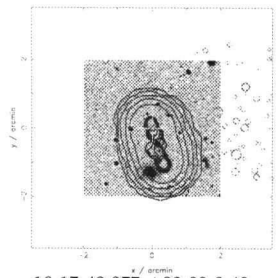

16 17 43.277 +32 23 2.40
3C 332

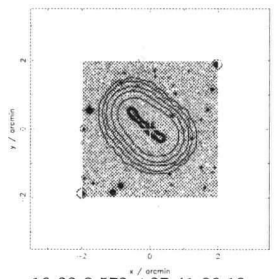

16 28 3.572 +27 41 36.10
3C 341

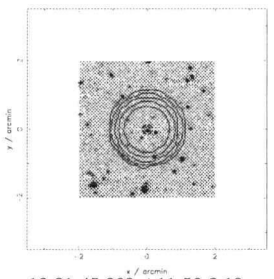

16 31 45.260 +11 56 3.19
PKS 1629+120

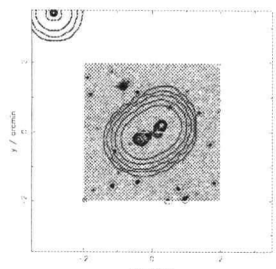

16 20 21.398 +17 36 29.30
3C 334

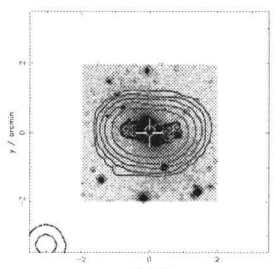

16 28 38.337 +39 33 0.00
3C 338

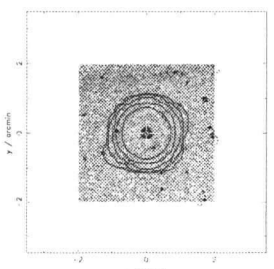

16 34 33.772 +62 45 35.36
3C 343

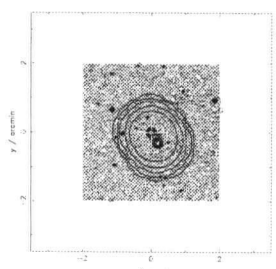

16 24 39.695 +23 45 24.17
3C 336

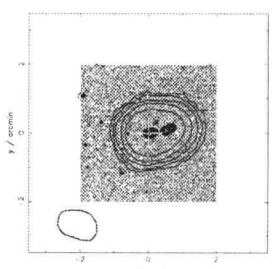

16 28 53.870 +44 19 3.52
3C 337

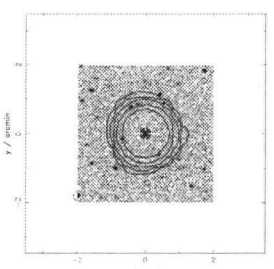

16 35 15.483 +38 08 4.56
4C 38.41

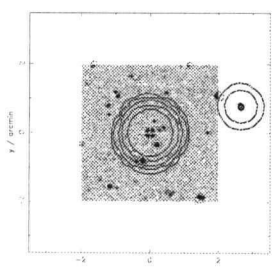

16 25 57.672 +41 34 40.60
4C 41.32

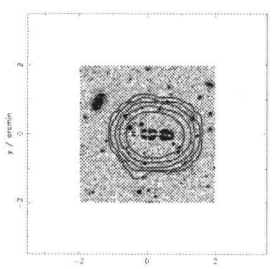

16 29 37.862 +23 20 14.41
3C 340

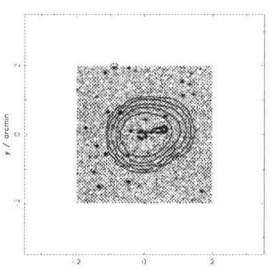

16 36 37.382 +26 48 6.60
3C 342

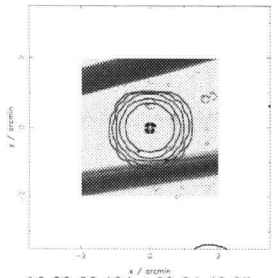

16 38 28.194 +62 34 43.95
3C 343.1

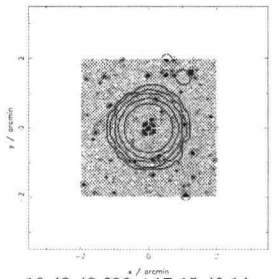

16 43 48.696 +17 15 49.14
3C 346

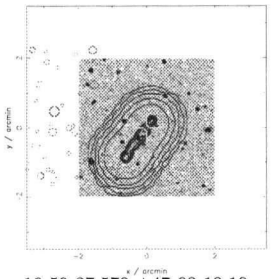

16 59 27.570 +47 03 13.10
3C 349

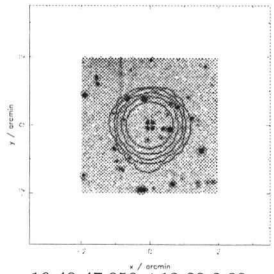

16 40 47.956 +12 20 2.08
4C 12.60

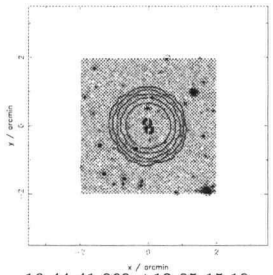

16 44 41.069 +13 05 15.10
4C 13.62

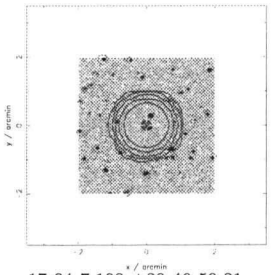

17 04 7.198 +29 46 59.31
4C 29.50

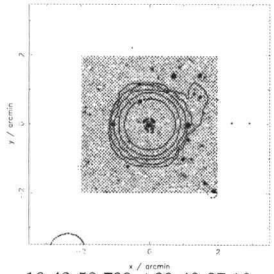

16 42 58.799 +39 48 37.16
3C 345

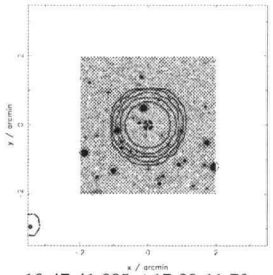

16 47 41.835 +17 20 11.76
PKS 1645+17

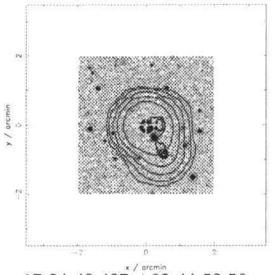

17 04 43.427 +60 44 52.56
3C 351

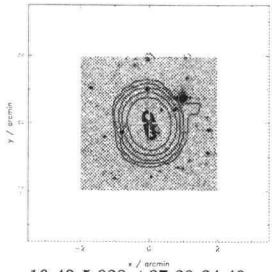

16 43 5.928 +37 29 34.40
3C 344

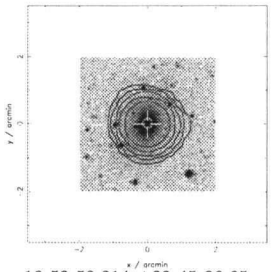

16 53 52.214 +39 45 36.65
4C 39.49

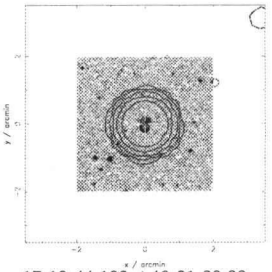

17 10 44.108 +46 01 30.30
3C 352

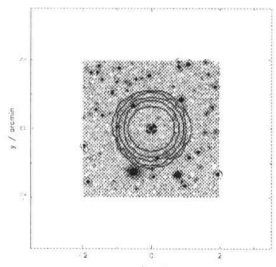

17 19 8.937 +22 45 6.08
PKS 1717+22

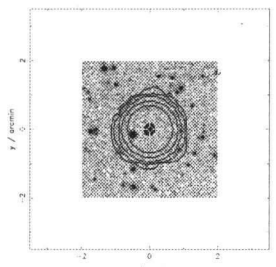

21 34 10.335 -01 53 17.39
PKS 2131-021

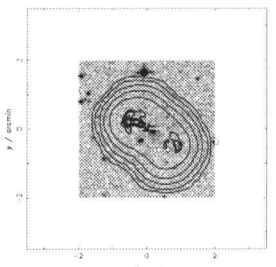

23 26 54.468 -02 02 10.30
PKS 2324-02

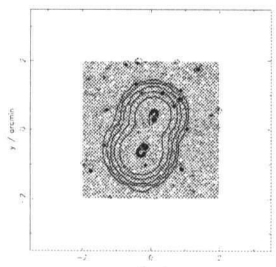

17 24 18.400 +50 57 54.00
3C 356

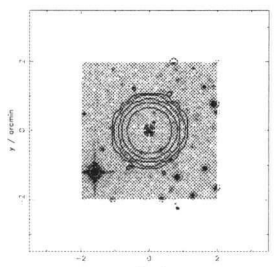

21 36 38.600 +00 41 54.47
PKS 2134+004

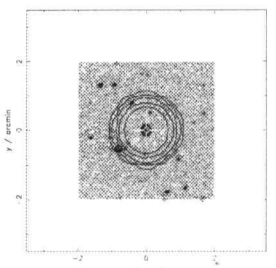

23 32 25.585 -09 57 56.42
PKS 2329-10

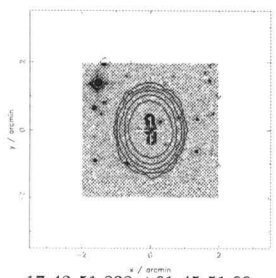

17 42 51.838 +61 45 51.00
4C 61.34

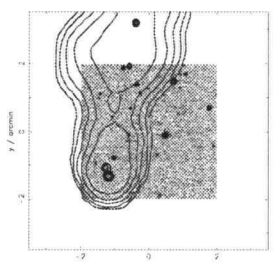

22 23 48.000 -02 09 24.00
3C 445

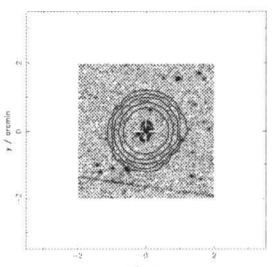

23 51 56.210 -01 09 16.30
QSO B2349-0125

Appendix D

Comments on particular sources

00 57 34.150 -01 22 58.40 Coordinates are not centered on the optical identification.

01 26 4.670 -01 24 1.90 NGC 547, also known as 3C 040. Coordinates are not centered on the optical identification.

07 58 28.601 +37 47 13.80 This source shows no NVSS contours on the plot.

08 05 31.310 +24 10 21.30 Coordinates are not centered on the optical identification.

08 22 31.400 +05 57 24.00 Coordinates are not centered on the optical identification. This is a large FRI source with only few FIRST detections.

08 30 4.120 +07 45 45.00 This source actually consists in 2 separate sources, both with $S < 1.3Jy$ .It was taken out of the primary sample.

09 21 8.650 +45 38 57.40 This source is probably a FRII that has slightly rotated.

09 39 50.199 +35 55 53.10 Coordinates are not centered on the optical identification.

09 41 25.700 +39 42 18.00 Coordinates are not centered on the optical identification.

09 47 47.270 +07 25 13.81 Coordinates are not centered on the optical identification.

10 01 46.200 +28 46 54.69 Coordinates are not centered on the optical identification.

11 23 9.062 +05 30 20.58 This source actually consists in 2 separate sources, one of them with $S \geq 1.3Jy$.

11 45 5.229 +19 36 37.80 3C 264, also known as NGC 3862.

11 45 31.181 +31 33 35.82 Coordinates are not centered on the optical identification.

12 00 59.000 +31 31 12.00 Coordinates are not centered on the optical identification.

12 19 15.329 +05 49 40.40 Coordinates are not centered on the optical identification.

12 24 30.200 +42 06 24.00 Coordinates are not centered on the optical identification.

12 29 6.410 +02 03 5.10 Probable QSO with visible jets.

12 35 22.971 +21 20 18.30 Coordinates are not centered on the optical identification.

12 53 3.549 +02 38 22.30 Coordinates are not centered on the optical identification.

13 11 6.600 +27 26 6.00 Coordinates are not centered on the optical identification.

13 21 20.300 +42 36 0.00 Coordinates are not centered on the optical identification.

13 23 2.331 +29 41 34.00 This source actually consists in 3 separate sources, all with $S < 1.3Jy$ .It was taken out of the primary sample.

13 32 56.368 +02 00 46.50 Coordinates are not centered on the optical identification.

13 52 17.842 +31 26 46.48 The jets being seen only on one side in the FIRST contours, the source was classified as FRI.

14 17 0.489 +07 10 50.20 This source actually consists in 2 separate sources, both with $S < 1.3Jy$ .It was taken out of the primary sample.

15 04 58.979 +25 59 49.00 Coordinates are not centered on the optical identification.

15 10 57.030 +07 51 24.80 Coordinates are not centered on the optical identification.

15 31 50.622 +24 02 42.33 Coordinates are not centered on the optical identification.

15 52 26.800 +20 07 24.00 Coordinates are not centered on the optical identification.

15 56 36.351 +42 57 9.60 This is a known radio source, but no optical identification shows on the contour plot.

16 02 17.212 +01 58 19.40 Coordinates are not centered on the optical identification.

22 23 48.000 -02 09 24.00 Coordinates are not centered on the optical identification.

Sources from the 3CRR sample The following sources can be found in Laing, Riley & Longair (1983):

06 55 14.780 +54 09 00.00	3C 171	12 54 11.678 +27 37 32.70	3C 277.3
08 01 33.507 +14 14 42.66	3C 190	12 56 57.380 +47 20 19.80	3C 280
08 04 47.970 +10 15 22.91	3C 191	13 00 32.870 +40 09 9.20	3C 280.1
08 05 31.310 +24 10 21.30	3C 192	13 11 6.600 +27 26 6.00	3C 284
08 13 36.037 +48 13 1.77	3C 196	13 21 20.300 +42 36 0.00	3C 285
08 27 25.398 +29 18 44.80	3C 200	13 30 37.694 +25 09 10.87	3C 287
08 39 6.500 +57 54 13.40	3C 205	13 31 8.285 +30 30 32.95	3C 286
08 40 47.712 +13 12 23.64	3C 207	13 38 49.670 +38 51 11.10	3C 288
08 53 9.008 +13 52 55.83	3C 208	13 45 26.699 +49 46 31.39	3C 289
08 58 41.539 +14 09 43.24	3C 212	13 52 17.842 +31 26 46.48	3C 293
09 06 31.879 +16 46 13.00	3C 215	14 06 44.101 +34 11 26.20	3C 294

09 08 50.561 +37 48 20.20	3C 217	14 11 20.592 +52 12 9.44	3C 295
09 09 33.497 +42 53 46.54	3C 216	14 21 5.829 +41 44 49.98	3C 299
09 21 8.650 +45 38 57.40	3C 219	14 23 0.626 +19 35 17.41	3C 300
09 39 50.199 +35 55 53.10	3C 223	14 43 1.012 +52 01 40.79	3C 303
09 44 16.401 +09 46 19.20	3C 226	14 49 21.786 +63 16 14.27	3C 305
09 50 10.566 +14 19 40.30	3C 228	15 04 58.979 +25 59 49.00	3C 310
10 01 46.200 +28 46 54.69	3C 234	15 13 39.899 +26 07 33.70	3C 315
10 06 1.738 +34 54 10.43	3C 236	15 20 5.485 +20 16 5.74	3C 318
10 11 45.460 +46 28 20.10	3C 239	15 24 5.639 +54 28 18.40	3C 319
10 21 54.533 +21 59 30.50	3C 241	15 31 50.622 +24 02 42.33	3C 321
10 33 33.870 +58 14 37.90	3C 244.1	15 35 1.269 +55 36 49.80	3C 322
10 42 44.586 +12 03 31.32	3C 245	15 49 49.170 +21 25 39.50	3C 324
10 58 58.360 +43 01 21.66	3C 247	15 49 59.206 +62 41 18.31	3C 325
11 11 31.558 +35 40 45.50	3C 252	15 52 26.800 +20 07 24.00	3C 326
11 14 38.814 +40 37 19.13	3C 254	16 20 21.398 +17 36 29.30	3C 334
11 43 25.040 +22 06 56.00	3C 263.1	16 24 39.695 +23 45 24.17	3C 336
11 45 5.229 +19 36 37.80	3C 264	16 28 3.572 +27 41 36.10	3C 341
11 45 31.181 +31 33 35.82	3C 265	16 28 38.337 +39 33 0.00	3C 338
11 45 43.384 +49 46 7.90	3C 266	16 28 53.870 +44 19 3.52	3C 337
11 49 55.540 +12 47 15.90	3C 267	16 29 37.862 +23 20 14.41	3C 340
12 09 13.401 +43 39 16.89	3C 268.4	16 34 33.772 +62 45 35.36	3C 343
12 20 33.888 +33 43 7.97	3C 270.1	16 38 28.194 +62 34 43.95	3C 343.1
12 24 30.200 +42 06 24.00	3C 272	16 42 58.799 +39 48 37.16	3C 345
12 25 3.781 +12 52 35.20	3C 272.1	16 43 48.696 +17 15 49.14	3C 346
12 30 49.460 +12 23 21.60	3C 274	16 59 27.570 +47 03 13.10	3C 349
12 35 22.971 +21 20 18.30	3C 274.1	17 04 43.427 +60 44 52.56	3C 351
12 43 57.650 +16 22 48.13	3C 275.1	17 10 44.108 +46 01 30.30	3C 352
12 53 32.425 +15 42 25.29	3C 277.2	17 24 18.400 +50 57 54.00	3C 356